Monolithic Electronic-Photonic Systems for Massive-MIMO Millimeter-Wave Applications

Ruocheng Wang

Electrical Engineering and Computer Sciences
University of California, Berkeley

Technical Report No. UCB/EECS-2024-201
http://www2.eecs.berkeley.edu/Pubs/TechRpts/2024/EECS-2024-201.html

December 1, 2024

Monolithic Electronic-Photonic Systems for Massive-MIMO Millimeter-Wave Applications

by

Ruocheng Wang

A dissertation submitted in partial satisfaction of the

requirements for the degree of

Doctor of Philosophy

in

Engineering - Electrical Engineering and Computer Sciences

in the

Graduate Division

of the

University of California, Berkeley

Committee in charge:

Professor Vladimir Stojanović, Chair
Professor Ming-Chiang Wu
Professor Martin White

Fall 2023

The dissertation of Ruocheng Wang, titled Monolithic Electronic-Photonic Systems for Massive-MIMO Millimeter-Wave Applications, is approved:

Chair _____ Date _____

_____ Date _____

_____ Date _____

University of California, Berkeley

Monolithic Electronic-Photonic Systems for Massive-MIMO Millimeter-Wave Applications

Abstract

Monolithic Electronic-Photonic Systems for Massive-MIMO Millimeter-Wave Applications

by

Ruocheng Wang

Doctor of Philosophy in Engineering - Electrical Engineering and Computer Sciences

University of California, Berkeley

Professor Vladimir Stojanović, Chair

Modern wireless communication systems at millimeter-wave frequency band embrace the scalable massive-MIMO architecture to address the increasing demand for data capacity, while the design challenge in terms of size, weight, power and cost still remain in the pure electrical millimeter-wave systems. Leveraging miniaturized modulators with high bandwidth capacity, silicon photonic links provides potential solutions for large scale data communication within such systems. This work proposes a disaggregated architecture based on silicon photonic link and presents several essential design considerations. For the silicon photonic modulation, the conventional microring modulator is analyzed and proven to have fundamental operating frequency limitation due to its intrinsic characteristic, and so the advanced modulators are presented as the alternative solution with their individual performance metrics analyzed. In addition, the end-to-end performance of the proposed link architecture is modeled providing guidance for both the design optimization of the advanced modulators and the electrical circuits as a part of the complete monolithic electronic-photonic system. Two of the core array elements on the photonic transmitter side and receiver side for the proposed architecture are designed in the monolithic integration process platforms, with their design procedure introduced, and the measurement results of the transmitter array element demonstrate a promising performance metric for the realistic system.

To my mother.

——祝愿人们幸福。

Contents

List of Figures

List of Tables

Acknowledgments

In late January 2017, people around me were celebrating the Spring Festival. I wasn't enjoying it - as I couldn't stop thinking of my Ph.D. applications - until February 3rd when I received the admission email. I can't clearly remember how I exactly felt at that time, but I did feel that there were gears starting to turn. It has been turning for six year from then, and as a new destination is appearing, I would like to thank all the people who helped me along the journey that is going to complete soon.

I would like to begin by thanking my advisor, Professor Vladimir Stojanović, not only for his inspirations during the research, but also for his endless passion and dedicated efforts to managing the projects, to building up the excellent research environment, and to providing practical advice both inside and outside the research field. I am sincerely grateful that I can be advised by him.

I would next like to thank Professor Ali Niknejad, Professor Ming Wu and Professor Martin White for being in my qualification exam or thesis committees and for offering valuable feedback. I would like to again thank Professor Ali Niknejad for the courses of communication ICs and Professor Ming Wu for the course of lightwave device. Both courses offer valuable guidance during my research.

Research often means collaboration, and I would like to thank people who I have collaborated with. Within the Integrated Systems Group (ISG), I would like to thank Sidney Buchbinder in particular, as we have worked on many projects together, from infrastructure development to link modeling and implementation, and as I have learned a lot from him. I would also thank Professor Miloš Popović for leading his photonics team at Boston University, and thank the students in his team, particularly Manuj Singh, Deniz Onural, Dorde Gluhovic and Xinchang Zhang, for their knowledge of the photonic device. Among them, I would like to give the special thank to Manuj Singh, for all the discussions with him that helped me understand the device better, for his iterative work to clean up our design during the tapeouts, and for the measurement work he made.

I would like to thank all the other students of the Integrated Systems Group for their help. Thank you to Bozhi Yin and Daniel Kramnik for answering the packaging related questions, and for sharing the useful building blocks. Thank you to Sarika Madhvapathy and Hyeong-Seok Oh for helping with the substrate release process. The days that the tapeout deadline approaches can be stressful, and I would like to thank Sunjin Choi and Wahid Rahman for managing the tapeout repository and the top level assembly.

I have also achieved a lot from the students in Berkeley Wireless Research Center (BWRC) outside ISG. I would like to thank Luya Zhang, Zhongkai Wang and Benyuanyi Liu, as they are the senior students who can share their valuable experience. Thank you to Zhaokai Liu for the information of packaging and evaluation board design. Thank you to Meng Wei, Yikuan Chen for answering the RF related questions. Keeping health both physically and emotionally is also an important part of the Ph.D. study, so in addition I would like to thank Yue Dai for chatting about a wide range of interesting topics, and thank Rebekah Zhao, Yi-Hsuan Shih and Liz Murray for the weekend badminton sessions.

I am also grateful for all the members and staffs in BWRC for maintaining a collaborative environment. Special thanks to Candy Corpus-Steudeman and Mikaela Cavizo-Briggs for organizing the wonderful events and for coordinating with the purchase orders.

I am also going to thank my friends who share the interesting stories in our daily life with each other. Thank you to Canxun Zhang for being my roommate for 5 years and sharing your impressive knowledge database. Thank you to Junjie Hu and Xiao Lyu, two of my undergrad roommates, for keeping the frequency online chat even though we are not in the same city. Witnessting the happiness is always pleasant, so I would like to thank Wenlong Mou and Rui Zhang for inviting me to their wedding; in addition, thank you to Ziyu Ma for inviting me to your wedding in New York and thank you to Bowen Yao for inviting me to your wedding in Philadelphia, so I could get chance to plan these exciting long-distance travels. Additionally, thank you to Chenhao Bao, for sharing thoughts on a wide range of topics, including news, animations and so on.

Finally, I would like to give my special thanks to my mother, for raising me up, for creating the best education environment that she could, for respecting the decisions I made, for the emotional support of all time, and for the endless love.

Support: This material is based upon work supported by the National Science Foundation under grant No. 2328945 and is supported in part by funds from federal agency and industry partners as specified in the Future of Semiconductors (FuSe) program. This work has also been supported in part by JUMP ComSenter, DII and BWRC member companies.

Chapter 1

Introduction

1.1 Motivation

The increasing demand for data capacity in modern wireless communication motivates the exploration of advanced system architectures. One of the trends is to utilize the massive-MIMO technique that replaces a single antenna with a large scale antenna array. With the feature of beamforming, the massive-MIMO technique benefits from the feature of spatial multiplexing and higher directivity. Utilizing higher frequency bands (50 - 100 GHz and beyond) further enables thousands of antenna elements per array panel for future communication and sensing systems.

There are various massive-MIMO architectures for aggregating and processing the RF

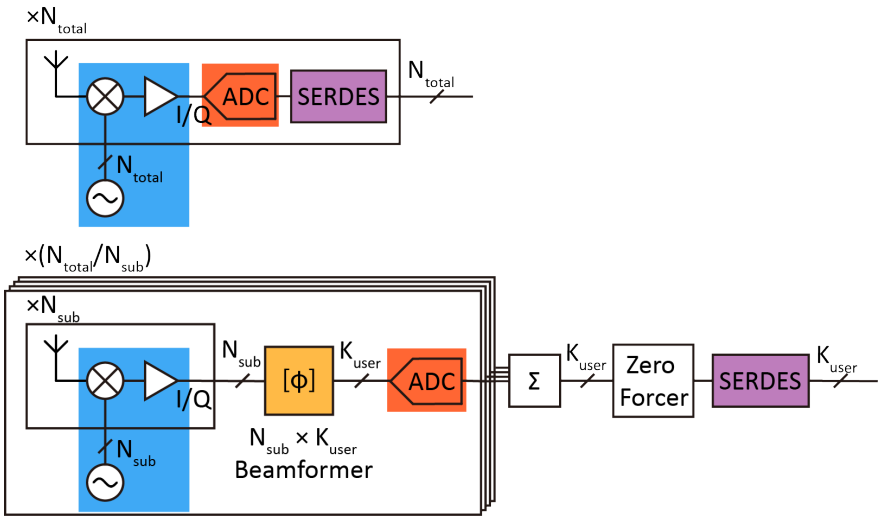

Figure 1.1: Diagram of present massive-MIMO architectures. Top: impractical fully centralized array; bottom: two-stage fully connected array

signals. A fully centralized array shown at the top of Fig. 1.1, where the baseband data from an antenna array with a size of N_{total} is not processed before transmitted out of the array. Due to the large capacity and the number of physical channels required for the high-speed serial links, this architecture is by no means practical if they are realized with electrical components. One architecture of a two-stage fully-connected array was therefore proposed [1], shown at the bottom of Fig. 1.1. This architecture utilizes a $N_{total} \times K_{user}$ beamformer to convert the data from antenna dimensions to user dimensions. Given the fact that the array size is much larger than the user size: $N_{total} \gg K_{user}$, there is significantly less design constraint for the serial link with the bottom architecture. However, design challenges still exist for this architecture in size, weight, power and cost (SWAP-C), especially if we scale up the carrier frequency and the size of the massive-MIMO array: A higher carrier frequency caused higher channel bandwidth that lead to the increasing number of baseband samples and beamforming compute throughput, and it also brings stricter area constraint as the antenna array co-packaged with the circuit follows the half-wavelength pitch. The co-scaling of antenna array size and the number of users results in baseband processing blocks with higher design cost, especially the beamformer with quadratically increasing power and area. In summary, the scaling causes both the beamforming processors and the links from ADCs / DACs to processors to begin dominating the SWAP-C of the array panel.

A critical reason for these design challenges is that the baseband processing is required close to the antenna array, given the fact that the SERDES link in the fully centralized architecture sacrifices energy efficiency due to limited physical channels that can be implemented. Emerging high-density, low-power silicon-photonic optical links however, address this design constraint. Such links take advantage of lower crosstalk and loss along the link channel, and feature wavelength division multiplexing (WDM) which reduces the number of physical fiber channels. The proposed silicon-photonic links directly from mm-wave frontends to the processing chips would enable radio unit (RU) disaggregation into a low SWAP-C sensor panel and remote processor. This further enables new multi-static sensing and cell-free communication architectures where many low SWAP-C panels per central processing site can be organized to optimize the sensing and communication capacity.

Therefore, we proposed a silicon-photonic based architecture that is built with the antenna array and the processing hub, which is shown in Fig. 1.2. The compact, low-power mm-wave sensing element, consisting of a Low Noise Amplifier (LNA) driver monolithically integrated with a silicon-photonic microring modulator (MRM), is implemented as an array across the antenna site. The sensing element design is a critical building block that enables the low SWAP-C mm-wave sensing arrays with thousands of them. The sensing array site communicates with the processing hub via photonic links featuring wavelength division multiplexing (WDM), which reduces the number of physical channels (optical fibers), and takes advantage of lower crosstalk and loss. The MRM is approximately 10 μm in diameter and 10 fF in capacitance, typically 100 times smaller area and power footprint than the Mach-Zehnder Modulator (MZM). While providing the high-bandwidth connectivity to the remote processing hub, the design leverages tiny MRM footprint, monolithic integration with LNA driver, and wavelength-multiplexing capability to realize energy-efficient, high-bandwidth

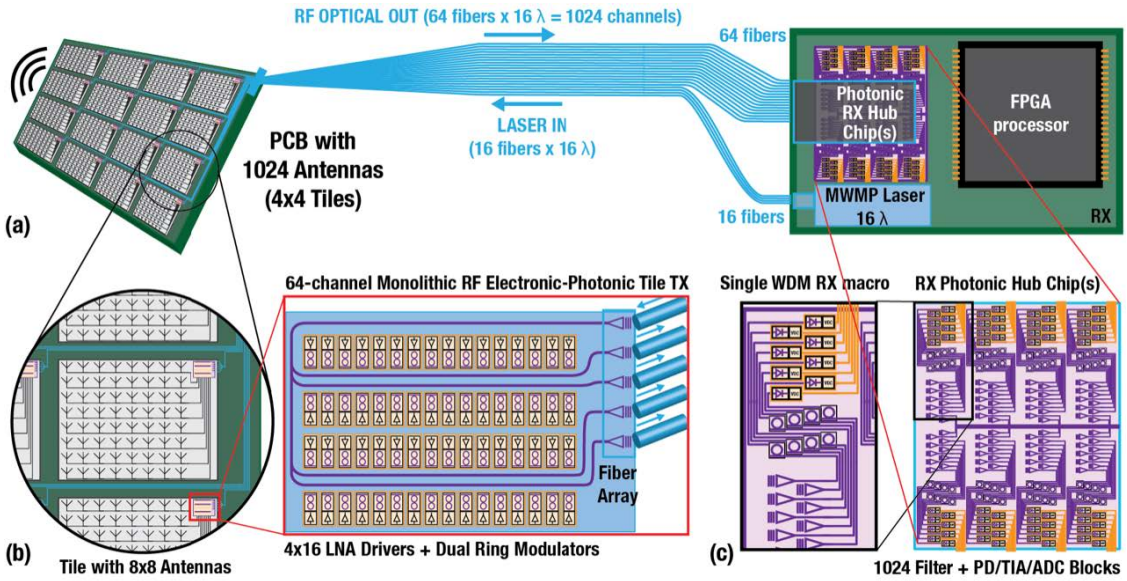

Figure 1.2: Diagram of the proposed system architecture

density transmission. The processing site contains the laser source, the photonic receiver (RX) hub as the frontend, plus the backend processing. This processing site handles all the data conversion, beamforming and other additional post processing that is power consuming.

With the proposed architecture, the entire system is split into two subsystems that can be implemented in different location with a medium- to long-reach distance. The compact and low power antenna array site is implemented wherever the mm-wave signals are accessible, and the more power-hungry processing site can be close to the back haul where the power delivery is no longer a challenge. A promising evaluation and demonstration of such electronic-photonic massive-MIMO architecture would explore a new path for the future of large-capacity communication system.

1.2 Thesis Organization

The goal of this thesis is to illustrate the design of the silicon photonic transceiver array element for the wireless receiver in a massive-MIMO mm-wave system. Chapter 2 begins with the fundamentals and performance limitation of the basic electro-optical (EO) modulator and then introduces the advanced modulators for high-frequency EO conversion. Chapter 3 analyzes the system level performance metrics of the silicon photonic system. Chapter 4 illustrates the design of a silicon-photonic mm-wave frontend as the element of the sensing array with a commercial RFSOI process, parts of this work appear in

- [2] Ruocheng Wang et al. “A Monolithically Integrated Electronic-Photonic Front-end Utilizing Micro-ring Modulators for Large-Scale mm-wave Sensing”. In: *ESSCIRC*

2023- IEEE 49th European Solid State Circuits Conference (ESSCIRC). 2023, pp. 489–492

- [3] Manuj Singh et al. "Electronic-Photonic Millimeter-Wave Sensing Element Based on Monolithically Integrated LNA and Triple Cavity Ring Modulator". In: *2023 European Conference on Optical Communication (ECOC)*. 2023

Next design is developed in an advanced electronic-photonic process in Chapter 5. Chapter 6 presents the design of the receiver element. Chapter 7 concludes the entire thesis.

Chapter 2

Millimeter-Wave Electro-Optical Conversion

In this section we start with the concept of microring modulators (MRM) by describing how electrical signals get modulated to the optical band and characterizing the critical design parameters that influence the electro-optical (EO) modulation efficiency. Then we present the reason why single-MRM is fundamentally inefficient in handling mm-wave EO modulation. Finally, we illustrate how dual-MRM and triple-MRM resolve the issue of high-frequency mm-wave EO conversion.

2.1 Fundamentals of Microring Modulator

A typical single-MRM shown in Fig. 2.1 consists of a resonance cavity and one or more coupling waveguides. The incident lightwave travels along the waveguides. The resonance cavity makes the lightwave circulate and accumulate inside, and the coupling waveguides enable the lightwave propagating into or out of the cavity. Given the assumptions of lossless coupling, the steady-state transmission of the electric field from the input port to the through port can be solved from the two equations [4]:

$$\begin{bmatrix} \tilde{E}_{thru} \\ \tilde{E}_{cav} \end{bmatrix} = \begin{bmatrix} t & \kappa \\ -\kappa^* & t^* \end{bmatrix} \begin{bmatrix} \tilde{E}_{in} \\ \tilde{E}_{cav,rt} \end{bmatrix}, \qquad \tilde{E}_{cav,rt} = a_{rt} e^{j\phi_{rt}} \tilde{E}_{cav} \tag{2.1}$$

$$\Rightarrow t_E \equiv \frac{\tilde{E}_{thru}}{\tilde{E}_{in}} = \frac{t - a_{rt} e^{j\phi_{rt}}}{1 - t^* a_{rt} e^{j\phi_{rt}}} \tag{2.2}$$

In the equations, $\tilde{E}$ represents the steady-state lightwave with time-varying phase, with its magnitude proportional to the E-field strength, and with its square of magnitude equals the lightwave power P; t, κ are the self-coupling and cross-coupling coefficients of the lossless coupling waveguide fulfilling $|t|^2 + |\kappa|^2 = 1$, a_{rt} is the round-trip E-field magnitude transmission, and ϕ_{rt} is the round-trip phase shift. Fig. 2.2 shows an example of the magnitude and

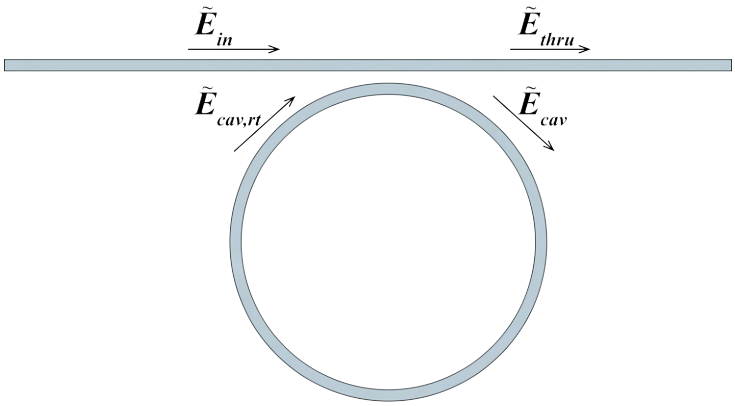

Figure 2.1: Diagram of a basic single microring modulator

phase of the E-field MRM transfer function, t_E, with respect to ϕ_{rt}. Intuitively, when the ring is on resonance, which means that the lightwave frequency equals a specific resonance frequency ω_0 so that ϕ_{rt} equals an integer multiple of 2π, the E-fields at different rounds of trips inside the cavity are accumulated with the same phase, so that the accumulated steady-state cavity E-field is maximized, and $\tilde{E}_{thru}$ is minimized since the $\tilde{E}_{in}$ and $\tilde{E}_{cavity,rt}$ contribute to the through port destructively. If the ring is off resonance, which means ϕ_{rt} is far away from any integer multiple of 2π, the accumulated cavity E-field is minimized, so that $\tilde{E}_{thru}$ is very close to $\tilde{E}_{in}$. The extinction ratio (ER) describing the depth of the Lorentzian shape in Fig. 2.2a depends on the relationship between $1 - a_{rt}^2$ and $|\kappa|^2$, which represent the energy dissipated and coupled into the cavity, respectively. In case these two energy terms are equal, the highest extinction ratio will be obtained which is also known as the critically coupled condition. In case t and a_{rt} are closer to 1, the accumulated $\tilde{E}_{cavity,rt}$ will be more sensitive to ϕ_{rt}, which depends on the refractive index that can be modulated by the voltage applied.

The modulated optical signal can be demodulated by one or more photodetectors (PDs) into the photo current:

$$I_{PD} = \mathcal{R}_{PD}\tilde{E}_{PD}\tilde{E}_{PD}^{*} \tag{2.3}$$

where $\mathcal{R}_{PD}$ is the responsivity of a PD and $\tilde{E}_{PD}$ is the complex optical signal that reaches it. The amplitude modulation and the phase modulation can be demodulated with intensity-modulation direct-detection (IMDD) links [5–8] and coherent links [9–12], respectively. Benefiting from the accumulation of incident lightwave, the response of an MRM is sensitive to the refractive index modulation when it is close to the on-resonance state, while its footprint of around 10 - 20 μm in diameter and 10 - 20 fF in load capacitance are much smaller than the conventional Mach-Zehnder modulator (MZM) with a typical length of at least hundreds of microns and a capacitance over 1 pF [13–15].

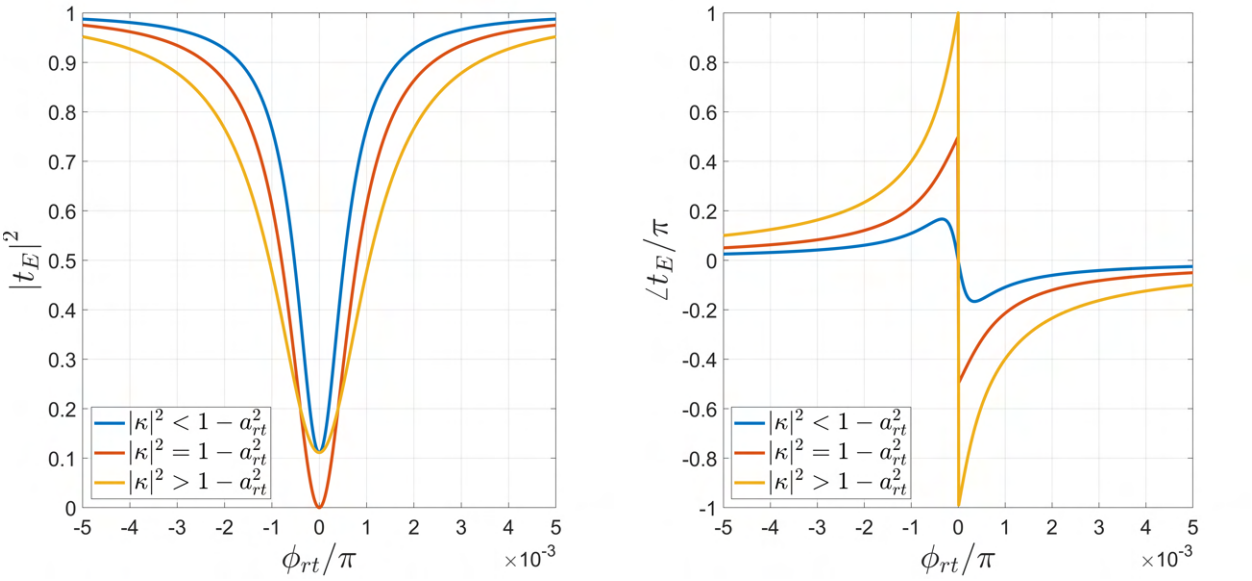

(a) Normalized through port power

(b) Phase

Figure 2.2: E-field transfer function of three single MRM examples

2.2 Gain and Bandwith Limitations of Single MRM

Being derived from the steady-state analysis, Eq. 2.2 only applies to the cases where the modulation voltage is varying slowly, which does not apply to mm-wave EO modulations. To extend the characterization of MRMs into a wider modulation frequency range, time domain analysis is required. The time domain behavior of the incident lightwaves, including a which represents the amplitude of lightwave energy in the ring cavity, and S_{in}, S_{thru} which represent the amplitudes of lightwave power that couples into and out of the cavity, described by [16]:

$$\frac{d}{dt}a = (j\omega - r_o)a - j\sqrt{2r_e}S_{in}, \qquad S_{thru} = S_{in} - j\sqrt{2r_e}a \tag{2.4}$$

, where ω is the angular frequency of the lightwave, r_o is the material-dependant decay rate of the E-field inside the cavity waveguide, and r_e represents the mutual coupling between the resonance cavity and the bus waveguide. Given the group velocity v_g and the ring radius R, these parameters can also derive the values of those in Eq. 2.1:

$$-ln(a_{rt}) = r_o\frac{2\pi R}{v_g}, \qquad \phi_{rt} = \omega\frac{2\pi R}{v_g}, \qquad \kappa^2 = 2r_e\frac{2\pi R}{v_g} \tag{2.5}$$

Time domain analyses based on these equations show part of the frequency response of single-MRMs [17, 18]. To further reveal its gain and bandwidth limitation, we take the

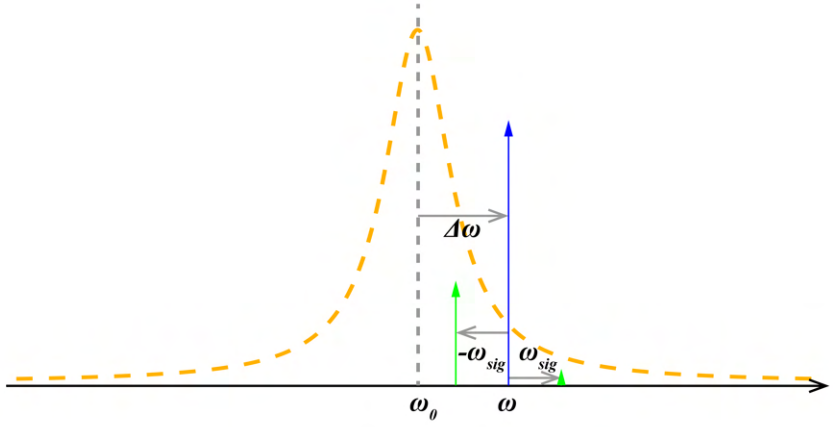

Figure 2.3: Spectral diagram denoting the operating parameters of a single MRM. Orange dashed line: cavity optical power response; blue arrow: laser tone; green arrows: sidebands generated by the electrical modulation; ω_0: resonance frequency; $\Delta\omega = \omega - \omega_0$: detuned frequency; ω_{sig}: modulation frequency

equation in [18] assuming a cosine wave at angular frequency ω_{sig} is modulating the single-MRM, causing the instant resonance frequency to change with a swing of $\delta\omega_m$, and we only keep the response to refractive index modulation by decoupling the electrical bandwidth due to the parasitic resistance of the modulator:

$$\begin{aligned} &S_{thru}(t) \propto \tilde{E}_{thru}(t) \\ &= E_{in}e^{j\omega t}\left\{\frac{j\Delta\omega + r_o - r_e}{j\Delta\omega + r_o + r_e} - \frac{jr_e\delta\omega_m}{(j\Delta\omega + r_o + r_e)^2 + \omega_{sig}^2}\left[cos(\omega_{sig}t) + \frac{\omega_{sig}sin(\omega_{sig}t)}{j\Delta\omega + r_o + r_e}\right]\right\} \end{aligned} \tag{2.6}$$

Here $\Delta\omega$ is the frequency detuning from the resonance frequency ω_0, and $\delta\omega_m$ is proportional to the swing of the sine wave. The terms containing $cos(\omega_{sig}t)$ and $sin(\omega_{sig}t)$ can also be expressed as a combination of $e^{\pm j\omega_{sig}t}$ representing the two sidebands in the optical domain:

$$\begin{aligned} \tilde{E}_{thru}(t) &\equiv E_{in}e^{j\omega t}\left(\tilde{c}_0 + \tilde{c}_{SB+}e^{j\omega_{sig}t} + \tilde{c}_{SB-}e^{-j\omega_{sig}t}\right) \\ \tilde{c}_0 &= \frac{j\Delta\omega + r_o - r_e}{j\Delta\omega + r_o + r_e} \\ \tilde{c}_{SB+} &= \frac{-j\delta\omega_m}{2}\cdot\frac{r_e}{(r_o + r_e + j\Delta\omega)[r_o + r_e + j(\Delta\omega + \omega_{sig})]} \\ \tilde{c}_{SB-} &= \frac{-j\delta\omega_m}{2}\cdot\frac{r_e}{(r_o + r_e + j\Delta\omega)[r_o + r_e + j(\Delta\omega - \omega_{sig})]} \end{aligned} \tag{2.7}$$

The spectral diagram containing the two sidebands are shown in Fig. 2.3. Intuitively the modulation information is contained in these two sidebands. In the next chapter, we will prove that we can build a link so that the amplitude of the output photo current is pro-

portional to the sideband conversion efficiency (SCE) $c_{SB\pm}$, which are defined as the absolute values of $\tilde{c}_{SB\pm}$. For the RF / mm-wave applications, only one sideband will be utilized in order to generate the baseband signal at the photodetector, and by observing that $c_{SB+}(-\Delta\omega) = c_{SB+}(\Delta\omega)$, we only need to look into one of these two coefficients:

$$c_{SB} \equiv c_{SB+} = \frac{\delta\omega_m}{2} \cdot \frac{r_e}{\sqrt{\left[(r_o+r_e)^2+\Delta\omega^2\right]\left[(r_o+r_e)^2+(\Delta\omega+\omega_{sig})^2\right]}} \tag{2.8}$$

There are four design and operating parameters for the ring modulator: $\Delta\omega, r_e, r_o$ and $\delta\omega_m$, and we will focus on the first three parameters as c_{SB+} is proportional to $\delta\omega_m$. The equation shows that any non-zero combination of $(\Delta\omega, \omega_{sig})$ leads to lower c_{SB}, so can look into the case when $\Delta\omega = 0$:

$$c_{SB}(\omega_{sig})|_{\Delta\omega=0} = \frac{\delta\omega_m}{2} \cdot \frac{r_e}{(r_o+r_e)^2} \cdot \frac{1}{\sqrt{1+\left(\frac{\omega_{sig}}{r_o+r_e}\right)^2}} \tag{2.9}$$

This represents the only curve that achieves the highest SCE among the full range of $\Delta\omega$ when r_o, r_e are fixed, with the highest value at $\omega_{sig} = 0$ and its 3 dB bandwidth are:

$$\begin{aligned} \omega_{3dB} &= r_o + r_e \\ c_{SB}(\omega_{sig}=0)|_{\Delta\omega=0} &= \frac{\delta\omega_m r_e}{2(r_o+r_e)^2} = \frac{\delta\omega_m}{2} \cdot \frac{r_e}{r_o+r_e} \cdot \frac{1}{\omega_{3dB}} \end{aligned} \tag{2.10}$$

Practically, $\frac{r_e}{r_o+r_e}$ is around $\frac{1}{2}$ which corresponds to the critical coupling, and in this case the SCE can also be expressed as:

$$c_{SB}(\omega_{sig}=0)|_{\Delta\omega=0} \approx \frac{\delta\omega_m}{4\omega_{3dB}} \approx \frac{\delta\omega_m}{8r_o} \tag{2.11}$$

The bandwidth design specification gives the baseline SCE for a single-MRM at low frequencies. At higher frequencies, however, the SCE starts to roll off, and the goal is to find out the optimal combination $(r_o, r_e, \Delta\omega)$ that maximizes c_{SB}. For the roll-off of c_{SB} from its baseline value in Eq. 2.10, Fig. 2.4 shows the relationship between it and the normalized modulation and detuning frequency. The contour plot indicates for a modulation frequency that is decently low, e.g. less than 2 when it is normalized to $(r_o + r_e)$, the tuning around $-\frac{1}{2}\omega_{sig}$ enables the highest c_{SB}. If the normalized frequency exceeds this threshold, the optimal detuning seems to get closer to $-\omega_{sig}$ or 0. This observation can be verified by solving the extrema of Eq. 2.8 and take the extrema that represent the maximum value:

$$\begin{aligned} &\frac{\partial}{\partial(\Delta\omega_{sig})}\left\{\left[(r_o+r_e)^2+\Delta\omega^2\right]\left[(r_o+r_e)^2+(\Delta\omega+\omega_{sig})^2\right]\right\} = 0 \\ &\Rightarrow \left(\Delta\omega + \frac{1}{2}\omega_{sig}\right)\left[\Delta\omega^2 + \omega_{sig}\Delta\omega + (r_o+r_e)\right] = 0 \end{aligned} \tag{2.12}$$

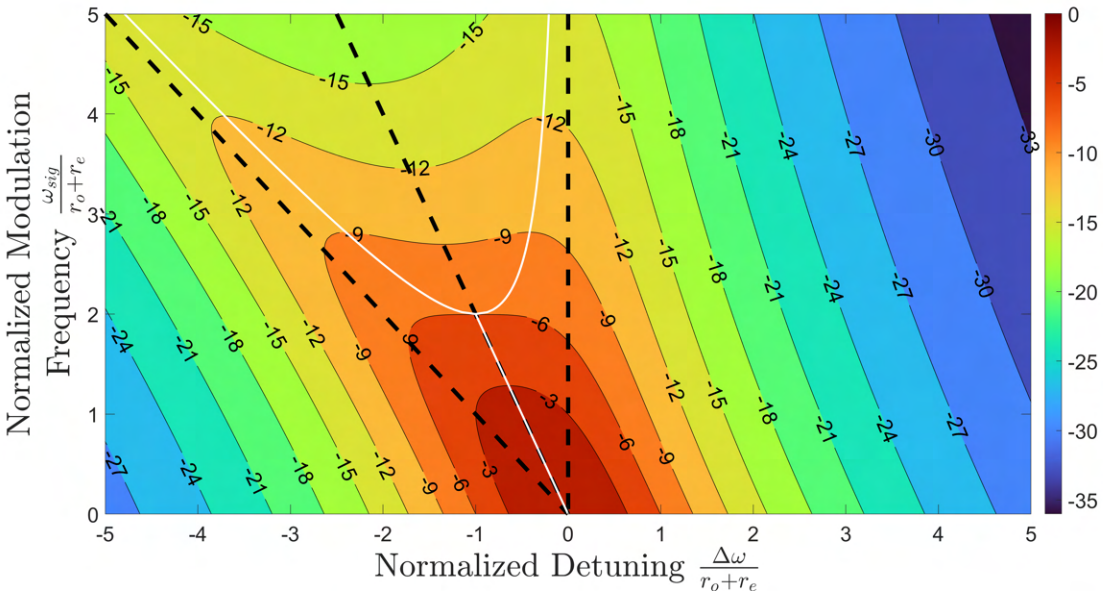

Figure 2.4: Roll-off [dB] of c_{SB} with respect to normalized modulation frequency $\frac{\omega_{sig}}{r_o+r_e}$ and normalized detuning $\frac{\Delta\omega}{r_o+r_e}$. White curves: set of $(\omega_{sig}, \Delta\omega)$ that maximizes c_{SB} for the specific ω_{sig}. Black dashed lines: lines that the white curves get close to

There are two cases for solving this equation. If $\omega_{sig} < 2(r_o + r_e)$, there is only one solution and it leads to the maximum SCE:

$$\begin{aligned} \Delta\omega_{opt0} &= -\frac{1}{2}\omega_{sig} \\ c_{SB}|_{\Delta\omega=\Delta\omega_{opt0}} &= \frac{\delta\omega_m}{2} \cdot \frac{r_e}{(r_o+r_e)^2} \cdot \frac{1}{1+\frac{\omega_{sig}^2}{4(r_o+r_e)^2}} \end{aligned} \tag{2.13}$$

If $\omega_{sig} \geq 2(r_o+r_e)$, the previous solution still exist but the extrema will be the local minima. Instead, we will have the other two solutions that represent the maximum value are these two values are the same:

$$\begin{aligned} \Delta\omega_{opt\pm} &= \frac{-\omega_{sig} \pm \sqrt{\omega_{sig}^2 - 4(r_o+r_e)^2}}{2} \\ c_{SB}|_{\Delta\omega=\Delta\omega_{opt+}} &= c_{SB}|_{\Delta\omega=\Delta\omega_{opt-}} = \frac{\delta\omega_m r_e}{2(r_o+r_e)^2} \cdot \frac{r_o+r_e}{\omega_{sig}} \end{aligned} \tag{2.14}$$

These results are plotted in Fig. 2.5, where Fig. 2.5a shows several equal-ω_{sig} sections from the contour plot in Fig. 2.4 and visualizes the split of the optimal $\Delta\omega$ when ω_{sig} increases, and Fig. 2.5b presents the "best" SCE we can achieve by tracking the detuning with the

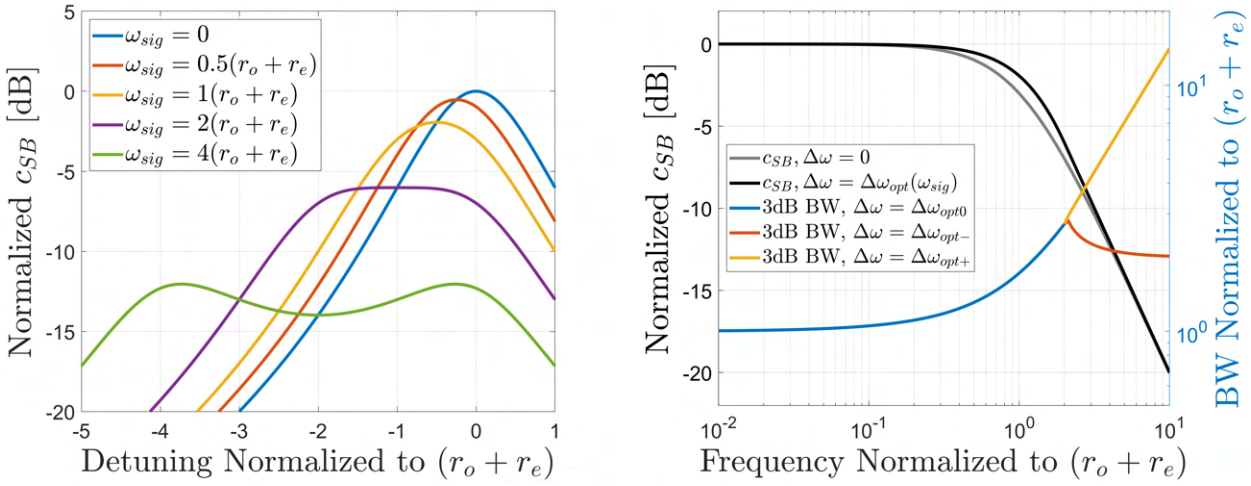

(a) Normalized c_{SB} v.s. detuning with different modulation frequency

(b) c_{SB} and bandwidth v.s. normalized modulation frequency

Figure 2.5: Normalized sideband conversion efficiency in different scenarios

modulation frequency. From the plot, the detuning improves the SCE to some extent around the original 3dB bandwidth $(r_o + r_e)$, but this improvement disappears when the modulation frequency is far above. Compared to the baseline SCE in Eq. 2.10, the roll-off when $\omega_{sig} > 2(r_o + r_e)$ will be:

$$\frac{c_{SB,opt}(\omega_{sig} \to 0)}{c_{SB,opt}(\omega_{sig})} = \frac{\omega_{3dB}}{\omega_{sig}} \tag{2.15}$$

Eq. 2.15 reveals that there is a fundamental conversion gain degradation for single-MRM when it is modulated by narrow-band signals with bandwidth much lower than its carrier frequency. Engineering r_o and r_e can potentially boost the 3dB frequency, but SCE at ω_{sig} does not benefit after some point, since for the same drive voltage and $\delta\omega_m$, the sharpness of the Lorentzian shape would be reduced, providing a similar trade-off to the one well-known in electronics as the gain-bandwidth product reformulated here as a "sharpness-bandwidth" product. This penalty of single-MRM strongly motivates developing novel electro-optical modulators.

2.3 Dual Microring Modulator

Dual-microring modulators [19–24] are reported to be able to address the narrow band modulation that is a challenge for single-MRM. The diagram of a basic dual-ring modulator is shown in Fig. 2.6 containing two couplers between the two identical cavities and the bus waveguide, the steady-state response can be derived from the equation similar to Eq. 2.1,

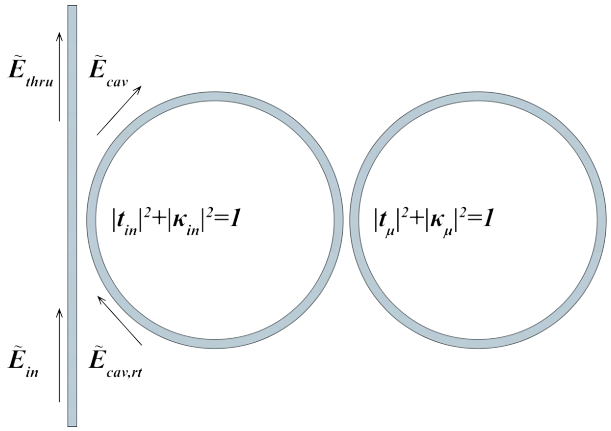

Figure 2.6: Diagram of a basic dual microring modulator

with the through-port response of a single MRM incorporated into the round-trip transfer function of the ring closer to the bus waveguide:

$$\begin{bmatrix} \tilde{E}_{thru} \\ \tilde{E}_{cav} \end{bmatrix} = \begin{bmatrix} t_{in} & \kappa_{in} \\ -\kappa_{in}^* & t_{in}^* \end{bmatrix} \begin{bmatrix} \tilde{E}_{in} \\ \tilde{E}_{cav,rt} \end{bmatrix}$$
$$\tilde{E}_{cav,rt} = t_{E,single} a_{rt} e^{j\phi_{rt}} \tilde{E}_{cav} = \frac{t_\mu - a_{rt} e^{j\phi_{rt}}}{1 - t_\mu^* a_{rt} e^{j\phi_{rt}}} a_{rt} e^{j\phi_{rt}} \tilde{E}_{cav} \tag{2.16}$$

Based on Eq. 2.16, Fig. 2.7 presents example of the steady-state through port power of the dual-MRM with varied κ_μ, and for simplicity the critically coupled condition is assumed, which leads to $\kappa_{in}^2 = 1 - a_{rt}^4$. One observation is that in case the round-trip phase shift inside both rings are multiples of 2π, which corresponds to on-resonance state for the single-MRM, the dual-MRM as one device is off-resonance. The reason is that since the cavity farther away from the waveguide is on resonance, the power at its through port, or say in the cavity closer to the bus waveguide, is zero. Thus, there is no E-field interaction between the dual-cavity system and the bus waveguide, and this leads to the off-resonance situation. With the mutual coupling, two resonance notches appear above and below that of the isolated single-MRM, which are known as two supermodes. In most cases t_μ of the mutual coupling can be modeled as a real number, split has positive correlation with the mutual coupling strength shown in Fig. 2.7a, which is analogous to coupled inductor-capacitor tanks [25–28] as illustrated in Fig. 2.8, since both systems follow the electromagnetic wave equations and have interaction between two resonance subsystems. The supermode frequencies follow the following equation:

$$\begin{aligned} \omega_- &= \omega_0 - \omega_\mu \\ \omega_+ &= \omega_0 + \omega_\mu \\ \omega_\mu &= |\kappa_\mu| \frac{v_g}{2\pi R} \end{aligned} \tag{2.17}$$

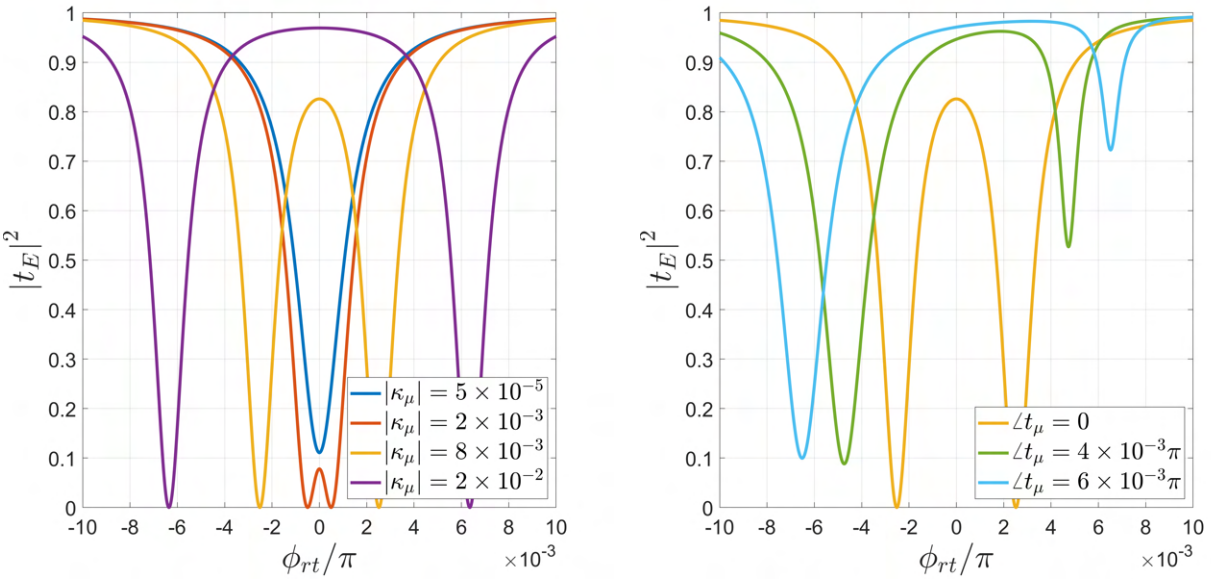

(a) $\angle t_\mu = 0$ (b) $|\kappa_\mu| = 8 \times 10^{-3}$

Figure 2.7: Normalized through port power of a dual-MRM behavioral model, where $t_\mu = \sqrt{1 - |\kappa_\mu|^2} e^{j\angle t_\mu}$

where ω_0 is the intrinsic resonance frequency of the two rings when they are not mutually coupled. In some other cases, t_μ might be a complex number, and the split of the two notches is also related to its angle, though the response becomes asymmetric, as shown in Fig. 2.7b.

As Fig. 2.5b illustrates that the gain of a single MRM peaks at the detuning frequency and is maximized when the detuning is zero, the two notches in Fig. 2.7 imply that if the laser is parked at one of them, and the modulation frequency happens to be equal to the frequency of the split, then the gain can be potentially maximized. The intuition is verified by the analysis [19] by applying the time-domain CMT model to a more generalized dual-MRM, which reveals two supermodes corresponding to the two notches. According to it, if a dual-MRM is modulated by the push-pull signals at ω_{RF} so that the instant resonance frequencies of the two rings are modulated in the form of $\omega_{res\pm} = \omega_0 \pm \frac{\delta\omega_m}{2} cos(\omega_{RF} t)$, and if the laser frequency ω plus either one of the potential sideband frequencies $\omega \pm \omega_{RF}$ are close to the two supermodes, a relatively strong optical sideband will be generated, and the ratio

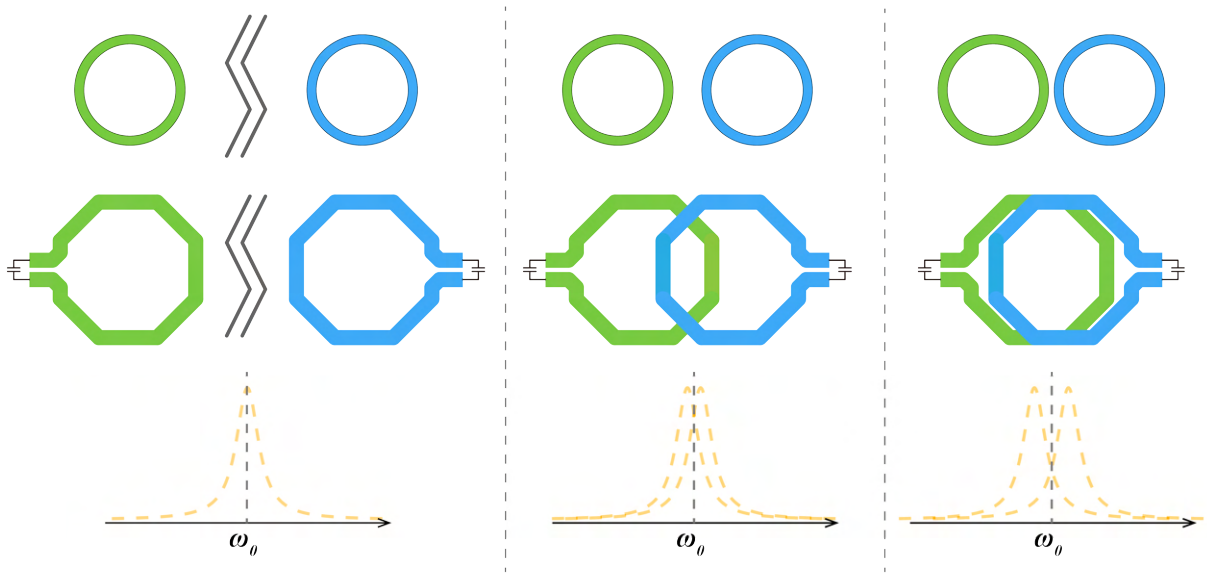

Figure 2.8: Illustration of resonance frequency split caused by mutual coupling
Left: isolated; Middle: weak couple; Right: strong couple

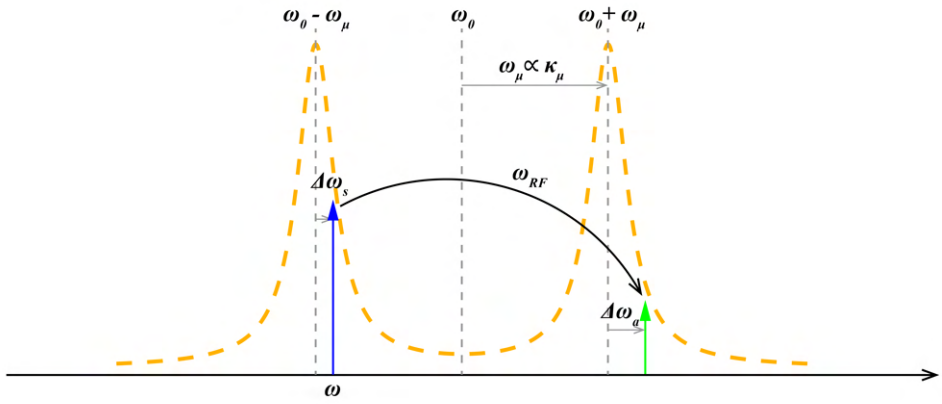

Figure 2.9: Spectral diagram denoting the operating parameters of a dual MRM.
Orange dashed line: cavity optical power response; blue arrow: laser tone;
green arrow: sideband generated by the electrical modulation;
ω_0: intrinsic resonance frequency; $\omega_0 \pm \omega_\mu$: coupled resonance frequencies (supermodes);
$\Delta\omega_s, \Delta\omega_a$: detunings from the symmetric / asymmetric supermodes;
ω_{RF}: RF modulation frequency

of the optical sideband power to the pump power is derived as:

$$\begin{aligned} G_{SB} &\equiv \frac{P_{SB}}{P_{pump}} \\ &= \frac{\frac{1}{4} r_{e,s} r_{e,a} \delta\omega_m^2}{\left[(r_o + r_{e,a})\Delta\omega_s + (r_o + r_{e,s})\Delta\omega_a\right]^2 + \left[(r_o + r_{e,s})(r_o + r_{e,a}) + \left(\frac{\delta\omega_m}{4}\right)^2 - \Delta\omega_s \Delta\omega_s\right]^2} \end{aligned} \tag{2.18}$$

Here r_o is the decay rate of the standalone cavities assuming that they are not mutually coupled, $r_{e,s}, r_{e,a}$ are the coupling rates of the symmetric and asymmetric supermodes, and $\Delta\omega_s, \Delta\omega_a$ are the detuning from the symmetric and asymmetric resonance, denoted in Fig. 2.9. In case of basic dual ring modulator shown in Fig. 2.6 where $r_{e,s} = r_{e,a}$, if they are designed to have $r_{e,s} = r_{e,a} = r_o$ which optimizes G_{SB} in the linear regime, the equation is simplified to:

$$\begin{aligned} G_{SB} &= \frac{\frac{1}{4} r_o^2 \delta\omega_m^2}{\left[2r_o(\Delta\omega_s + \Delta\omega_a)\right]^2 + \left[4r_o^2 + (\frac{\delta\omega_m}{4})^2 - \Delta\omega_s \Delta\omega_s\right]^2} \\ &= \frac{\delta\omega_m^2}{64 r_o^2 \left[1 + (\frac{\Delta\omega_s^2 + \Delta\omega_a^2}{4r_o^2} + \frac{\Delta\omega_s^2 \Delta\omega_a^2}{16 r_o^4}) + (\frac{1}{32} - \frac{\Delta\omega_s \Delta\omega_a}{128 r_o^2})(\frac{\delta\omega_m}{r_o})^2 + \frac{1}{4096}(\frac{\delta\omega_m}{r_o})^4\right]} \end{aligned} \tag{2.19}$$

And in case $\Delta\omega_s, \Delta\omega_a, \delta\omega_m \ll r_o$, meaning that both the detuning and the modulation is weak and the modulation is in the linear region, we have the very simplified equation along the sideband conversion efficiency we defined:

$$\begin{aligned} G_{SB}^{linear} &= \frac{\delta\omega_m^2}{64 r_o^2} \\ c_{SB}^{linear} &= \sqrt{G_{SB}^{linear}} = \frac{\delta\omega_m}{8 r_o} \end{aligned} \tag{2.20}$$

The expression equals that in Eq. 2.11, proving that by engineering the mutual coupling to match the carrier frequency of the signal, the dual-MRM provides the same SCE as a single-MRM for the low-frequency signal.

The 3 dB bandwidth of the dual-MRM can also be derived from Eq. 2.18. The presumption is that the modulation is weak, and either the pump laser or the sideband is aligned with a supermode while the other is slightly misaligned, by solving the equation:

$$G_{SB}(\Delta\omega_s', \Delta\omega_a = \delta\omega_m = 0) = G_{SB}(\Delta\omega_s = \delta\omega_m = 0, \Delta\omega_a') = \frac{1}{2} G_{SB}(\Delta\omega_s = \Delta\omega_a = \delta\omega_m = 0) \tag{2.21}$$

and the solution is:

$$\begin{aligned} \Delta\omega_s' &= \pm(r_o + r_{e,s}) \\ \Delta\omega_a' &= \pm(r_o + r_{e,a}) \end{aligned} \tag{2.22}$$

Similarly we have $r_{e,s} = r_{e,a} = r_o$ in most cases, and finally the expression of the 3 dB bandwidth is:

$$\omega_{3dB} = 2\Delta\omega'_s = 2\Delta\omega'_a = 4r_o \tag{2.23}$$

Eq. 2.17 and Eq. 2.23 together explain the benefits of the dual-MRM: for the RF signal with specific bandwidth and carrier frequency, the target is to design a split that equals the carrier frequency; and for the cavity, we would like to have $4r_o$ slightly higher than the RF bandwidth so that the in-band signal does not suffer from in-band gain penalty, and that we also achieves the best possible SCE. Notice that the split and the bandwidth are determined by two decoupled design parameters so there is no design "trade-off" where we need to sacrifice one performance metric for the other.

2.4 Triple Microring Modulator

While the dual MRM resolves the issue of narrow band modulation at high frequencies, for any one design variant, its optimal modulation frequency is determined at the time of the design by engineering the mutual coupling coefficient κ_μ. If this frequency changes due to process variation, or if the entire system is desired to operate with a variable carrier frequency, the tunability is highly preferred. Although we can tune the intrinsic resonance frequencies of two rings to modify the resonance frequency split, this tuning confronts the following challenges:

- The heater power applied to the two cavities can be decomposed to a common-mode term and a differential-mode one. The common-mode term shifts the two supermode frequencies together as an entity, so only the differential-mode term is the one that controls the split. Noticing that the two cavities are identical if we ignore the location of the bus waveguide, a positive and a negative differential term of the same strength give us the same split. Intuitively, making the intrinsic resonance different should make the split larger, so the split of the dual-MRM has a lower limit through this differential detuning, which is the split where the two cavities have the same resonance frequency.

- The tuning can be conducted through changing the DC bias voltage or the heater power. DC bias voltage changes the decay rate of the cavity which is not preferred. Thermal tuning has a wider tuning range and it does not have a significant impact on the decay rate, but the ring cavities are so close that the heater power will couple, which leads to larger required tuning strength compared to the thermal tuning of the single-MRM, as the dual-MRM requires a differential thermal tuning.

Therefore, a better tuning technique needs to be implemented to tune the split in both directions in case we do not have good control over the process variation, and if possible avoid differential thermal tuning of the cavities that are physically close. Inspired from Eq. 2.17, the tuning can be realized if κ_μ is controlled, and this motivates the design of a triple-microring modulator.

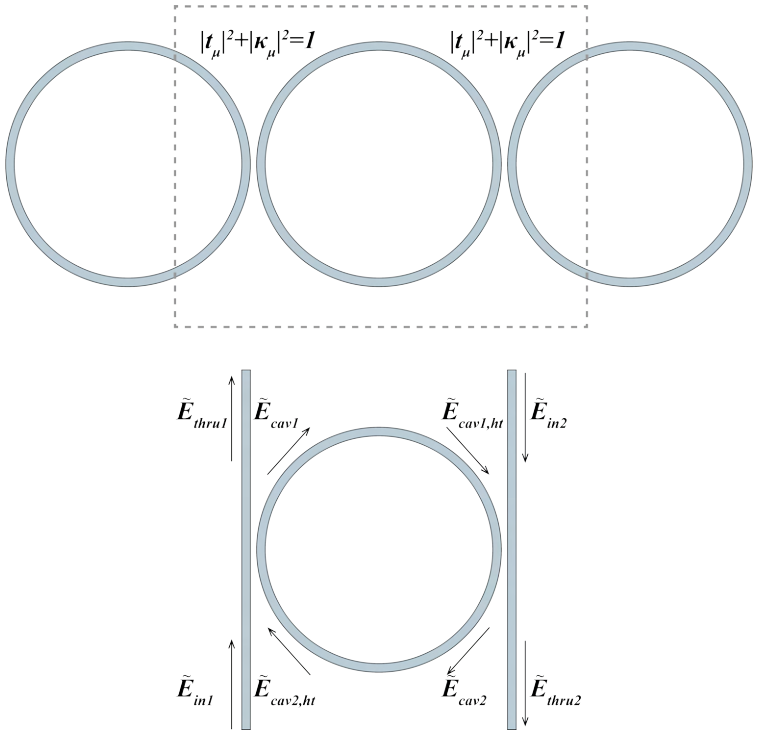

Figure 2.10: Top: a triple-cavity system; bottom: central cavity with signal names marked

Fig. 2.10 shows the diagram of a triple-cavity system, where the mutual coupling coefficients between the central cavity to the two outside cavities are the same: $\kappa_{\mu,left} = \kappa_{\mu,right} = \kappa_\mu$. Intuitively, the mutual couplings between the central ring and the outside rings are still κ_μ, but κ_{eq}, the effective coupling between the outside rings depends on the round-trip phase shift ϕ_{rt}. To find out its expression, we can take out the central cavity and the two inter-cavity couplers as shown in Fig. 2.10:

$$\begin{bmatrix} \tilde{E}_{thru1} \\ \tilde{E}_{thru2} \end{bmatrix} = \begin{bmatrix} t_{eq} & \kappa_{eq} \\ -\kappa_{eq}^* & t_{eq}^* \end{bmatrix} \begin{bmatrix} \tilde{E}_{in1} \\ \tilde{E}_{in2} \end{bmatrix} \tag{2.24}$$

For simplicity, we can treat the central ring as two sections of phase shifters with no loss, so the two inter-cavity couplers gives us:

$$\begin{aligned}
\begin{bmatrix}\tilde{E}_{thru1}\\ \tilde{E}_{cav1}\end{bmatrix} &= \begin{bmatrix} t_\mu & \kappa_\mu \\ -\kappa_\mu^* & t_\mu^* \end{bmatrix}\begin{bmatrix}\tilde{E}_{in1}\\ \tilde{E}_{cav2,ht}\end{bmatrix} = \begin{bmatrix} t_\mu & \kappa_\mu \\ -\kappa_\mu^* & t_\mu^* \end{bmatrix}\begin{bmatrix}1 & 0\\ 0 & e^{j\phi_{ht}}\end{bmatrix}\begin{bmatrix}\tilde{E}_{in1}\\ \tilde{E}_{cav2}\end{bmatrix} \\
&= \begin{bmatrix} t_\mu & \kappa_\mu e^{j\phi_{ht}} \\ -\kappa_\mu^* & t_\mu^* e^{j\phi_{ht}} \end{bmatrix}\begin{bmatrix}\tilde{E}_{in1}\\ \tilde{E}_{cav2}\end{bmatrix} \\
\begin{bmatrix}\tilde{E}_{thru2}\\ \tilde{E}_{cav2}\end{bmatrix} &= \begin{bmatrix} t_\mu & \kappa_\mu \\ -\kappa_\mu^* & t_\mu^* \end{bmatrix}\begin{bmatrix}\tilde{E}_{in2}\\ \tilde{E}_{cav1,ht}\end{bmatrix} = \begin{bmatrix} t_\mu & \kappa_\mu \\ -\kappa_\mu^* & t_\mu^* \end{bmatrix}\begin{bmatrix}1 & 0\\ 0 & e^{j\phi_{ht}}\end{bmatrix}\begin{bmatrix}\tilde{E}_{in2}\\ \tilde{E}_{cav1}\end{bmatrix} \\
&= \begin{bmatrix} t_\mu & \kappa_\mu e^{j\phi_{ht}} \\ -\kappa_\mu^* & t_\mu^* e^{j\phi_{ht}} \end{bmatrix}\begin{bmatrix}\tilde{E}_{in2}\\ \tilde{E}_{cav1}\end{bmatrix}
\end{aligned} \tag{2.25}$$

Here ϕ_{ht} equals half of ϕ_{rt} which is the round-trip phase shift. After canceling $\tilde{E}_{cav1}$ and $\tilde{E}_{cav2}$ in Eq. 2.25, we have:

$$\begin{aligned}
t_{eq} &= \frac{t - t^* e^{j\phi_{rt}}}{1 - t_\mu^{*2} e^{j\phi_{rt}}} \\
|\kappa_{eq}| &= \frac{|\kappa_\mu|^2}{\left|1 - t_\mu^{*2} e^{j\phi_{rt}}\right|}
\end{aligned} \tag{2.26}$$

We can see that t_{eq} is no longer guaranteed to be a real value. In addition, κ_{eq} highly depends on the round-trip phase shift ϕ_{rt}, with its minimum and maximum value equal to:

$$\begin{aligned}
min\{|\kappa_{eq}|\} &= \frac{|\kappa_\mu|^2}{1 + |t_\mu^*|^2} \approx \frac{1}{2}|\kappa_\mu|^2 \\
max\{|\kappa_{eq}|\} &= \frac{|\kappa_\mu|^2}{1 - |t_\mu^*|^2} = 1
\end{aligned} \tag{2.27}$$

With interactions in between, the triple-cavity system has three resonance supermode frequencies at which the optical power circulates with minimum loss, and at which the notches can be observed from the through port optical power. Since the interactions can be controlled by the phase shift of the central cavity, the splits between the three notches are also tunable, as plotted in Fig. 2.11.

For triple-MRMs, in addition to ω_μ that is related to the splits of the three supermodes, another auxiliary parameter T representing the detuning will be introduced as well, their expressions are:

$$\begin{aligned}
\omega_\mu &= |\kappa_\mu| \frac{v_g}{2\pi R} \\
T &= \frac{\Delta\omega_{D0} + j(r_{o,m} - r_o)}{2} - \sqrt{\left[\frac{\Delta\omega_{D0} + j(r_{o,m} - r_o)}{2}\right]^2 + 2\omega_\mu^2}
\end{aligned} \tag{2.28}$$

Here the the decay rates of the outside cavities are both r_o while the decay rate of the middle cavity is $r_{o,m}$. The outside cavities also have the same intrinsic resonance frequency ω_0 and

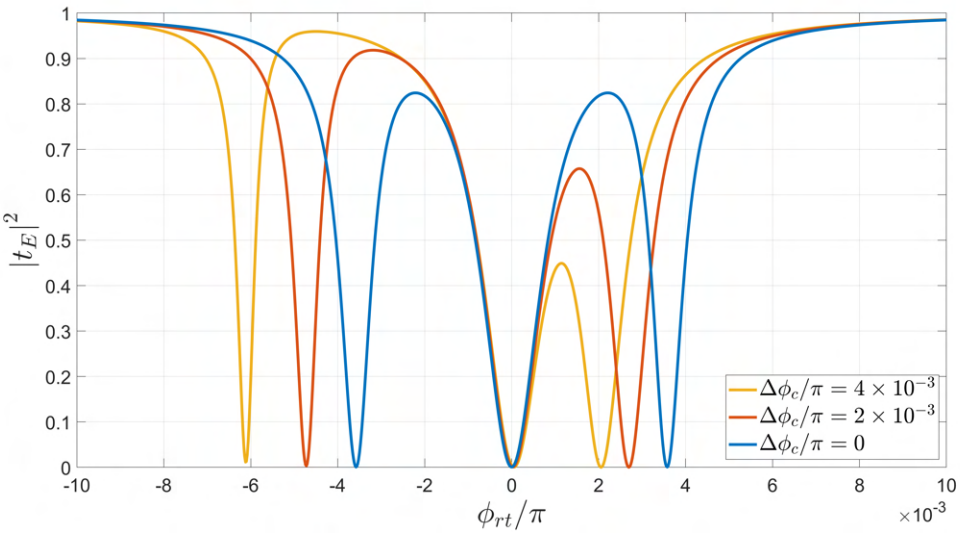

Figure 2.11: Normalized through port power of a triple-MRM behavioral model with central ring phase shift detuning $\Delta\phi_c$

the central cavity has its resonance frequency detuned by $\Delta\omega_{D0}$ from ω_0. Using the similar time-domain CMT model, the three resonance frequencies are:

$$\begin{aligned} \omega_- &= \omega_0 + \frac{2\omega_\mu^2}{T} \\ \omega_\cdot &= \omega_0 \\ \omega_+ &= \omega_0 - T \end{aligned} \tag{2.29}$$

And with the identical cavity assumption meaning $r_o = r_{o,m}$, the sideband conversion efficiency in terms of power like Eq. 2.30 for dual-MRM is:

$$G_{SB} = \frac{\frac{1}{4}\frac{2\omega_\mu^2}{2\omega_\mu^2+T^2} r_{e,o} r_{e,m} \delta\omega_m^2}{\left[(r_o + r_{e,o})\Delta\omega_1 + (r_o + r_{e,m})\Delta\omega_2\right]^2 + \left[(r_o + r_{e,o})(r_o + r_{e,m}) + \frac{2\omega_\mu^2}{2\omega_\mu^2+T^2}\left(\frac{\delta\omega_m}{4}\right)^2 - \Delta\omega_1\Delta\omega_2\right]^2} \tag{2.30}$$

In this equation, $\Delta\omega_1$ and $\Delta\omega_2$ still represent the misalignment between the pump laser or the sideband and the supermodes, $r_{e,o}$ is the external coupling rate of the outside cavities and $r_{e,m}$ is the external coupling rate of the middle cavity. A simplified case would be when the misalignment is zero so G_{SB} reaches its maximum value, $\delta\omega_m \ll r_o$ representing small signal modulation, and $\Delta\omega_{D0} = 0$ indicating zero central cavity detuning, where we have:

$$G_{SB} = \frac{\frac{1}{8} r_{e,o} r_{e,m} \delta\omega_m^2}{(r_o + r_{e,o})^2 (r_o + r_{e,m})^2} \tag{2.31}$$

Depending on what we are trying to optimize, the values of $r_{e,o}$ and $r_{e,m}$ might vary but generally this conversion efficiency of the triple-MRM is approximately 3 dB lower than that of the dual-MRM, and its 3 dB bandwidth is similar to or slightly higher than that of the dual-MRM.

2.5 Tunability and Conversion Efficiency Comparison

Although the triple-MRM claims to have wider tuning range, especially for its ability to tune the split lower than the limit of a dual-MRM, its tuning range, together with the sideband conversion efficiency after tuning, still needs to be verified. From Eq. 2.17, a triple-MRM with the identical cavity assumption originally has a split of $\omega_{RF0} = T_0 = \sqrt{2}\omega_\mu$ when $\Delta\omega_{D0} = 0$, and if it is detuned for a different frequency ω_{RF}, we have

$$\begin{aligned} \omega_{RF} &= \frac{\Delta\omega_{D0}}{2} - \sqrt{\omega_{RF0}^2 + \frac{1}{4}\Delta\omega_{D0}^2} \\ \Rightarrow \frac{\Delta\omega_{D0}}{\omega_{RF0}} &= \frac{\omega_{RF}}{\omega_{RF0}} - \frac{\omega_{RF0}}{\omega_{RF}} \end{aligned} \tag{2.32}$$

There is also another solution which is the inverse, in which case $\frac{2\omega_\mu^2}{T}$ instead of T is tuned to the target ω_{RF}. Similarly, for a dual-MRM, if one of the cavities has its resonance detuned by $\frac{1}{2}\Delta\omega_{D0}$ and the other detuned by $-\frac{1}{2}\Delta\omega_{D0}$, we have: :

$$\begin{aligned} \omega_{RF} &= \sqrt{\omega_{RF0}^2 + \Delta\omega_{D0}^2} \\ \Rightarrow \frac{\Delta\omega_{D0}}{\omega_{RF0}} &= \sqrt{\left(\frac{\omega_{RF}}{\omega_{RF0}}\right)^2 - 1} \end{aligned} \tag{2.33}$$

$|\Delta\omega_{D0}|$ represents the required detuning strength which is linearly dependent on the heater power, so we would like to have it reasonably small, which benefits the total power consumption. The comparison between the dual-MRM and triple-MRM is shown in Fig. 2.12a, where we can observe that triple-MRM requires less detuning strength than dual-MRM. In addition, triple-MRM can handle the cases where $\omega_{RF} < \omega_{RF0}$ whereas dual-MRM cannot.

However, analysis [29] implies that there are also cases where the dual-MRM outperforms the triple-MRM. Fig. 2.12 shows the performance of a dual-MRM and a triple-MRM originally targeting the same frequency split, where the green and the blue curves represent the frequency response of the ring variant without detuning, and the red and the dark red curves are the envelopes of their peak SCE with respect to the detuned frequency split. The dual-MRM has about 2 dB higher SCE because of less lossy mode profiles, and though the dual-MRM's envelope curve decreases faster with the increasing ω_{RF}/ω_{RF0}, its absolute SCE is still beyond that of the triple-MRM. Nevertheless, triple-MRM still has a decent performance considering its much wider tuning range. In addition, the analysis assumes that the

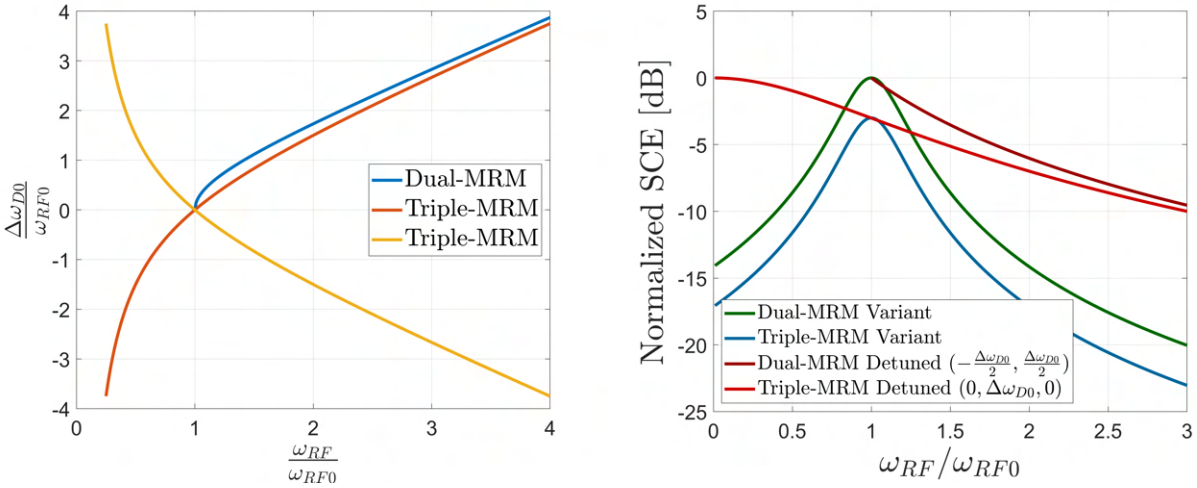

(a) Required detuning strength

(b) Normalized SCE with detuning [29]

Figure 2.12: Detuning performance comparison

triple-MRM has equally lossy central cavity, and as the central cavity is not modulated by the high speed signal, it can have light doping profile to form a less lossy passive cavity, which boosts the triple-MRM's SCE to nearly the same as that of the dual-MRM.

2.6 Chapter Summary

We summarize here the performance of different types of MRM for RF/millimeter-wave modulation. Single-MRM is an important building block for modern photonic links, and although its SCE is boosted because of the resonance cavity, it is fundamentally limited by the inherent gain-bandwidth trade-off. This makes it particularly unsuitable for handling narrow-band signals with a high carrier frequency, due to the fact that either the pump laser or the sideband will fall out of its optical band if the decay rate is low, and the SCE is poor if we target a large decay rate to make the optical bandwidth high. Dual-MRM and triple-MRM however, resolve this limitation. Additional rings increase the design degrees of freedom enabling separate control of the resonance split frequency (to the RF carrier) from the resonance bandwidth (to the RF signal bandwidth). This allows them to achieve a similar SCE while handling a narrow band RF/mm-wave signal, compared to a single-MRM that handles the baseband signal of the same bandwidth. The dual-MRM has higher SCE than the triple-MRM, while the triple-MRM has a wider tuning range.

Chapter 3

Link Performance Analysis

In this chapter, the link performance analyses, including but not limited to linearity, gain and noise, will be established for both the circuits and the photonics, which together provide the direction for the electronic-photonic system design.

3.1 Conversion Gain

The simplified photonic link element for the proposed architecture is shown in Fig. 3.1. Where one branch of the laser signal $\tilde{E}_{in}$ passes through an MRM to generate the modulated signal $\tilde{E}_{thru}$, and get mixed with a reference signal $\tilde{E}_{ref}$ via a 2×2 - coupler [30] to generate the signal pair $\tilde{E}_{\pm}$ that reach the balanced photodetector pair. The general output current follows the equation below:

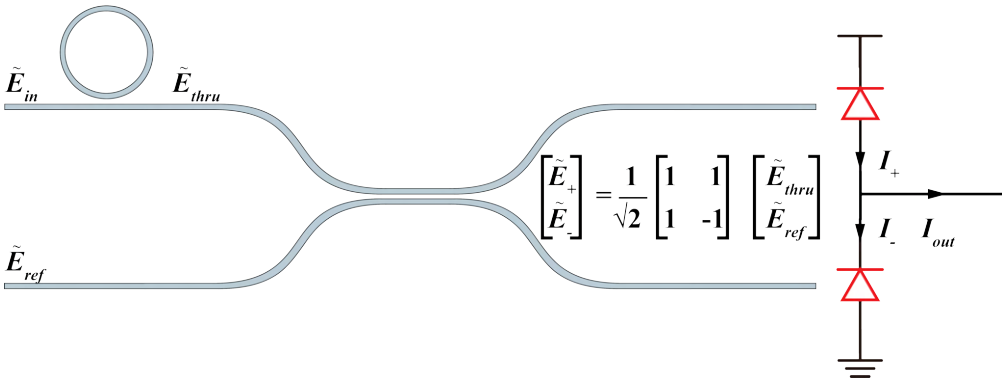

Figure 3.1: Diagram of a MRM-based coherent link

$$\begin{aligned} I_{out} &= I_+ - I_- \\ &= \mathcal{R}_{PD}(\tilde{E}_+\tilde{E}_+^* - \tilde{E}_-\tilde{E}_-^*) \\ &= \frac{1}{2}\mathcal{R}_{PD}\left[(\tilde{E}_{thru} + \tilde{E}_{ref})(\tilde{E}_{thru}^* + \tilde{E}_{ref}^*) - (\tilde{E}_{thru} - \tilde{E}_{ref})(\tilde{E}_{thru}^* - \tilde{E}_{ref}^*)\right] \\ &= \mathcal{R}_{PD}(\tilde{E}_{thru}\tilde{E}_{ref}^* + \tilde{E}_{thru}^*\tilde{E}_{ref}) \end{aligned} \tag{3.1}$$

When it is used in regular high speed serial links where the single-MRM is used and the modulation signal is in baseband, we usually obtain the signals $\tilde{E}_{in}, \tilde{E}_{ref}$ by splitting the optical power from a single-tone laser source and insert a phase shifter, so that:

$$\tilde{E}_{ref} = k_E\tilde{E}_{in}e^{j(\omega t + \phi_{ref})} \tag{3.2}$$

Compared to the IMDD link that converts the modulated laser power to the photocurrent, the presented coherent link which demodulates the phase modulation usually performs at higher energy efficiency if configured properly [31], and this is one of the reason that this coherent link architecture is chosen. The other reason to utilize it is that $\tilde{E}_{ref}$ does not need to be from the same laser tone as $\tilde{E}_{in}$: suppose there are two laser tones, one with power P_{in} and angular frequency ω_{in}, and the other tone with power P_{ref} and angular frequency ω_{ref}, so the two branches of input signals fulfill the following equations and constraints:

$$\begin{gathered} \tilde{E}_{in} = E_{in}e^{j(\omega_{in}t + \phi_{in})} \\ \tilde{E}_{ref} = E_{ref}e^{j(\omega_{ref}t + \phi_{ref})} \\ E_{in} = \sqrt{P_{in}}, \qquad E_{ref} = \sqrt{P_{ref}}, \qquad \omega_{ref} - \omega_{in} = \omega_{RF} \end{gathered} \tag{3.3}$$

The modulator is modulated by an electrical signal with a carrier frequency of ω_{RF} an a slow-varying amplitude of $v_{amp}(t)$:

$$v_{RF}(t) = v_{amp}(t)cos(\omega_{RF}t + \phi_{RF}) \tag{3.4}$$

From the analysis in the previous section, there will be one or two sidebands generated at the through port of the modulator, plus the residual signals from the original input laser tone:

$$\tilde{E}_{thru} = E_{in}e^{j(\omega_{in}t + \phi_{in})} \cdot \left[\tilde{c}_{residual} + \tilde{c}_{SB+}(t)e^{j(\omega_{RF}t + \phi_{RF})} + \tilde{c}_{SB-}(t)e^{-j(\omega_{RF}t + \phi_{RF})}\right] \tag{3.5}$$

where $\tilde{c}_{SB+}(t) = c_{SB+}(t)e^{j\phi_{SB+}}, \tilde{c}_{SB-}(t) = c_{SB-}(t)e^{j\phi_{SB-}}$ are two slow-varying complex terms that describe the amplitudes and phases of the two sidebands. If the modulation is linear, the magnitudes of $\tilde{c}_{SB+}(t), \tilde{c}_{SB-}(t)$ should be proportional to $v_{amp}(t)$, while the phases of them should be independent of $v_{amp}(t)$ and t [19]. In the spectral domain, $\tilde{E}_{thru}$ contains three frequency elements, and by filtering one of them:

$$\tilde{E}_{thru+} \approx E_{in}e^{j(\omega_{in}t + \phi_{in})} \cdot \tilde{c}_{SB+}(t)e^{j(\omega_{RF}t + \phi_{RF})} \tag{3.6}$$

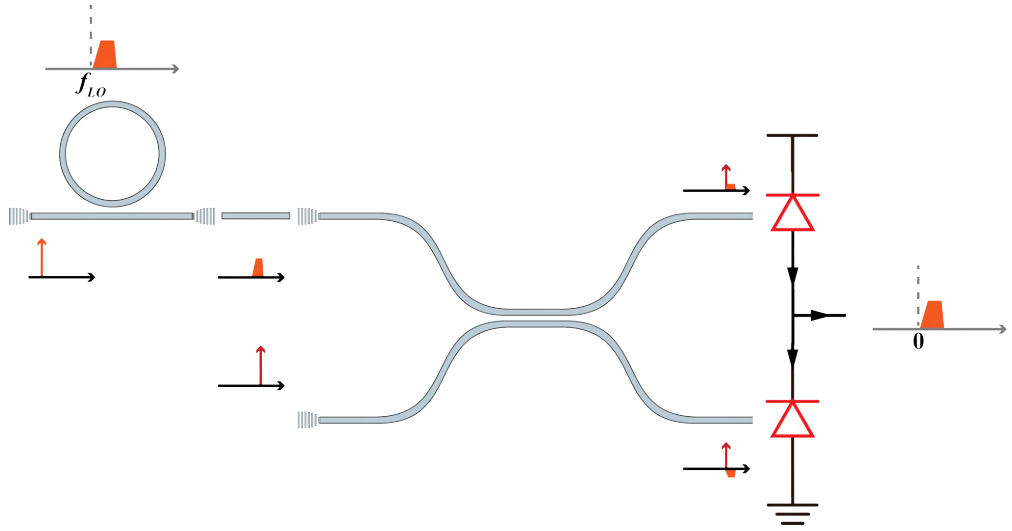

Figure 3.2: Spectral diagram of the proposed link element

and feeding the output into the 2×2 - coupler with $\tilde{E}_{ref}$, based on Eq. 3.1 we have:

$$\begin{aligned} I_{out}(t) =& \mathcal{R}_{PD}(\tilde{E}_{thru}\tilde{E}^*_{ref} + \tilde{E}^*_{thru}\tilde{E}_{ref}) \\ =& \mathcal{R}_{PD}\sqrt{P_{in}P_{ref}}c_{SB}(t)cos\left[(\omega_{RF}+\omega_{in}-\omega_{ref})t + (\phi_{SB+}+\phi_{RF}+\phi_{in}-\phi_{ref})\right] \\ =& \mathcal{R}_{PD}\sqrt{P_{in}P_{ref}}c_{SB+}(t)cos(\phi_{SB+}+\phi_{RF}+\phi_{in}-\phi_{ref}) \end{aligned} \tag{3.7}$$

By defining $\phi_{eq+} = \phi_{SB+} + \phi_{in} - \phi_{ref}$ which is independent from the modulation signal, we have

$$I_{out}(t) = \mathcal{R}_{PD}\sqrt{P_{in}P_{ref}}c_{SB+}(t)cos(\phi_{RF}+\phi_{eq+}) \tag{3.8}$$

The output has only has a slow-varying time-dependent term c_{SB+} because this sideband is close to the reference tone, and Fig. 3.2 presents the spectral diagram showing the core freqeuncy components. If we keep all the sidebands and the residual pump, there will be additional current components, but noticing that the only two frequency components that are close to each other are $\tilde{E}_{thru}$ and $\tilde{E}_{ref}$, all the other remaining time-dependent current components will be fast-varying, for example, $cos(\omega_{RF}t)$ and $cos(2\omega_{RF}t)$. As ω_{RF} is much higher than the bandwidth of the slow-varying terms $c_{SB\pm}(t)$, we can choose to keep $\tilde{E}_{thru}$ without filtering in the optical domain, but instead place a low-pass filter in the electrical frontend to obtain the same output photo current as expressed in Eq. 3.8. In addition, we do not even have those optical signal components that potentially require filtering: if the dual-MRM is implemented, aligning ω_{in} with the left supermode frequency that achieves the maximum c_{SB+} automatically makes c_{SB-} and $c_{residual}$ negligible, and for triple-MRM, we can choose to align ω_{in} with the left-most supermode frequency instead of the central one.

This indicates that the amplitude of the output photo current is proportional to c_{SB+} as we claimed. Once ϕ_{eq+} is set properly so that $|cos(\phi_{RF}+\phi_{eq})| = 1$, we are able to

achieve the maximum output amplitude although this is not necessary in a realistic system implementation, as we can create a replica of the signal, apply $\phi_{eq+,I}, \phi_{eq+,Q}$ with 90 degrees of phase shift to realize the complex demodulation.

The expression of c_{SB} can be derived from Equation 2.20, and given the fact that the 3 dB bandwidth of the dual-MRM based ring is $f_{BW} = 2(r_o + r_e)/2\pi = 2r_o/\pi$, so:

$$\left|\frac{c_{SB}}{v_{amp}}\right| = \frac{1}{8r_o} \cdot \left|\frac{\delta\omega_m}{v_{amp}}\right| = \frac{\pi}{4r_o} \cdot \left|\frac{\partial f_{res}}{\partial V}\right| = \frac{1}{2f_{BW}} \cdot \left|\frac{\partial f_{res}}{\partial V}\right| \tag{3.9}$$

Here the resonance frequency change per unit voltage, $k_{f,V} \equiv \partial f_{res}/\partial V$, is widely used to characterize the performance of the phase shifter. If we dig into the mechanism of $k_{f,V}$, since L representing the circumferences of the two rings don't change during modulation, we have:

$$\begin{aligned} & n(V)L = N \cdot \lambda_{res}(V) = N \cdot \frac{c}{f_{res}(V)} \\ \Rightarrow \quad & L\frac{\partial n}{\partial V} = -\frac{Nc}{f_{res0}^2} \cdot \frac{\partial f_{res}}{\partial V} \\ \Rightarrow \quad & \frac{\partial f_{res}}{\partial V} = -f_{res0} \cdot \frac{\partial n}{\partial V} \end{aligned} \tag{3.10}$$

, where $n(V)$ is the effective refractive index of the resonance cavity modulated by the voltage, N is an integer representing the ratio of the optical path length of the cavity and the resonance wavelength we care about, and λ_{res} is the resonance wavelength. The transconductance equation from the junction voltage shows that the decay rate r_o and the refractive index modulation coefficient $\frac{\partial n}{\partial V}$ of the modulator, which are both material related, are the dominant factors from the ring, while the geometric parameters like the radius does not contribute to the gain much, unless they significantly influence other factors like the bending loss of the ring waveguide:

$$G_{m,j} = \frac{\partial i_{out}}{\partial V_j} = \mathcal{R}_{PD}\sqrt{P_{in}P_{ref}} \cdot \frac{k_{f,V}}{2f_{BW}} \tag{3.11}$$

Equation 3.11 does not consider the energy loss factors of the grating couplers shown in Fig. 3.2 or the parasitic resistance from the electrodes of the modulator to the actual junctions. Coupler loss η_c can be incorporated into the terms P_{in} and P_{ref}. The modulated arm passes through three grating couplers in total, with two at the photonic transmitter and one at the photonic receiver. The reference arm on the other hand, can bypass the photonic transmitter, so equivalently we have:

$$\begin{aligned} P_{in,eq} = \eta_c^3 P_{in}, \qquad & P_{ref} = \eta_c P_{ref} \\ G_{m,j} = \mathcal{R}_{PD}\sqrt{P_{in,eq}P_{ref,eq}} \cdot \frac{k_{f,V}}{2f_{BW}} & = \eta_c^2 \mathcal{R}_{PD}\sqrt{P_{in}P_{ref}} \cdot \frac{k_{f,V}}{2f_{BW}} \end{aligned} \tag{3.12}$$

To verify the accuracy of both the analytic model of the dual-MRM and that of the effective conversion gain model, the Simulink models are established from an open-source

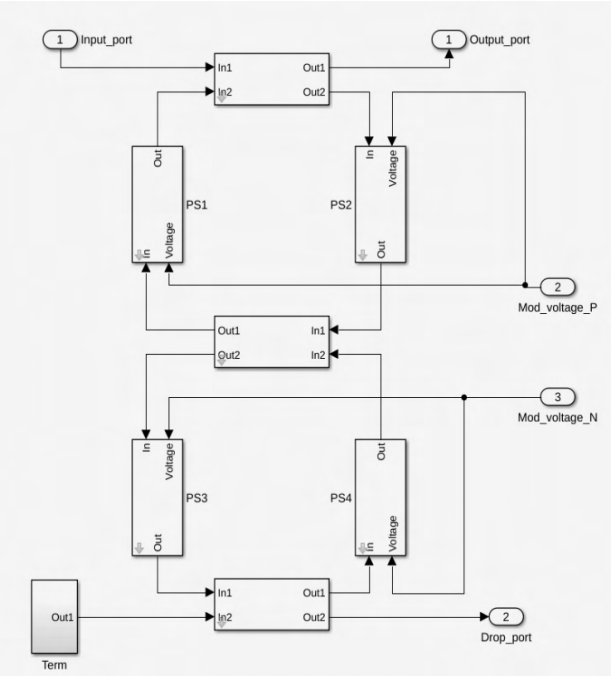

(a) Simulink model of the dual-MRM

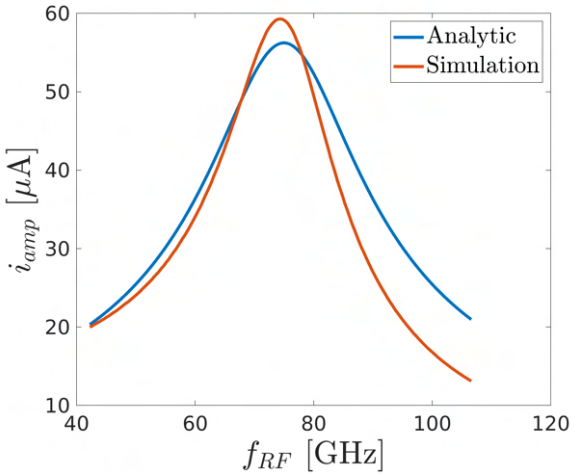

(b) Comparison between analytic solution and simulation

Figure 3.3: Conversion gain characterization of the dual-MRM based link

toolbox [32] to characterize the transient behavior. The model of a dual-MRM is shown in Fig. 3.3. It consists of the waveguide couplers and the phase shifters. The phase shifter takes the material parameters fitting from the device measurement so that the nonlinear effects, including but not limited to the nonlinear voltage to effective index modulation, are also considered. The voltage input represents the junction voltage that can instantly change the effective index of the phase shifter. In the conversion gain simulation, the devices block that represents the link shown in Fig. 3.1, where the modulator is replaced by the dual-MRM model as Fig. 3.3a shows with a resonance split of 75 GHz, the 2×2 - coupler and the balanced photo detectors are both ideal lossless devices with infinite bandwidth. We apply the electrical modulation signals as $v_{\pm}(t) = V_{DC} \pm v_{amp} cos(2\pi f_{RF} t)$ and the optical signals as $\tilde{E}_{ref} = \tilde{E}_{in} = E_{in} e^{j\omega_{opt} t}$. With the specified input signals, the output current will be a fast varying term with a frequency of f_{RF}, while its amplitude will become independent of the ϕ_{eq+}, based on the assumption that there is no residual pump laser component in the through port optical signal:

$$i_{out}(t) = \mathcal{R}_{PD} \sqrt{P_{in} P_{ref}} c_{SB+}(t) \tag{3.13}$$

where $c_{SB+}(t)$ is a time-independent, f_{RF}-dependent term that is proportional to v_{amp}. The comparison of the frequency response of the analytic model and the simulation are plotted in

Fig. 3.3. The results are very similar in terms of the peak gain while showing a discrepancy in the bandwidth and the symmetry of the response. The cause of such discrepancy is the existence of the residual pump laser at angular frequency ω_{opt} at the though port of the MRM. Its amplitude and phase are slightly dependent of the modulation frequency. As a result, the effective pump laser tone propagating out of the 2×2 - coupler has its amplitude varying with f_{RF}, which results in the slightly different output current amplitude.

3.2 Noise

The major portion of the noise originates at the output of the link from the shot noise of the balanced photo detector, with a power spectral density (PSD) of:

$$S_{I,out}(f) = S_{I,shot} = \frac{\overline{i_{shot}^2}}{\Delta f} = 2qI_{DC} \tag{3.14}$$

, where q is the charge of an electron and I_{DC} is the static current flowing through the photodetector. Since there are two photodetectors shown in Fig. 3.1, the noise they generate are uncorrelated, hence we have

$$\begin{aligned} S_{I,shot} &= 2q(I_+ + I-) \\ &= 2q \cdot \mathcal{R}_{PD}(\tilde{E}_+\tilde{E}_+^* + \tilde{E}_-\tilde{E}_-^*) \\ &= 2q \cdot \frac{1}{2}\mathcal{R}_{PD}\left[(\tilde{E}_{thru} + \tilde{E}_{ref})(\tilde{E}_{thru}^* + \tilde{E}_{ref}^*) + (\tilde{E}_{thru} - \tilde{E}_{ref})(\tilde{E}_{thru}^* - \tilde{E}_{ref}^*)\right] \\ &= 2q\mathcal{R}_{PD}(\tilde{E}_{thru}\tilde{E}_{thru}^* + \tilde{E}_{ref}^*\tilde{E}_{ref}) \\ &= 2q\mathcal{R}_{PD}(P_{thru} + P_{ref}) \end{aligned} \tag{3.15}$$

The sideband power is usually much lower than the reference power, which is one of the reasons to use the coherent link, so $P_{thru} + P_{ref} \approx P_{ref}$. Finally, if we take the coupler loss into account, we have:

$$\begin{aligned} S_{I,shot} &= 2q\mathcal{R}_{PD}(P_{thru,eq} + P_{ref,eq}) \\ &\approx 2q\mathcal{R}_{PD}P_{ref,eq} \\ &= 2q\eta_c\mathcal{R}_{PD}P_{ref} \end{aligned} \tag{3.16}$$

The gain and noise model of such a link is very similar to a MOSFET common-source amplifier: it has the series RC network $R_j - C_j$ at the input junction resulting in the physical noise source and loss at high frequencies, can be characterized by the transconductance gain, and have the noise current at the output. Therefore, the noise figure of the link has the similar expression:

$$\begin{aligned} F &= 1 + \frac{R_j}{R_S} + \frac{S_{I,shot}}{4kTR_S} \cdot \frac{1}{|A_{V,j}G_{m,j}|^2} \\ A_{V,j} &= \frac{1}{1 + j\omega(R_S + R_j)C_j} \end{aligned} \tag{3.17}$$

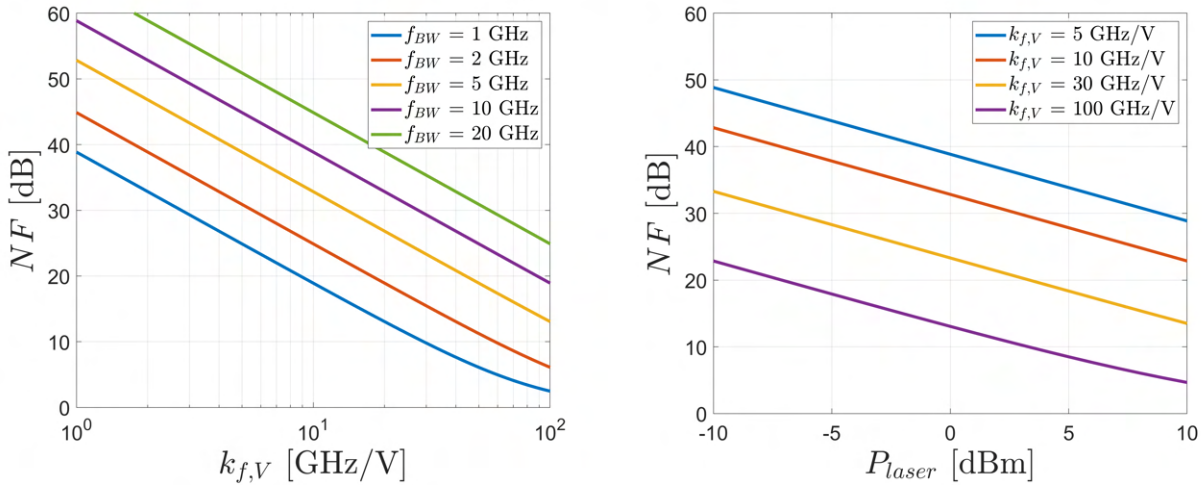

(a) NF v.s. resonance sensitivity. $P_{laser} = 0\,\text{dBm}$

(b) NF v.s. total laser power. $f_{BW} = 5\,\text{GHz}$

Figure 3.4: Scaling of NF with resonance frequency sensitivity $k_{f,V}$ and total laser power P_{laser}. Assumptions: $P_{ref} = P_{in} = P_{laser}/2$, η_c = -2 dB, $\mathcal{R}_{PD} = 1\,\text{A/W}$ and $Q_j = 2$.

By substituting $S_{I,shot}$ by the expression in Eq. 3.16 and $G_{m,j}$ by that in Eq. 3.12, we have:

$$\begin{aligned} F &= 1 + \frac{R_j}{R_S} + \frac{S_{I,shot}}{4kTR_S} \cdot \frac{1}{|A_{V,j}G_{m,j}|^2} \\ &= 1 + \frac{R_j}{R_S} + \frac{2q\eta_c\mathcal{R}_{PD}P_{ref}}{4kTR_S} \cdot \frac{4f_{BW}^2\left[1+\omega^2(R_S+R_j)^2C_j^2\right]}{\eta_c^4\mathcal{R}_{PD}^2P_{in}P_{ref}k_{f,V}^2} \\ &= 1 + \frac{R_j}{R_S} + \left[1+\omega^2(R_S+R_j)^2C_j^2\right]\frac{q}{kTR_S} \cdot \frac{1}{\eta_c^3\mathcal{R}_{PD}P_{in}} \cdot \frac{f_{BW}^2}{k_{f,V}^2} \end{aligned} \tag{3.18}$$

In case $R_j \ll R_S$, $\omega(R_S + R_j)C_j \approx \omega R_j C_j = 1/Q_j$, where Q_j is the frequency-dependent electrical quality factor of the junction network, so:

$$F \approx 1 + \frac{q}{kTR_S} \cdot \left(1 + Q_j^{-2}\right) \cdot \frac{1}{\eta_c^3\mathcal{R}_{PD}P_{in}} \cdot \frac{f_{BW}^2}{k_{f,V}^2} \tag{3.19}$$

From Eq. 3.19, there are several factors that potentially improve the noise figure. For example, a high junction quality factor reduces the signal loss while the limitation exists as it is a passive network; the responsivity of the photodetector, the coupler loss together with the modulation branch laser power represents the non-MRM portion of the photonic link. What draws most of our interests are however, f_{BW} and $k_{f,V}$, since they both lead to steeper decrease of the large term in the noise figure expression. With advanced phase shifters, we are able to reach lower decay rate and higher resonance sensitivity to voltage.

The decay rate can be lowered until the optical channel bandwidth is limited by the system level bandwidth specifications. The resonance sensitivity on the other hand, is not limited by any system level specs, which potentially brings even more improvement. Fig. 3.4a and Fig. 3.4b illustrate the trend of decreasing noise figure with higher laser power and with the improvement of the cavity decay rate, and the resonance frequency sensitivity. The existing process is able to provide modulators with around 35 - 45 dB noise figure with about 1 mW total laser power. To achieve a reasonably low overall noise figure comparable to that of the electrical link, the LNA is still required to pre-amplify the RF /mm-wave signals at present. If we are targeting around 3 dB degradation of SNR by the modulator-PD link, the power gain spec of the LNA is approximately the NF calculated above. With the improving performance of the modulator, we are foreseeing lower LNA gain specification which reduces both the electrical power consumption and the area.

3.3 Linearity

For the microring modulator, if we define the sideband conversion efficiency (SCE) in amplitude as c_{SB}, which is the squareroot of G_{SB} defined in Eq. 2.19, we will see in the next section that the gain from the input voltage to the output photo current is proportional to the gain from the input voltage to c_{SB}. There are two major factors that add the non-linearity to this gain, which are the voltage-to-$\delta\omega_m$ modulation, and the $\delta\omega_m$-to-c_{SB} conversion, respectively.

The $\delta\omega_m$-to-c_{SB} conversion, is the product of a linear term and a non-linear term:

$$\begin{aligned} c_{SB} &= \sqrt{G_{SB}^{basic,optimized}} \\ &= \frac{\delta\omega_m}{8r_o}\left[1+\left(\frac{\Delta\omega_s^2+\Delta\omega_a^2}{4r_o^2}+\frac{\Delta\omega_s^2\Delta\omega_a^2}{16r_o^4}\right)+\left(\frac{1}{32}-\frac{\Delta\omega_s\Delta\omega_a}{128r_o^2}\right)\left(\frac{\delta\omega_m}{r_o}\right)^2+\frac{1}{4096}\left(\frac{\delta\omega_m}{r_o}\right)^4\right]^{-\frac{1}{2}} \end{aligned} \tag{3.20}$$

The following normalization can be done to simplify the equation:

$$t_s \equiv \frac{\Delta\omega_s}{r_o}, \qquad t_a \equiv \frac{\Delta\omega_a}{r_o}, \qquad t_m \equiv \frac{\delta\omega_m}{r_o} \tag{3.21}$$

, so that c_{SB} can be decomposed into the product of three terms:

$$\begin{aligned} c_{SB} &= \frac{t_m}{8}\left[1+\frac{t_s^2+t_a^2}{4}+\frac{t_s^2t_a^2}{16}+\left(\frac{1}{32}-\frac{t_st_a}{128}\right)t_m^2+\frac{1}{4096}t_m^4\right]^{-\frac{1}{2}} \\ &= \frac{t_m}{8}\left(1+\frac{t_s^2+t_a^2}{4}+\frac{t_s^2t_a^2}{16}\right)^{-\frac{1}{2}}\left[1+\frac{\left(\frac{1}{32}-\frac{t_st_a}{128}\right)t_m^2+\frac{1}{4096}t_m^4}{1+\frac{t_s^2+t_a^2}{4}+\frac{t_s^2t_a^2}{16}}\right]^{-\frac{1}{2}} \\ &\equiv c_{lin,max}\cdot c_{deg}\cdot c_{harmonics} \end{aligned} \tag{3.22}$$

Here $c_{lin,max}$ represents the the maximum linear SCE naturally at zero detuning, c_{deg} is the degradation of the SCE due to detuning, and $c_{harmonics}$ can be used for distortion

analysis:

$$c_{lin,max} = \frac{t_m}{8} \tag{3.23}$$

$$c_{deg} = \left(1 + \frac{t_s^2 + t_a^2}{4} + \frac{t_s^2 t_a^2}{16}\right)^{-\frac{1}{2}} \tag{3.24}$$

$$c_{harmonics} = \left\{1 + c_{deg}^2 \left[\left(\frac{1}{32} - \frac{t_s t_a}{128}\right) t_m^2 + \frac{1}{4096} t_m^4\right]\right\}^{-\frac{1}{2}} \tag{3.25}$$

Eq. 3.25 can be approximately written in the form of the following Taylor series:

$$(1+x)^{-\frac{1}{2}} = 1 - \frac{1}{2}x + \frac{3}{8}x^2 + O(x^3) \tag{3.26}$$

$$\begin{aligned} c_{hormonics} &\approx 1 - \frac{1}{2} c_{deg}^2 \left[\left(\frac{1}{32} - \frac{t_s t_a}{128}\right) t_m^2 + \frac{1}{4096} t_m^4\right] + \frac{3}{8} c_{deg}^4 \left(\frac{1}{32} - \frac{t_s t_a}{128}\right)^2 t_m^4 \\ &= 1 - 2^{-8} \times c_{deg}^2 \left(4 - t_s t_a\right) t_m^2 + 2^{-16} \times \left[\frac{3}{2}(4 - t_s t_a)^2 - 8 c_{deg}^{-2}\right] c_{deg}^4 t_m^4 \\ &\equiv a_0 + a_2 t_m^2 + a_4 t_m^4 \end{aligned} \tag{3.27}$$

From the Taylor series, the input (defined as t_m) interception point of the third-order and the fifth-order harmonics can be calculated:

$$IIP_3^{t_m} = \sqrt{\left|\frac{4a_0}{3a_2}\right|} = \frac{32}{\sqrt{3}} \times \frac{c_{deg}^{-1}}{\sqrt{|4 - t_s t_a|}} \tag{3.28}$$

$$IIP_5^{t_m} = \sqrt[4]{\left|\frac{58a_0}{25a_4}\right|} = 16\sqrt[4]{\frac{58}{25}} \times \frac{c_{deg}^{-1}}{\sqrt[4]{\left|t_s t_a - \sqrt{2}(t_s + t_a) - 4\right| \left|t_s t_a + \sqrt{2}(t_s + t_a) - 4\right|}} \tag{3.29}$$

The plots of $c_{deg}, IIP_3^{t_m}$ and $IIP_5^{t_m}$ versus the frequency detuning are shown in Fig. 3.5. The plots indicate that the linearity of the intrinsic dual-ring modulation mechanism is high with proper detuning, with less than 6 dB gain degradation. A fine control of the detuning help to achieve an normalized IIP_3 of nearly 55 dB as the red regions in Fig. 3.5b, which is 35dB higher. Even if we don't have fine control over the detunings, we can see a much larger detuning space represented by the green regions, where the IIP_3 is around 35 dB, bringing an improvement of 15 dB.

3.4 Linearity Verification and Measurement

Although single-MRM is not practical to be implemented in the proposed system, its performance metrics are easier to verify, so the same time domain CMT model for the dual- or

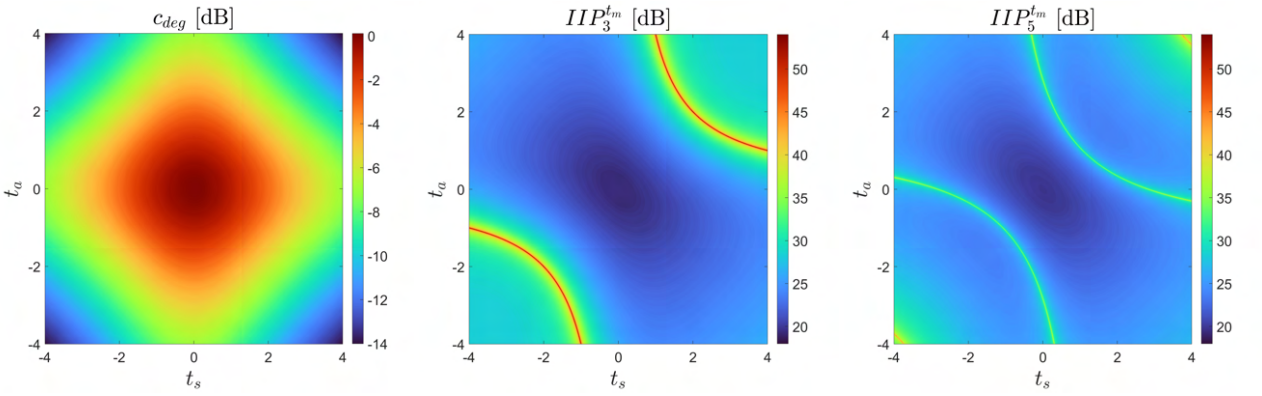

(a) Degradation from detuning (b) Normalized IIP_3 (c) Normalized IIP_5

Figure 3.5: Degradation and linearity of the sideband conversion efficiency c_{SB}

triple-MRM can be applied to it as well and through measurement, the accuracy level of the model can be verified indirectly.

Based on the time-domain CMT, the wave inside the cavity $\tilde{s}_{cav}$ which is proportional to $\tilde{E}_{cav}$ should fulfill:

$$\begin{aligned}\frac{\partial}{\partial t}\tilde{s}_{cav} &= j[\omega_0 + \delta\omega(t) + j(r_o + r_e)]\tilde{s}_{cav} - j\sqrt{2r_e}\tilde{E}_{in} \\ &= j[\omega_0 + \delta\omega(t) + j(r_o + r_e)]\tilde{s}_{cav} - j\sqrt{2r_e}E_{in}e^{j(\omega_0+\Delta\omega)t}\end{aligned} \tag{3.30}$$

The resonance frequency of the single-MRM is modulated to change in the form of: $\delta\omega(t) = \frac{\delta\omega_m}{2}cos(\omega_{RF}t)$, so we know that the two sidebands will be generated and there will be residual laser pump signal, so the through optical signal in the cavity can be written in the form of:

$$\tilde{s}_{cav} \equiv E_{in}\left[\tilde{c}_- e^{j(\omega_0+\Delta\omega-\omega_{RF})t} + \tilde{c}_0 e^{j(\omega_0+\Delta\omega)t} + \tilde{c}_+ e^{j(\omega_0+\Delta\omega+\omega_{RF})t}\right] \tag{3.31}$$

By substituting $\tilde{E}_{cav}$ with the expression form Eq. 3.31, the left and the right part of Eq. 3.30 are:

$$\begin{aligned}&\frac{\partial}{\partial t}\tilde{s}_{cav} = jE_{in}\begin{bmatrix} e^{j(\omega_0+\Delta\omega-\omega_{RF})t} \\ e^{j(\omega_0+\Delta\omega)t} \\ e^{j(\omega_0+\Delta\omega+\omega_{RF})t}\end{bmatrix}^T \begin{bmatrix}(\omega_0+\Delta\omega-\omega_{RF})\tilde{c}_- \\ (\omega_0+\Delta\omega)\tilde{c}_0 \\ (\omega_0+\Delta\omega+\omega_{RF})\tilde{c}_+\end{bmatrix} \\ &j[\omega_0 + \delta\omega(t) + j(r_o + r_e)]\tilde{s}_{cav} - j\sqrt{2r_e}E_{in}e^{j(\omega_0+\Delta\omega)t} \\ &= jE_{in}\begin{bmatrix} e^{j(\omega_0+\Delta\omega-\omega_{RF})t} \\ e^{j(\omega_0+\Delta\omega)t} \\ e^{j(\omega_0+\Delta\omega+\omega_{RF})t}\end{bmatrix}^T \begin{bmatrix}(\omega_0+jr_o+jr_e)c_- + \frac{\delta\omega_m}{4}\tilde{c}_0 \\ (\omega_0+jr_o+jr_e)c_0 + \frac{\delta\omega_m}{4}(\tilde{c}_- + \tilde{c}_+) - \sqrt{2r_e} \\ (\omega_0+jr_o+jr_e)\tilde{c}_+ + \frac{\delta\omega_m}{4}\tilde{c}_0\end{bmatrix}\end{aligned} \tag{3.32}$$

Notice the the three time-dependent terms are mutually orthogonal, so the matrices on the right of the equations are the same, i.e.:

$$\begin{bmatrix}(\omega_0+\Delta\omega-\omega_{RF})\tilde{c}_-\\(\omega_0+\Delta\omega)\tilde{c}_0\\(\omega_0+\Delta\omega+\omega_{RF})\tilde{c}_+\end{bmatrix}=\begin{bmatrix}(\omega_0+jr_o+jr_e)\tilde{c}_-+\frac{\delta\omega_m}{4}\tilde{c}_0\\(\omega_0+jr_o+jr_e)\tilde{c}_0+\frac{\delta\omega_m}{4}(\tilde{c}_-+\tilde{c}_+)-\sqrt{2r_e}\\(\omega_0+jr_o+jr_e)\tilde{c}_++\frac{\delta\omega_m}{4}\tilde{c}_0\end{bmatrix}$$
$$\Rightarrow\begin{bmatrix}\Delta\omega-j(r_o+r_e)-\omega_{RF} & -\frac{1}{4}\delta\omega_m & 0\\-\frac{1}{4}\delta\omega_m & \Delta\omega-j(r_o+r_e) & -\frac{1}{4}\delta\omega_m\\0 & -\frac{1}{4}\delta\omega_m & \Delta\omega-j(r_o+r_e)+\omega_{RF}\end{bmatrix}\begin{bmatrix}c_-\\c_0\\c_+\end{bmatrix}=\begin{bmatrix}0\\-\sqrt{2r_e}\\0\end{bmatrix} \tag{3.33}$$

The solution set of the coefficients is:

$$\begin{aligned}\tilde{c}_0&=\frac{-\sqrt{2r_e}}{\Delta\omega-j(r_o+r_e)}\cdot\frac{1}{1-\frac{1}{8}\frac{\delta\omega_m^2}{[\Delta\omega-j(r_o+r_e)]^2-\omega_{RF}^2}}\\\tilde{c}_\pm&=\frac{\delta\omega_m}{4[\Delta\omega-j(r_o+r_e)\pm\omega_{RF}]}\tilde{c}_0\\&=\frac{\delta\omega_m\sqrt{2r_e}}{4[\Delta\omega-j(r_o+r_e)][\Delta\omega-j(r_o+r_e)\pm\omega_{RF}]}\cdot\frac{1}{1-\frac{1}{8}\frac{\delta\omega_m^2}{[\Delta\omega-j(r_o+r_e)]^2-\omega_{RF}^2}}\end{aligned} \tag{3.34}$$

and the sideband conversion efficiencies at the through port can be derived given $\tilde{E}_{thru}=E_{in}-j\sqrt{2r_e}\tilde{E}_{cav}$:

$$\begin{aligned}&c_{SB\pm}=|-j\sqrt{2r_e}c_\pm|\\&=\left|\frac{\delta\omega_m r_e}{2[\Delta\omega-j(r_o+r_e)][\Delta\omega-j(r_o+r_e)\pm\omega_{RF}]}\right|\cdot\left|\frac{1}{1-\frac{1}{8}\frac{\delta\omega_m^2}{[\Delta\omega-j(r_o+r_e)]^2-\omega_{RF}^2}}\right|\end{aligned} \tag{3.35}$$

, where the first fraction is linear to the modulation $\delta\omega_m$ and the second term represents the nonlinear term: $|c_{SB\pm}|\equiv c_{lin\pm}\cdot c_{harmonics\pm}$, at low frequencies we have:

$$\begin{aligned}c_{harmonics\pm}|_{\omega_{RF}\to0}&=\left|\frac{1}{1-\frac{1}{8}\frac{\delta\omega_m^2}{[\Delta\omega-j(r_o+r_e)]^2}}\right|=\left|\frac{1}{1-\frac{1}{8}\frac{\delta\omega_m^2}{\Delta\omega^2-(r_o+r_e)^2-2j\Delta\omega(r_o+r_e)}}\right|\\&=\frac{1}{\sqrt{\left[1-\frac{1}{8}\frac{\delta\omega_m^2}{\Delta\omega^2-(r_o+r_e)^2-2j\Delta\omega(r_o+r_e)}\right]\left[1-\frac{1}{8}\frac{\delta\omega_m^2}{\Delta\omega^2-(r_o+r_e)^2+2j\Delta\omega(r_o+r_e)}\right]}}\\&=\frac{1}{\sqrt{1-\frac{\Delta\omega^2-(r_o+r_e)^2}{4[\Delta\omega^2+(r_o+r_e)^2]^2}\delta\omega^2+\frac{1}{64[\Delta\omega^2+(r_o+r_e)^2]^2}\delta\omega^4}}\end{aligned} \tag{3.36}$$

Here we can still assume that $r_e=r_o$ and do the similar normalization as Eq. 3.21: $t_D=\Delta\omega/r_o, t_m=\delta\omega_m/r_o$ which represent the normalized detuning and the normalized modula-

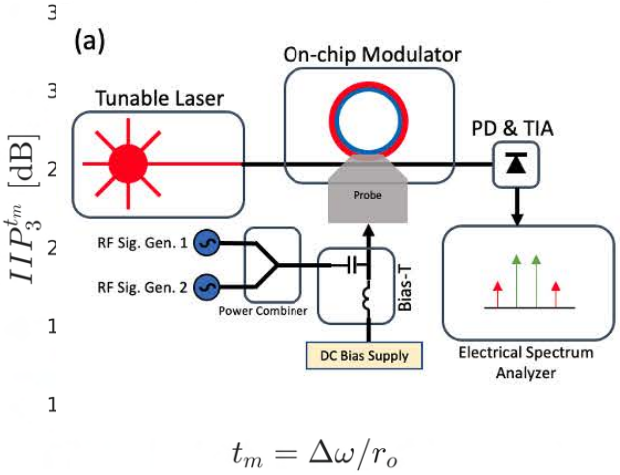

$$t_m = \Delta\omega / r_o$$

(a) Single-MRM IIP_3 from time-domain CMT

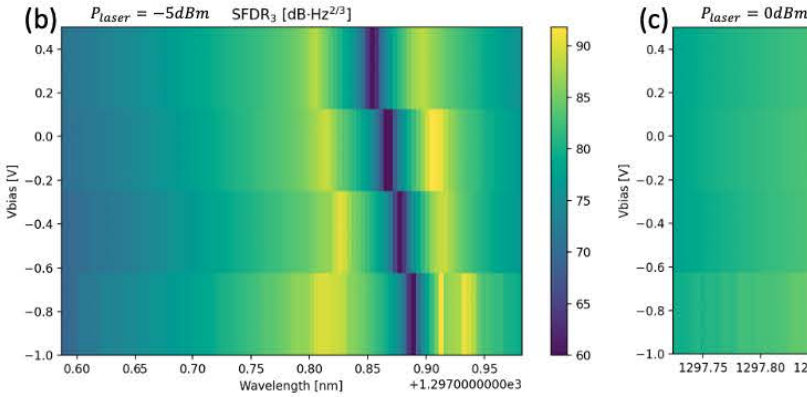

(b) Measured $SFDR_3$ [33]

Figure 3.6: Degradation and linearity of the sideband conversion efficiency c_{SB}

tion, respectively. By simplifying Eq. 3.36 with the normalization we get:

$$c_{harmonics\pm}\big|_{\omega_{RF}\to 0} = \frac{1}{\sqrt{1 - \frac{t_D^2-4}{4(t_D^2+4)^2}t_m^2 + \frac{1}{64(t_D^2+4)^2}t_m^4}} \tag{3.37}$$

, and by applying the Taylor expansion in Eq. 3.26, we have:

$$IIP_3^{t_m} = 4\sqrt{\frac{2}{3}} \times \frac{t_D^2+4}{\sqrt{|t_D+2||t_D-2|}} \tag{3.38}$$

$$IIP_5^{t_m} = 2\sqrt[4]{\frac{232}{25}} \times \frac{t_D^2+4}{\sqrt[4]{\left|t_D^2-(\sqrt{6}-\sqrt{2})^2\right|\left|t_D^2-(\sqrt{6}+\sqrt{2})^2\right|}} \tag{3.39}$$

Using the same method based on the time-domain CMT, we can achieve the normalized IIP_3 for the IMDD link as well. The analysis results are shown in Fig. 3.6a, where we can observe that IIP_3 reaches its local minimum when there is no detuning, and similar to the analysis of the dual-MRM with results shown in Fig. 3.5b, we can achieve a local peaking IIP_3 when the normalized detuning is ± 2 which gives us a significant benefit in term of linearity with the cost of the conversion efficiency. Such linearity enhancement is verified by the measurement [33] plotted in Fig. 3.6b. The measured third-order spurious-free dynamic range ($SFDR_3$) is highly correlated to IIP_3. The figure shows that the dark regions happens to overlap the single-MRM's resonance wavelengths, which fits the analytic model. It also has light regions representing the enhanced $SFDR_3$ on the left and right of the resonance that accords with the model, and after extracting the intrinsic decay rate r_o of this ring cavity

through the full-width half-max of the Lorentzian shape, the optimal detuning matches what the analytic models describes as well. These results confirm that even if the phase shifter being modulated in the cavity has a non-linear relationship to the bias voltage, we can still achieve this linearity enhancement originated from the intrinsic characteristic of the MRM.

3.5 Dynamic Range

In most cases, the third-order harmonic/intermodulation is the dominant distortion source. The Spurious-free dynamic range ($SFDR$) of it, defined as the input range from the minimum detectable signal (MDS) to the level that the harmonic is detectable, is then used to indicate whether the design can operate accommodating a wide range of input power level. the photonic device can be derived from the following equation:

$$SFDR_3 = \frac{2}{3}(IIP_3^{dB} - MDS^{dB}) \tag{3.40}$$

For the proposed link, the MDS of the output current gives us 0 dB SNR, and the MDS of the input voltage term $\delta\omega_m$ can be achieved by dividing it by the conversion gain related term. Further more, we can normalize it to r_o so that the result can be computed with the IIP_3 normalized to r_o:

$$MDS_{out} = 2S_{I,shot} \tag{3.41}$$

$$\begin{aligned} MDS_{in} =& MDS_{out} \cdot \left(\frac{1}{G_{m,j}c_{deg}} \cdot \frac{\delta\omega_m}{v_{amp}} \cdot \frac{1}{r_o}\right)^2 \\ =& 2S_{I,shot} \cdot \frac{4f_{BW}^2}{\eta_c^4 \mathcal{R}_{PD}^2 P_{in} P_{ref} k_{f,V}^2 c_{deg}^2} \cdot \frac{16k_{f,V}^2 r_o^2}{f_{BW}^2} \cdot \frac{1}{r_o^2} \\ =& 4q\eta_c \mathcal{R}_{PD} P_{ref} \cdot \frac{64}{\eta_c^4 c_{deg}^2 \mathcal{R}_{PD}^2 P_{in} P_{ref}} \\ =& \frac{256q}{\eta_c^3 c_{deg}^2 \mathcal{R}_{PD} P_{in}} \end{aligned} \tag{3.42}$$

The equation together with the plot of IIP_3 normalized to r_o implies that the third-order SFDR is independent of parameters like $k_{f,V}$, but instead highly dependent of the detuning terms t_s, t_a and the effective laser power. Fig. 3.7 presents the calculated $SFDR_3$ in two scenarios with a total laser power of -10 dBm and 0 dBm, respectively. As a reference, the SFDR with zero detuning is about 88 dB·Hz$^{2/3}$ and 98 dB·Hz$^{2/3}$. These two values means that with 1 Hz of noise bandwidth, the link can achieve 88 dB and 98 dB dynamic range, so considering an extreme case with 10 GHz signal (and noise) bandwidth, we need to deduct $\frac{2}{3} \times 10log_{10}(10^{10}) \approx 67$ dB from them, which gives us the dynamic range of 21 dB and 31 dB, respectively. Although a perfect detuning to the maximum value is challenging, from the plots we are still able to target 100 dB·Hz$^{2/3}$ and 110 dB·Hz$^{2/3}$ respectively with some detuning tolerance, which further boosts the dynamic range by about 12 dB.

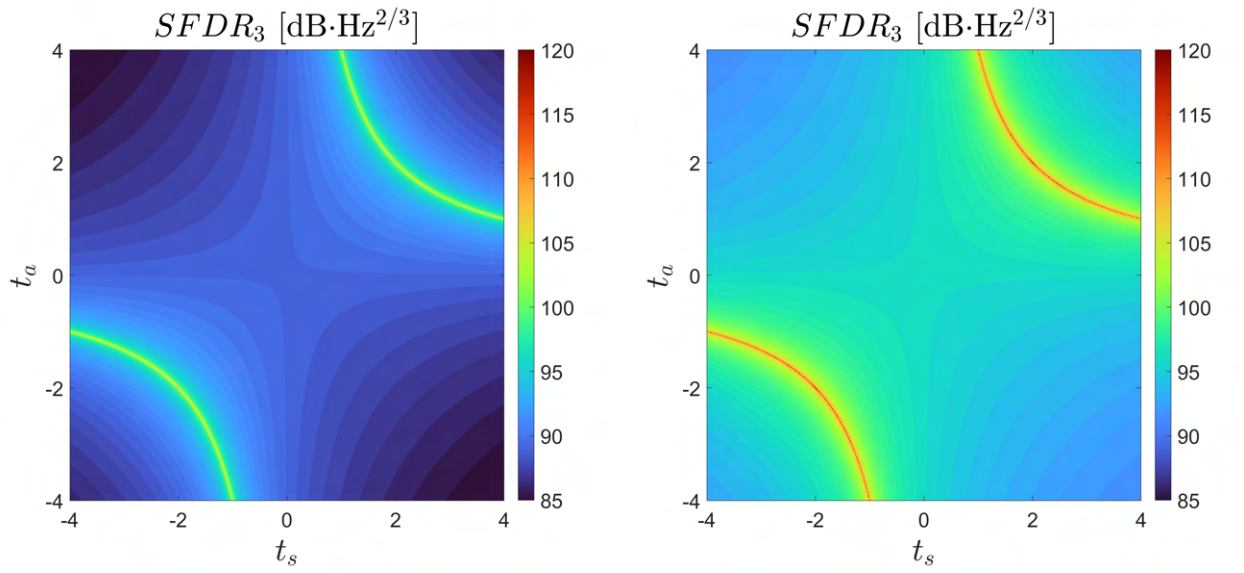

(a) Total laser power = -10 dBm

(b) Total laser power = 0 dBm

Figure 3.7: $SFDR_3$ of the dual-MRM. $\mathcal{R}_{PD}$ = 1.0 A/W, η_c = -2.0 dB

3.6 Chapter Summary

This chapter analyzes the fundamentals of the proposed photonic link. By employing two optical laser tones that can be treated as the photonic pump and LO, respectively, and by modulating the pump with RF/millimeter-wave signal and mixing with the LO at the receiver, the demodulated photo current at the output will be the baseband current. The end-to-end photonic link can be modeled as a down-conversion mixer with parameters of effective conversion gain/transconductance, noise figure and IIP_3 like regular electronic circuits and blocks. The gain and noise performance metrics are both correlated with the resonance frequency shift strength $k_{f,V}$ and the intrinsic decay rate r_o of the ring resonator. A higher $k_{f,V}$ also decreases both the upper bound and the lower bound of the input signal to be detectable without spurs, while the range between the two bounds are still kept the same.

Chapter 4

Transmitter Array Element Design in An RFSOI Platform

This chapter illustrates the design of the transmitter array element targeting 70 GHz carrier frequency in a CMOS RFSOI process. In order to achieve the gain and NF comparable to purely electrical links, an LNA needs to be implemented between the antenna and the microring modulator. To drive the dual-MRM or triple-MRM in the push-pull configuration, the LNA needs to have differential outputs. For the MRM performance available in this process, the gain of the LNA needs to be in the range of 30 - 40 dB. With SWaP-C considerations, the area of a transmitter element design, which is dominated by the passive inductive devices, need to be minimized. The RFSOI design platform does need some post processing to enable operational photonic devices, and specific design considerations for both the LNA and the photonics, which will be analyzed throughout this chapter.

4.1 Substrate Release and Circuits Design

The design is implemented in a commercial CMOS RFSOI process [34] that enables "zero change" electronic-photonic monolithic integration [35–40]. As shown in Fig. 4.1, the buried oxide (BOX) layer insulates the active device and the thick substrate, and the silicon above the insulation can be used for the design of waveguides, grating couplers, or other passive and active photonic devices in addition to the regular transistors, since its refractive index is significantly higher than the surroundings which is important the confine the optical mode. The "zero change" means no additional precise doping or change of the front-end-of-line (FEOL) or back-end-of-line (BEOL) layers. However, this SOI process was not originally intended for silicon photonics monolithic integration, so the silicon dioxide insulation is not thick enough to reject the leakage of the optical mode from the optical devices and waveguides to the thick silicon substrate with similar refractive index, and this results in unacceptable optical loss. To resolve the optical loss issue, one essential post-processing is to fully etch out the silicon substrate, which is called substrate removal or substrate release.

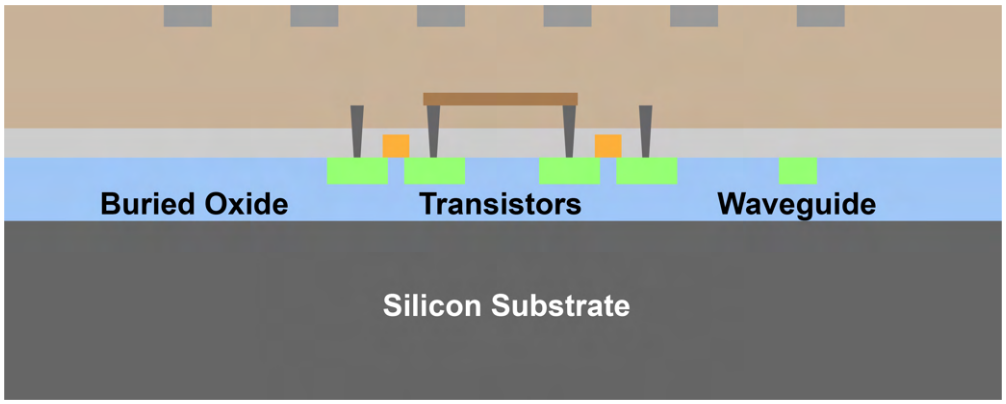

Figure 4.1: Cross-section of Zero-change monolithic on an SOI process platform

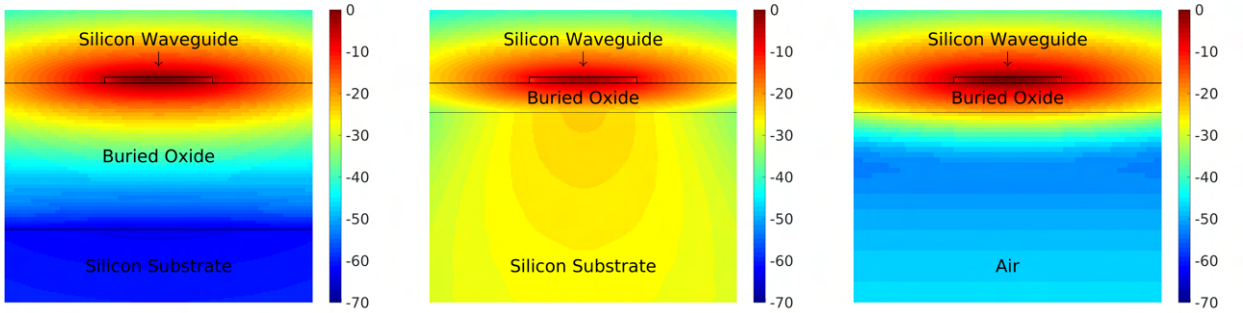

(a) Thick BOX layer

(b) Thin BOX layer

(c) Thin BOX layer with substrate release

Figure 4.2: Example of the normalized propagating optical power density [dB] around the waveguide cross section with different BOX thickness and post processing

Fig. 4.2 shows the representative optical mode distribution around the waveguide section along its propagation with different material stack and post-processing configurations, and it reveals the necessity of the substrate release for SOI processes with a thin BOX layer in terms of electronic-photonic monolithic integration. The following sections will show how the substrate release process, together with other constraints, affects the design space of the transmitter array element.

4.2 Active Core

As the gain specification of the LNA is high, there will be multiple gain stages connected by passive interstage matching networks in between to resonate the capacitive impedance maximize the power gain, so the area of the passives such as inductors and transformers

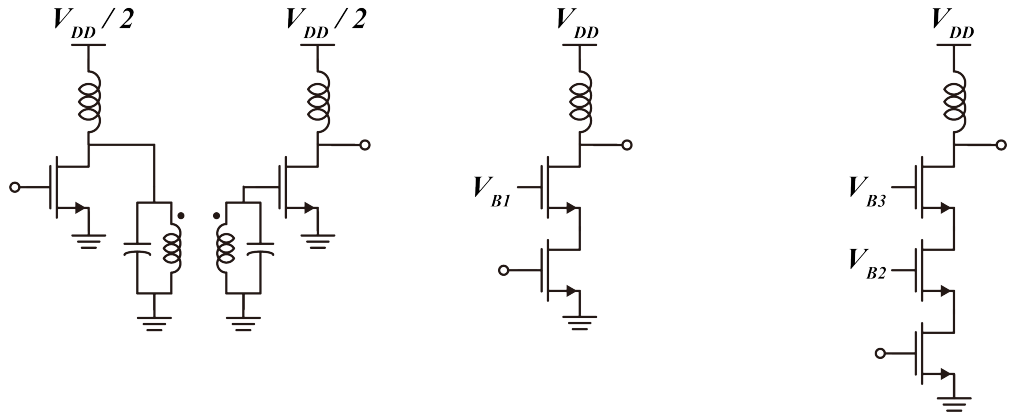

Figure 4.3: Three topologies for gain and noise comparison. Left: benchmark 2 CS stages w/ 1 interstage transformer; middle: 1 CS with 1 CG stage stacked; right: 1 CS with 2 CG stages stacked

(XFs) will dominate that of the entire photonic link transmitter design. Compared to the benchmark topology shown on the left of Fig. 4.3, which is a cascade of two common-source (CS) amplifier stages with interstage impedance matching, if we can find out an alternative topology of a similar gain without any inductive passives that occupy additional area, then this new active stage topology can replace the benchmark one, as the area can be significantly reduced.

Here two alternative topologies are shown together in Fig. 4.3: the middle diagram represents a 2-stack topology with one CS stack and one common-gate (CG) stack, and the right diagram shows a 3-stack topology with one CS stack and two CG stacks. To make a fair comparison, the two alternative topologies have the same supply voltage, which is twice of the supply voltage of the benchmark. Together with the setup that makes the current flowing through all the transistors the same, the total static power consumption of the three topologies are the same. The individual transistor has the double-gated layout with pitch and routing optimized [41–45] for smaller parasitic parameters and higher post-extraction gain.

All these three topologies for comparison can be treated as a two-port network that a 2×2 network matrix can represent. For example, the relationship between the voltages and currents of at the two ports, $i_{1,2}$ and $v_{1,2}$, can be described by the Y-parameter:

$$\begin{bmatrix} i_i \\ i_2 \end{bmatrix} = \begin{bmatrix} y_{11} & y_{12} \\ y_{21} & y_{22} \end{bmatrix} \begin{bmatrix} v_1 \\ v_2 \end{bmatrix}, \qquad Y \equiv \begin{bmatrix} y_{11} & y_{12} \\ y_{21} & y_{22} \end{bmatrix} \tag{4.1}$$

In this design, the target is to maximize the transducer gain, which is defined as the ratio of the power delivered to the load to the power available from the source, and which depends on both the source and the load impedance :

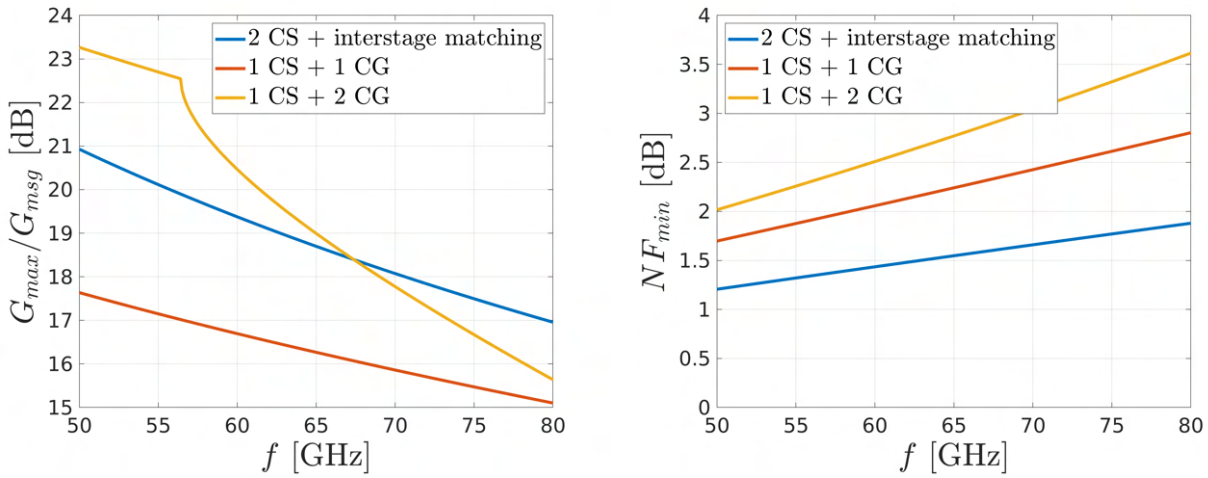

(a) Maximum available gain or maximum stable gain

(b) Minimum noise figure

Figure 4.4: Comparison of different topologies in gain and noise figure

$$G_T(Z_S, Z_L) = \frac{P_L}{P_{av,S}} \tag{4.2}$$

If the two port network is unconditionally stable, which physically means it never oscillates regardless of the passive load and source impedance, and mathematically means a stability parameter K is larger then 1:

$$K = \frac{2\Re(y_{11})\Re(y_{22}) - \Re(y_{12}y_{21})}{|y_{12}y_{21}|} \tag{4.3}$$

, then the maximum available gain can be achieved with a lossless bi-conjugate match:

$$G_{max} = G_T(Z_{S,match}, Z_{L,match}) = \frac{y_{21}}{y_{12}}(K - \sqrt{K^2 - 1}) \tag{4.4}$$

If the two port is conditionally stable, which means K is less than 1 and the circuit might be unstable with specific combinations of source/load impedance, then a bi-conjugate matching makes the network oscillate, hence either a lossy source/load or an impedance mismatch is desired to avoid potential oscillation, and in this case the maximum stable gain will be used instead:

$$G_{msg} = \frac{y_{21}}{y_{12}} \tag{4.5}$$

Fig. 4.4a shows the merged curves of $min(G_{max}, G_{msg})$ depending on the value of K. From the plot we can see that with the same static power, the maximum gain of the 2-stack

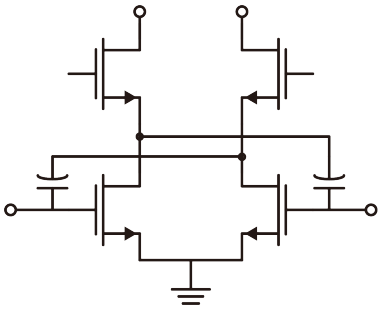

Figure 4.5: Example of the neutralization capacitors in a differential pair

topology (1 CS + 1 CG) is about 2 - 3 dB lower than that of the benchmark. This loss term is due to the fact that the CS stage does not have power matching with the CG stage. However, this drawback is acceptable in this design, as the alternative topology gets rid of one matching network, which is very likely to include either an inductor of a transformer that occupies an additional chip area. The plot also shows that the 3-stack topology (1 CS + 2 CG) benefits from even higher gain compared to the 2-stack design. However, its stronger roll-off indicates that the design might confront challenge in case a design with wider bandwidth is desired. Furthermore, too many stacks also makes the design potentially prone to DC biases and process variation, especially in this case where the supply voltage is low.

The minimum noise figure plots are shown in Fig. 4.4b, Here the blue line NF_{min} of the benchmark assumes a very ideal case, where the power matching between two CS stages simultaneously fulfills a noise matching. In most cases this is not naturally fulfilled so that the realistic NF_{min} will be higher than the plotted curve. Nevertheless, the the 2-stack topology only endures a penalty of around 0.5 - 1.0 dB, which is fairly reasonable. As a result, this design will choose the 2-stack (1 CS + 1 CG) topology as one active stage, and implement interstage power matching in between.

For the common-source stage, the physical C_{gd} will bring up the following effects which potentially deteriorates the performance of the design:

- Any disturbance at the drain node can be coupled to the gate through C_{gd} passively, and the coupled disturbance will be amplified by the common-source topology, which causes potential stability issues.

- The voltage gain of a general common-source topology is negative, and this makes the equivalent capacitance seeing from the gate to the drain higher than the physical C_{gd}. Larger capacitor of the same quality factor indicates higher conductance in parallel, and this leads to higher loss in the paralleled inductor-capacitor resonance tank.

- As the resonance frequency of an inductor-capacitor tank is $\omega_0 = \frac{1}{LC}$, a smaller inductance is preferred, and this might challenge its physical design process.

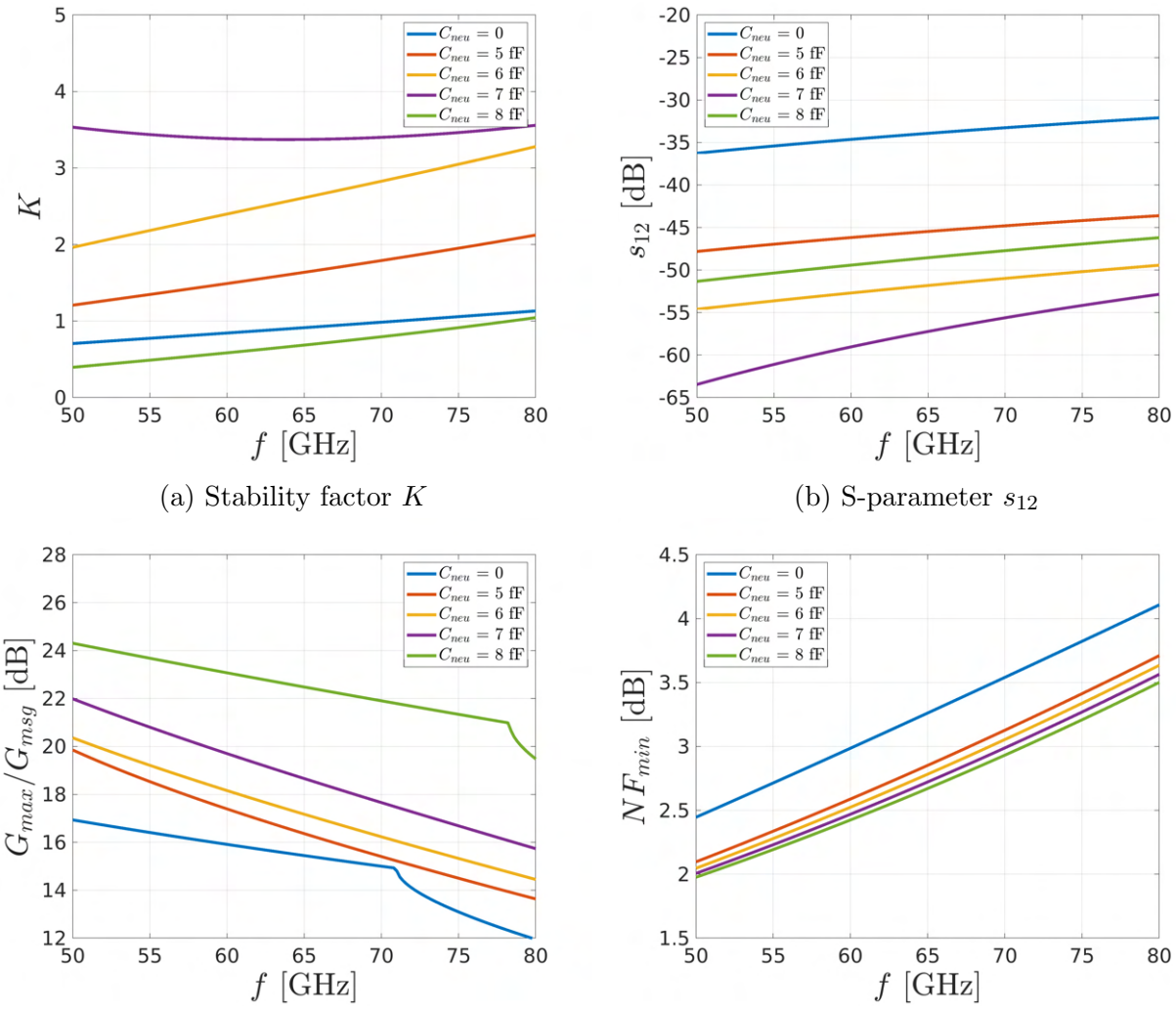

(a) Stability factor K

(b) S-parameter s_{12}

(c) Maximum available / stable gain

(d) Minimum noise figure

Figure 4.6: Simulated performance metrics versus frequency with varied neutralization capacitance C_{neu}

For the differential active core, the neutralization capacitors [46–48] that are shown in Fig. 4.5 are introduced for the differential pair to resolve the potential design issues. By matching the neutralization capacitance to the physical gate-drain capacitance: $C_{neu} = C_{gd}$, for any one of the gates in the common-source topology, the differential signals at the drains couples to it with the same strength in opposite directions, so ideally it is a unilateral network for the differential signal. Plots in Fig. 4.6 shows the simulation results of the important performance metrics of the differential active stage, including the stability factor K, the S-parameter s_{12} that propagates backwards, the maximum available / stable gain and the minimum noise figure NF_{min}, with different neutralization capacitance values.

From the plots we can summarize that:

- Without implementing the neutralization capacitors, K might be lower than 1, so the active stage is not always unconditionally stable across the frequency range of interest.
- A proper neutralization capacitance significantly decreases s_{12} that represents the wave traveling backwards, which is also a signal of higher stability factor K.
- Eq. 4.4 seems to imply that a higher stability factor K results in a lower G_{max} at first glance. In this case however, the neutralization capacitors simultaneously improves the maximum available gain and the stability This is because the Y-parameters also change with C_{neu}. In addition, the minimum noise figure also benefits from the neutralization. As the neutralization capacitance continues increasing, i.e. the network gets over-neutralized, many performance metrics degrades while the maximum gain can still increase.

To finally determine the precise neutralization capacitance, these performance metrics are also simulated versus C_{neu} at different frequency points, which are plotted in Fig. 4.7. From the plot we can observe that in the frequency range of our interest, the stability factor K peaks when C_{neu} is around 6.5 fF, and the maximum gain peaks when C_{neu} is in between 7.5 fF and 8 fF. However, Fig. 4.7a also shows a steeper slope when C_{neu} is larger than 6.5 fF, which potentially prevents the active stage being unconditionally stable. Considering potential process variation of all the on-chip devices, C_{neu} is fixed between 6 fF - 6.5 fF in this design.

In terms of the common-mode signals, however, it is equivalent to adding additional capacitor to C_{gd} that makes it more vulnerable to common-mode disturbance.

4.3 Passive Inter-stage Transformer

In this design, transformers are selected as the key passive impedance matching component in between the active stages, as it can be potentially more compact. A transformer consists of two mutually coupled inductors (named the primary and the secondary coil), which can be characterized by the self-inductance L_p, L_s, their quality factor Q_p, Q_s, and the mutual inductance M determined by the coupling coefficient k:

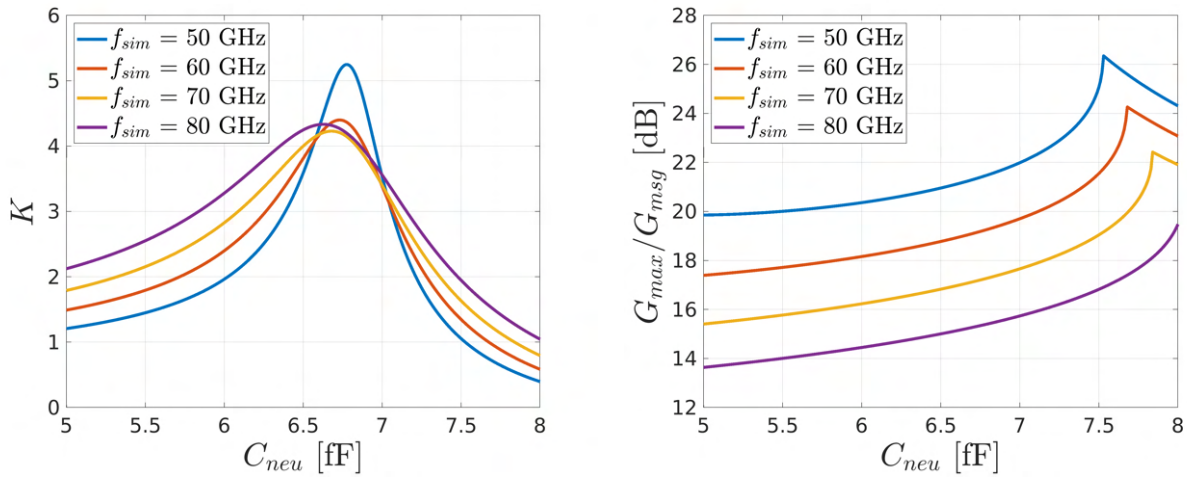

(a) Stability factor K (b) Maximum available / stable gain

Figure 4.7: Simulated performance metrics versus C_{neu} at different frequency points

$$M = k\sqrt{L_p L_s}, \qquad 0 < |k| < 1 \tag{4.6}$$

With such a transformer, it achieves the best transducer gain if the source impedance Z_S on the primary side and the load impedance Z_L on the secondary side fulfill:

$$\begin{aligned} Z_{S,XF,opt} &= \frac{\sqrt{k^2 Q_p Q_s + 1}}{Q_p}\omega L_p - j\omega L_p \\ Z_{L,XF,opt} &= \frac{\sqrt{k^2 Q_p Q_s + 1}}{Q_s}\omega L_s - j\omega L_s \end{aligned} \tag{4.7}$$

where ω is the operating angular frequency. In the meantime, the Y parameter of the active stage directs to the following requirement to maximize its own transducer gain:

$$\begin{aligned} Y_{S,active,opt} &= \frac{y_{12}y_{21} - 2\Re(y_{11})\Re(y_{22}) + |y_{12}y_{21}|(K + \sqrt{K^2 - 1})}{2\Re(y_{22})} - j\Im(y_{11}) \\ Y_{L,active,opt} &= \frac{y_{12}y_{21} - 2\Re(y_{11})\Re(y_{22}) + |y_{12}y_{21}|(K + \sqrt{K^2 - 1})}{2\Re(y_{11})} - j\Im(y_{22}) \end{aligned} \tag{4.8}$$

This is to say if a bi-conjugate power match is realized, we need to have:

$$\begin{aligned} Z^*_{S,active,opt} &= \frac{1}{Y^*_{S,active,opt}} = Z_{L,XF,opt} \\ Z^*_{L,active,opt} &= \frac{1}{Y^*_{L,active,opt}} = Z_{S,XF,opt} \end{aligned} \tag{4.9}$$

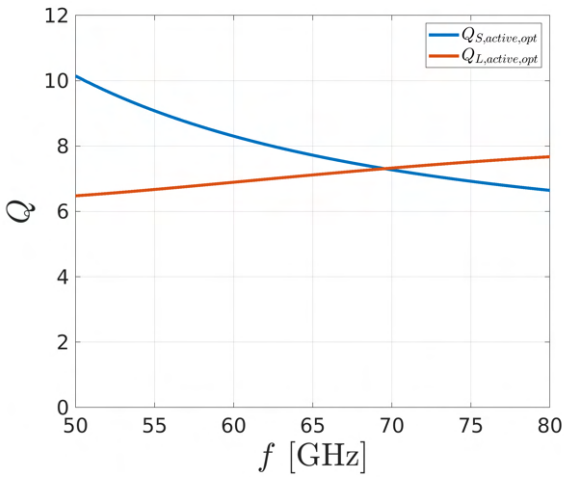

Figure 4.8: Quality factors of the optimal source and load impedance for the active stage

which is not automatically fulfilled. To be more specific, the necessary conditions for the bi-conjugate match match between the active stage and the transformer contain:

$$\begin{aligned} Q_{S,active,opt} &= Q_{L,XF,opt} \\ Q_{L,active,opt} &= Q_{S,XF,opt} \end{aligned} \tag{4.10}$$

where $Q = |\Im(Z)/\Re(Z)|$. Fig 4.8 shows $Q_{S,opt}$ and $Q_{L,opt}$ of the active stage computed from the simulated network parameters, which are in the range of 6 to 10. One the other hand, these quality factors of the transformer can be derived from Eq. 4.7, and can be simplified with the assumption $Q_p = Q_s = Q_{ind}$:

$$Q_{XF,opt} = \left|\frac{\Im(Z_{XF,opt})}{\Re(Z_{XF,opt})}\right| = \frac{Q_{ind}}{\sqrt{k^2 Q_{ind}^2 + 1}} \tag{4.11}$$

The equation is approximately:

$$Q_{XF,opt}|_{k^2Q_{ind}^2 \gg 1} = \frac{Q_{ind}}{\sqrt{k^2 Q_{ind}^2 + 1}} \approx \frac{1}{|k|} \ll Q_{ind} \tag{4.12}$$

in case $k^2 Q_{ind}^2 \gg 1$, while with this assumption the bi-conjugate match is not likely to happen since Q_{ind} in the transformer are between 10 and 15 in this design, which will be shown in the later sections, and which is only slightly higher than $Q_{S,active,opt}, Q_{L,active,opt}$ that need to match $Q_{XF,opt}$. On the other hand, we would like to avoid the case where $k^2 Q_{ind}^2 \not\gg 1$, because the G_{max} of the transformer itself will degrade, which is even regardless of the matching between the active stage and itself.

Fig 4.9 shows the plots of $Z_{S,active,opt}$ and $Z_{L,active,opt}$ with the lower halves of two equal-Q curves corresponding to $k = 0.2$ (representing a weakly coupled transformer) and $k = 0.5$

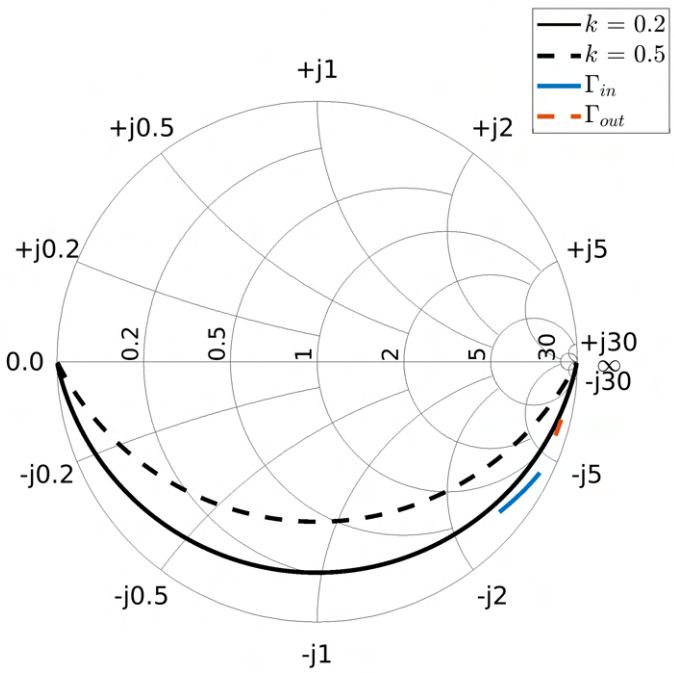

Figure 4.9: Smith chart of the active stage with $Q_{ind} = 15$. Γ_{in}: reflection seen from a 50 Ohm source to the input impedance $Z^*_{S,active,opt}$ assuming the output is matched; Γ_{out}: reflection seen from a 50 Ohm load to the output impedance $Z^*_{L,active,opt}$ assuming the input is matched.

(representing a strongly coupled transformer). The full equal-Q curves should be symmetric along the horizontal axis, and regions inside a full equal-Q curve represent the impedance with lower Q. The plot reveals that even with a fairly week coupling coefficient $k = 0.2$, the Q-match is still not fulfilled, yet this k already results in a G_{max} of -3 dB assuming that $Q_{ind} = 15$. Therefore, in order to fulfill the bi-conjugate match, additional components are required to avoid low k that leads to low G_{max} of the inductor.

The fact that both Γ_{in} and Γ_{out} are below the equal-Q curves also implies for the component used to match the network Q, no matter whether they placed in series or in parallel, they must contain inductive components, which potentially occupies a large area. Fig. 4.10 shows two matching topologies we are exploring. The left one assumes that both the primary and the secondary side of the transformer can be matched by placing additional inductors in series. The right one assumes that a capacitor is placed in parallel with the output of the active stage, and this will be explored later though it seems to contradict the principle of matching the network Q.

Fig. 4.11 shows the electrical parameters of the inductors. The additional inductors in series are assumed lossless (i.e. their component Q is infinite) and the inductors in the

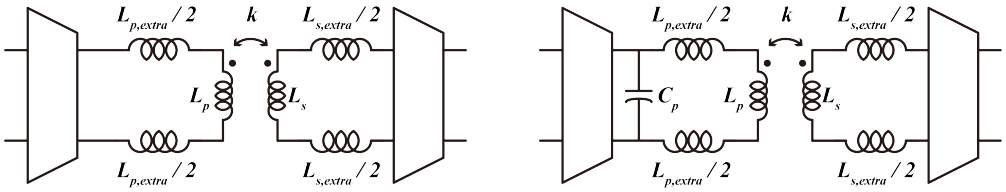

Figure 4.10: Two interstage matching topologies for preliminary evaluation

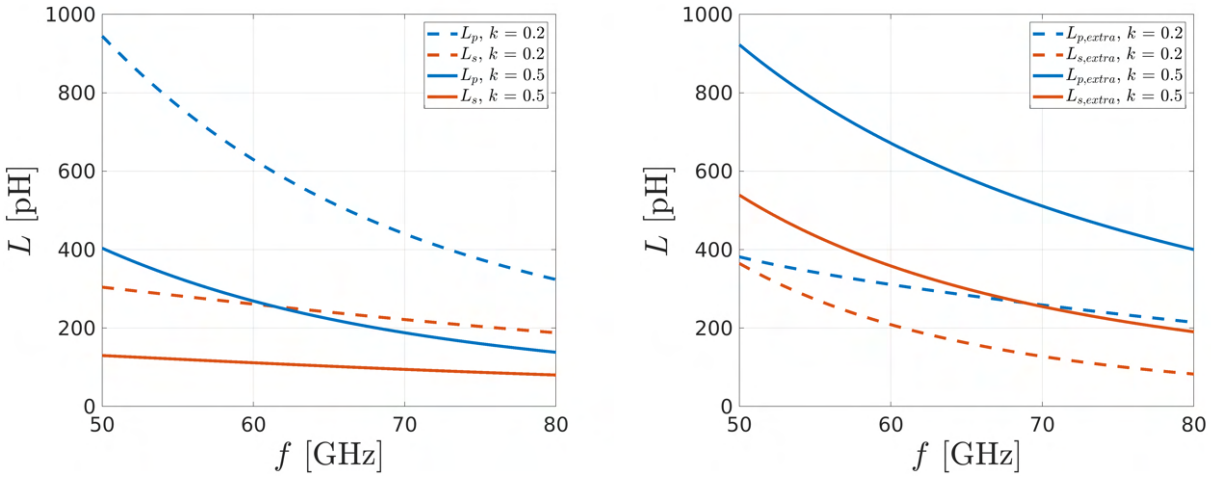

(a) Required self inductance of the transformer (b) Required additional inductance in series

Figure 4.11: Inductance needed for the interstage matching without shunt capacitor

transformer has a Q of 15. There are a few observations from the plots:

- Fig. 4.11a shows the self inductance of the primary and the secondary coil of the transformer. A strong coupling significantly decreases the required inductance, which is an advantage as large on-chip inductors, especially those close to 1 nH, are not likely to have high quality factor at mm-wave frequency band.
- No matter whether the coupling is assumed as strong or not, there is a considerable difference between the primary and secondary coils' inductance. This makes the strong coupling infeasible as there are only 2 - 3 thick layers of metal to route the coils. Usually there will be more design flexibility if this inductance ratio can be close to 1.
- The additional series inductance is close to those of the primary and secondary coil, applying more area constraint for the system design.

As a result, bi-conjugate matching with only inductors seems not practical due to the high inductance and the ratio between the two coils of the transformer. If these two bottlenecks

can be properly handled, the overall design might be much easier. This results in the motivation of analyzing the topology with shunt capacitance in the right of Fig. 4.10 and .

The ratio between the coils can be derived from Eq. 4.7 and Eq. 4.9:

$$\frac{\Re(Z_{L,active,opt})}{\Re(Z_{S,active,opt})} = \frac{\Re(Z_{S,XF,opt})}{\Re(Z_{L,XF,opt})} = \frac{L_p Q_s}{L_s Q_p} \approx \frac{L_p}{L_s} \tag{4.13}$$

Fig. 4.11a reveals that decreasing the real part of $Z_{L,active,opt}$, i.e. the resistance, helps to realize a $1:1$ ratio. If we derive the resistance from the expression of the admittance:

$$\Re(Z) = \Re\left(\frac{1}{Y}\right) = \Re\left(\frac{1}{G+jB}\right) = \Re\left(\frac{G-jB}{G^2+B^2}\right) = \frac{G}{G^2+B^2} \tag{4.14}$$

here G represents the conductance and B is the susceptance. Adding a shunt capacitor does not influence G while it makes B higher. As a result, in case the original B is larger than 0, which is the case in this design, the additional shunt capacitor effectively reduces the resistance. If we only place one capacitor C_p to match the resistance for a $1:1$ transformer, Fig. 4.12a shows the required C_p that is independent from the coupling coefficient k together with the inductance of the $1:1$ transformer that is dependent of k, and Fig 4.12b presents the additional series inductance for a bi-conjugate match. The plots together with the plots with no shunt capacitor reveal the following design intuition:

- The comparison between Fig. 4.11a and Fig. 4.12a shows that the shunt capacitor not only triggers a $1:1$ transformer, but also reduces the inductance of the two coils, no matter whether the coupling of the coils is strong or weak.
- If we only target a smaller inductance, strong coupling is preferred over weak coupling.
- The required additional series inductance decreases to a limited extent, so shunt capacitance is not likely to fully resolve the area-matching trade-off here.

Despite the remaining power mismatch, reducing the required transformer inductance and allowing a $1:1$ ratio is already a big advantage. Notice that the right diagram in Fig. 4.10 only assumes one capacitor on the primary coil side, and practically we can also place additional capacitor C_s on the secondary coil side. By tuning C_p and C_s with two degrees of freedom, we can keep a transformer ratio close to $1:1$ and simultaneously reduce the inductance. Notice that the series inductance required becomes even higher than that of the transformer inductance after adding the shunt capacitor(s), in this design we decided not to implement the additional inductors, which sacrifices the power gain in order to make the design more compact.

As mentioned in the previous section, the silicon substrate of the chip needs to be removed after flip-chip packaging the chip, in order to preserve the optical mode inside the silicon waveguide, which changes the electromagnetic (EM) environment of the transformer. The substrate release process is illustrated in Fig. 4.13, where the chip is flip-chip packaged and

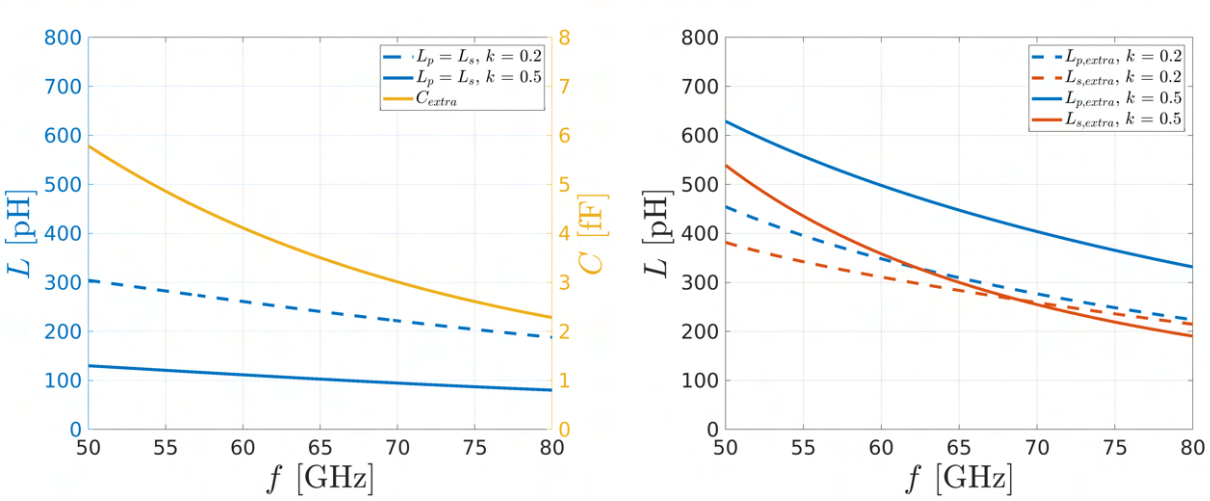

(a) Required self inductance and of the transformer and shunt capacitance

(b) Required additional inductance in series

Figure 4.12: Inductance needed for the interstage matching with one shunt capacitor

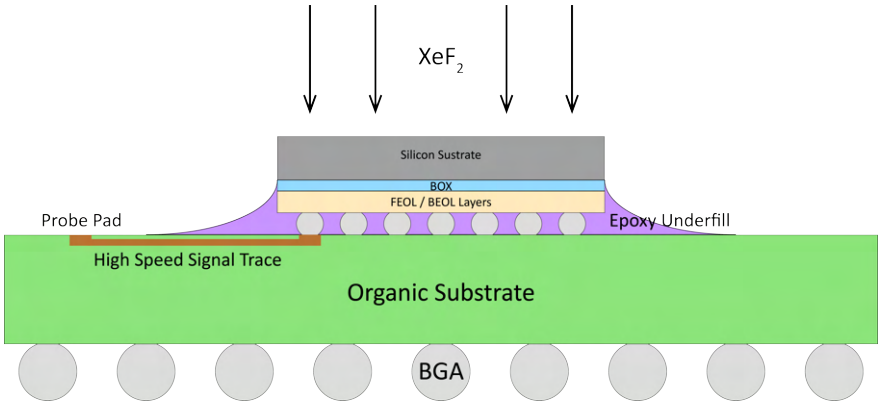

Figure 4.13: The substrate release process. XeF_2 etches out the silicon substrate

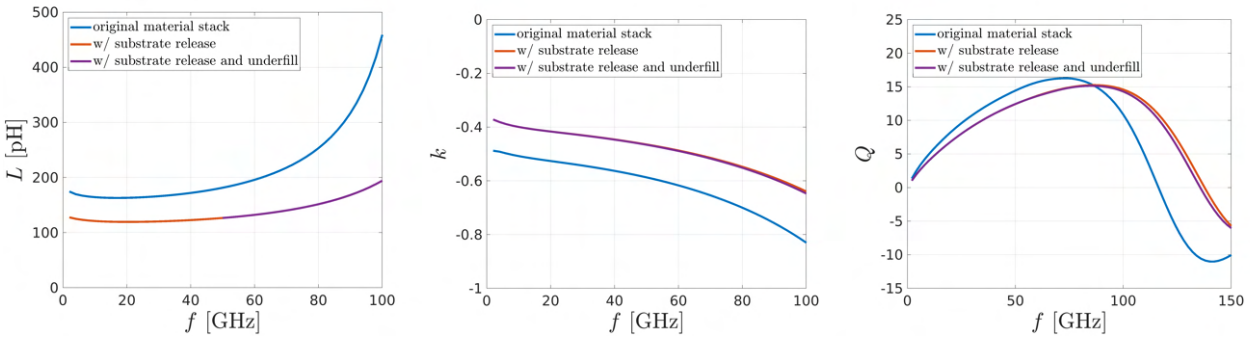

(a) Inductance (b) Coupling factor (c) Quality factor

Figure 4.14: Influence on the electromagnetic simulation results from the packaging process

has its thick silicon substrate etched by Xenon difluoride (XeF_2). Compared to the wirebond process, the main difference in the EM environment are the substrate and the epoxy underfill. Fig. 4.14 shows part of the core characteristics of the interstage transformer in this design that are extracted from the EM simulation that models these changes. The results include the inductance and the quality factor of the primary coil (close to the secondary one the results of which are not shown) together with the coupling factor k between the two coils. The results reveal that:

- The substrate release process significantly changes the EM environment as the silicon substrate is lossy. On the contrary, the underfill material for the flip-chip package only conduct minor effects.
- The effective inductance of the coils decrease by about 30% after the substrate release, and k implies a weaker mutual coupling between the coils. These two factors necessitate the need of placing shunt capacitors in order to realize a compact and area efficient design.
- The quality factor also seems lower below 90 GHz. One reason is that the inductance decreases. However, the decrease of Q in this frequency range is less significant compared to the inductance L because removing the lossy substrate effectively helps to preserve the electromagnetic energy, and this effect also results in a higher self-resonance frequency (SRF) of the coils where Q reaches 0, as shown in Fig. 4.14c.

4.4 Input and Output Matching Networks and LNA Implementation

The cascade of the active stages and inter-stage transformers builds up the LNA core. In a practical system, its input is integrated with a 50 Ω antenna, and its output is driving the

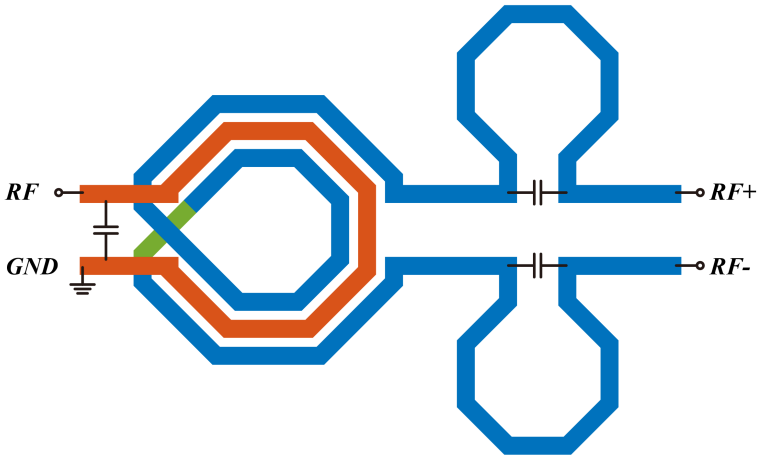

Figure 4.15: Layout diagram of the input matching inductors and transformers

MRM. Compared to a single-ended LNA that matches both the input and output impedance to 50 Ω, this design differs in terms of:

- A balun is required for the input matching network to convert the single-ended signals from the antenna to the differential signals applied to the differential core of the LNA.
- The output is no longer a 50 Ω load, but instead the load impedance of the MRM, which the output matching network need to accommodate.
- The load impedance is no longer a real number, and the performance metric to optimize is the voltage amplitude at the junction of the MRM.

The layout of the input matching network core is shown in Fig. 4.15, where the single-ended signal passes through a transformer with an approximate ratio of 1 : 2, followed by a series inductor pair to cancel out the remaining reactance. A capacitor pair is placed in parallel with the series inductor pair, so that they can provide a higher differential series reactance without requiring larger footprint for the inductors. There is also a capacitor implemented close to the input GSG probe pad utilizing metal-to-metal parasitic capacitance as a part of the input matching network.

For the output matching network, our goal is to maximize the voltage amplitude applied to the junction capacitor of the MRM. A practical MRM load impedance can be represented as the parasitic resistance R_s in series with this junction capacitance C_j, in this case we have:

$$\begin{aligned} \frac{|v_{amp,C_j}|^2}{|v_{amp,R_s}|^2} &= \frac{|Z_{C_j}|^2}{|Z_{R_s}|^2} = \frac{|Z_{C_j}|^2}{\omega^2 C_j^2 R_s^2} \\ \rightarrow |v_{amp,C_j}|^2 &= \frac{|v_{amp,R_s}|^2}{\omega^2 R_s^2 C_j^2} = \frac{P_{R_s}}{\omega^2 R_s C_j^2} \end{aligned} \tag{4.15}$$

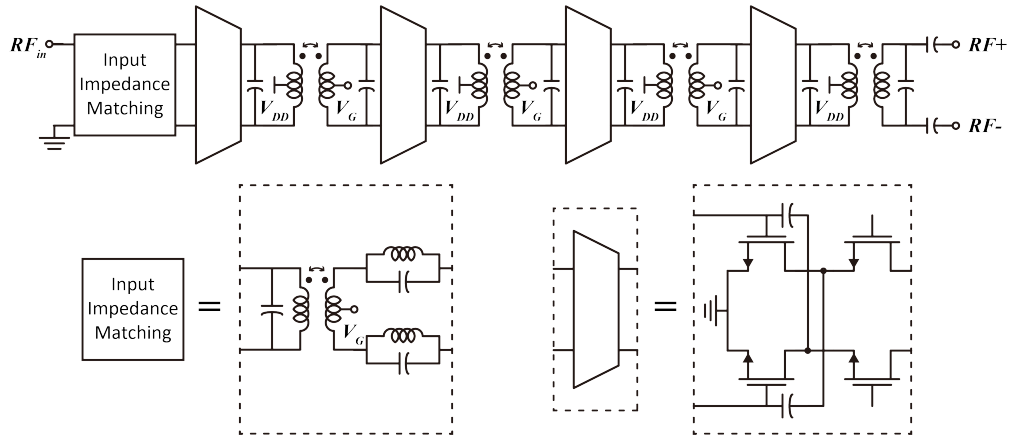

Figure 4.16: Schematic of the LNA

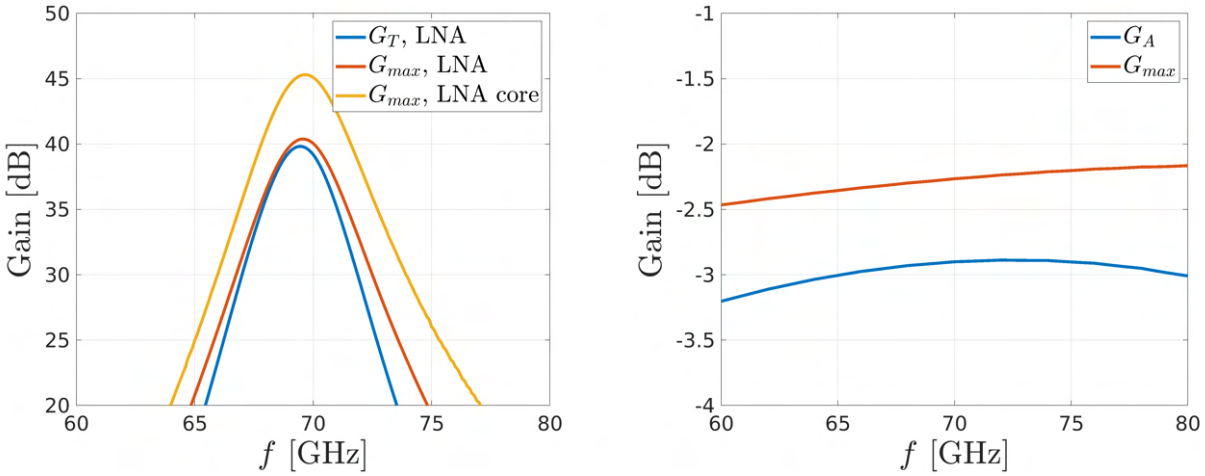

(a) Transducer gain G_T and maximum available gain G_{Amax} of the LNA and the LNA core

(b) Available gain G_A and maximum available gain G_{max} of the input matching network

Figure 4.17: Gain of the LNA building blocks

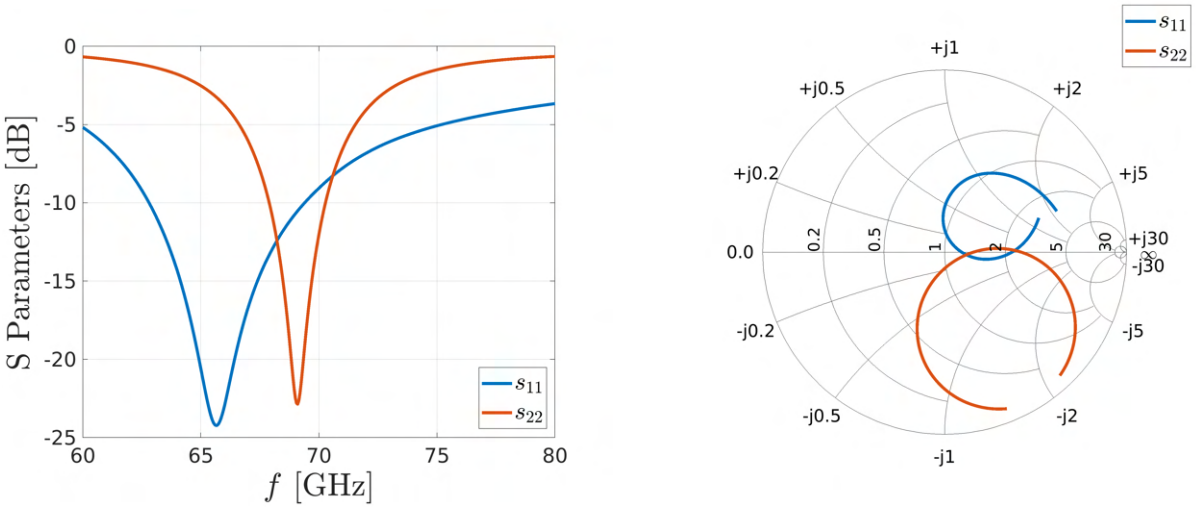

(a) Rectangular plot

(b) Smith chart

Figure 4.18: s_{11} and s_{22} of the LNA

, where ω is the operating frequency and P_{R_s} is the power delivered to R_s. Since all the other parameters are fixed, the goal is equivalently maximizing the $P_{R,s}$, so the output matching procedure is to match the output of the LNA to R_s with a mandatory C_j in series with R_s. The transformer closely connected to the output of the last active stage will be considered a part of the LNA core, so the matching network will be the residual inductors or capacitors. In this design, an L-match that consists of capacitors happens to be good for the modeled R_s and C_j of the MRMs.

The schematic of the LNA that contains all the essential matching network components is shown in Fig. 4.16. It consists of four active stages with interstage matching, plus the input power and noise matching at the input and the output matching to the modulator load impedance. Its performance is evaluated through the gain, noise and linearity simulations. Fig. 4.17a shows the plots of the maximum available gain G_{max} and the transducer gain G_T. The peak G_{max} of the LNA core is around 45.3 dB, while that of the entire LNA with input and output matching decreases to 40.3 dB, and the gain degradation is mainly due to the passive input matching network. Fig. 4.17b shows the gain of the input matching network, where we can observe a G_{max} of about -2.2 dB. Moreover, this G_{max} requires specific combination of source and load impedance and the optimal source impedance slightly differs from the 50 Ω one from the antenna, so the available gain G_A will be lower than G_{max}, which is around -3 dB in the plot. The actual transducer gain when the source is 50 Ω and the load is that of the MRM, is 39.8 dB which only has 0.5 dB degradation due to the slight power mismatch, and this transducer gain has a 3 dB bandwidth of around 2.6 GHz.

The power match situation can also be verified by the two S-parameters, s_{11} and s_{22} that are shown in Fig. 4.18. The input has optimal power match at around 66 GHz and

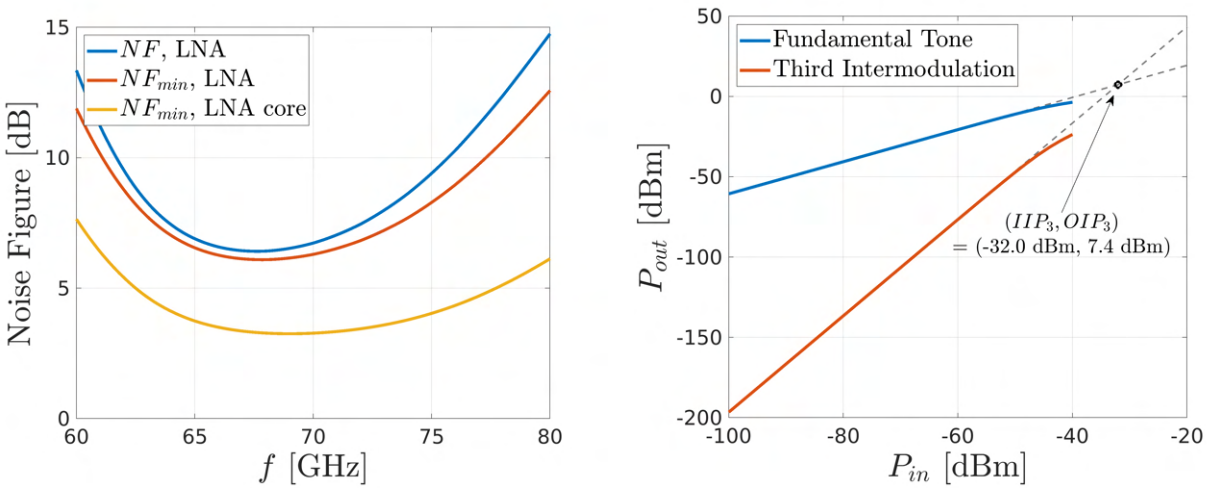

(a) Noise Performance

(b) Linearity Performance

Figure 4.19: Noise and Linearity Simulation Results of the LNA

the output has it around 69 GHz. The noise figures are shown in Fig. 4.19a, where NF is the noise figure with 50 Ω source impedance and NF_{min} is the noise figure with the optimal source impedance. The NF of the LNA is 6.4 dB, which is only 0.3 dB higher than its 6.1 dB NF_{min}, and this indicates that a noise match is fulfilled. However, we can see that compared to the 3.3 dB NF_{min} of the LNA core without input matching network, the NF_{min} of the LNA degrades by 2.8 dB, which is mainly due to the power loss of the input matching presented in Fig. 4.17b. Fig. 4.19b presents the harmonic balance simulation results with an IIP_3 of -32.0 dB. This implies that two achieve lower distortion, we need to operate the LNA with its input power well below this level. The performance metrics of the LNA from simulation are listed in Table. 4.1.

Table 4.1: Summary of LNA Performance from Simulation

Gain	39.8 dB
Center Frequency	69 GHz
Bandwidth	2.6 GHz
Noise Figure	6.4 dB
IIP_3	-32.0 dBm
Power	30 mW

4.5 Microring Modulator Implementation

While the electrical mm-wave frontend is designed to accommodate the entire electronic-photonics system, the design space of the microring modulator itself is not fully explored. From the previous CMT-based analysis, an outstanding MRM should have the following characteristics:

- High refractive index sensitivity to voltage modulation $\frac{\partial n}{\partial V}$. This describes how far the resonance itself can shift with a small-signal voltage modulation.
- High cavity quality factor Q_{cav}, or say low cavity decay rate r_o. This parameter corresponds to the actual change of the power / phase of the optical signal at the through-port, assuming that the resonance frequency is modulated by the same amount.
- High electrical bandwidth. For the implemented MRMs, the P-N junctions are the regions where the refractive index is modulated, which means that the MRM is ideally a capacitive load seem by the LNA. With the help of the matching network, a higher voltage gain to the capacitive junction can be realized that improves the system level performance. However, in order to preserve the optical mode, the metal electrodes are not implemented right next to the junction, and this introduces the series resistance that counteracts the effort of voltage gain enhancement through the passive matching network.

However, these three characteristics do not give us a design space with three degrees of freedom. For example, the doping concentration affects both the strength of effective index modulation and the cavity decay rate, but they usually change in opposite directions. The DC bias voltage presents the similar behavior, and the junction structure exerts even more complicated influence on these optical parameters. The testsite varieties implemented in this design are listed in Table. 4.2 as a summary. In detail, the microring modulators can vary in terms of:

- Grating coupler direction. It determines whether a relatively simple substrate release or a more complex substrate transfer process is required for the optical measurement. This design has most of the grating couplers receiving laser from the silicon substrate side after the substrate release, while it kept four varieties with couplers receiving laser from the top metal side of the chip for potential substrate-transferred packaging.
- Dopant type inside the cavity. This picks the doping concentration from a prefixed set of levels, which affects the decay rate and the refractive index sensitivity of the resonance cavities.
- Junction type. The P-N junctions can be either vertical (for example the P-region is on the top side and N-region is on the bottom side) [49, 50], horizontal (for example the P-region is on the inner side and the N-region on the outer side of the ring),

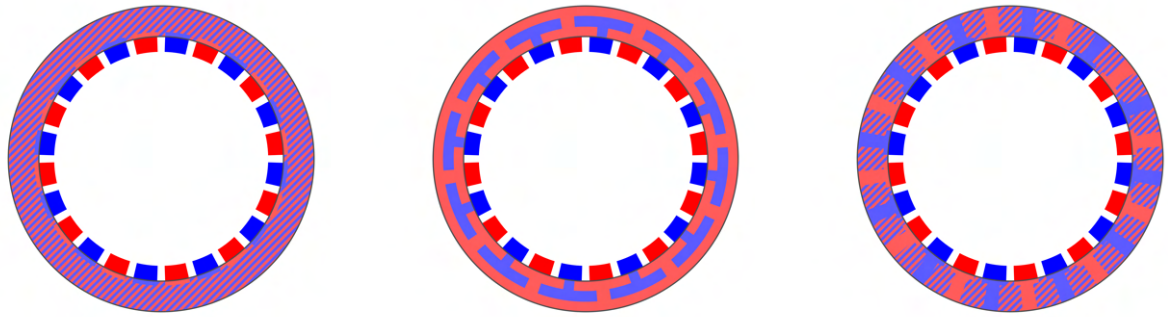

(a) Vertical junction (b) Interleaved junction (c) Hybrid junction

Figure 4.20: Top view of MRMs with different junction types. Red: P-doping; blue: N-doping; interleaved stripes: vertical junction (P-doping and N-doping overlap). Deep red and blue represent regions farther away from the cavity and closer to the electrodes.

interleaved (the P-regions and N-regions interleave along the ring) [51–53], or a hybrid of multiple types. On the optical side, this determines the possible optical modes that can be propagated, the decay rates of the them inside the cavity, together with the refractive index sensitivity. Since a portion of the cavities also forms the ring-to-ring couplers, the junction type also affects the coupling coefficient κ_μ of the optical modes. On the electrical side, the junction type gives requirement for the routing from the metal electrodes to the junctions to preserve the optical mode, which influences the electrical RC bandwidth. In this design, there are three types of junctions implemented: vertical, interleaved with T-shapes [54], and a hybrid of vertical and interleaved, which are shown in Fig. 4.20.

- Coupler type between the bus waveguide and the ring. As shown in Fig. 4.21, we can either have a point coupler where the bus waveguide can directly point to the ring in the main coupling region, or a wrapped coupler where the bus waveguide reaches close to the cavity and then keeps the distance as if it's wrapping the cavity. In this 45nm RFSOI process, the point coupler introduces an undesired multi-mode coupling that potentially brings excessive optical loss, so in order to realize the single-mode coupling, the wrapped coupler is required.

- Fundamental type of the MRM. In this design the single-MRMs and triple-MRMs are implemented. The single-MRMs are implemented as a baseline design. It's also easier to characterize the electrical performance, for example the frequency response of the LNA with these varieties, because we only need to align the laser frequency to the ring's resonance frequency with some offset, while for dual- or triple-MRM we also need to align the resonance split to the RF frequency. There is no dual-MRM implemented in

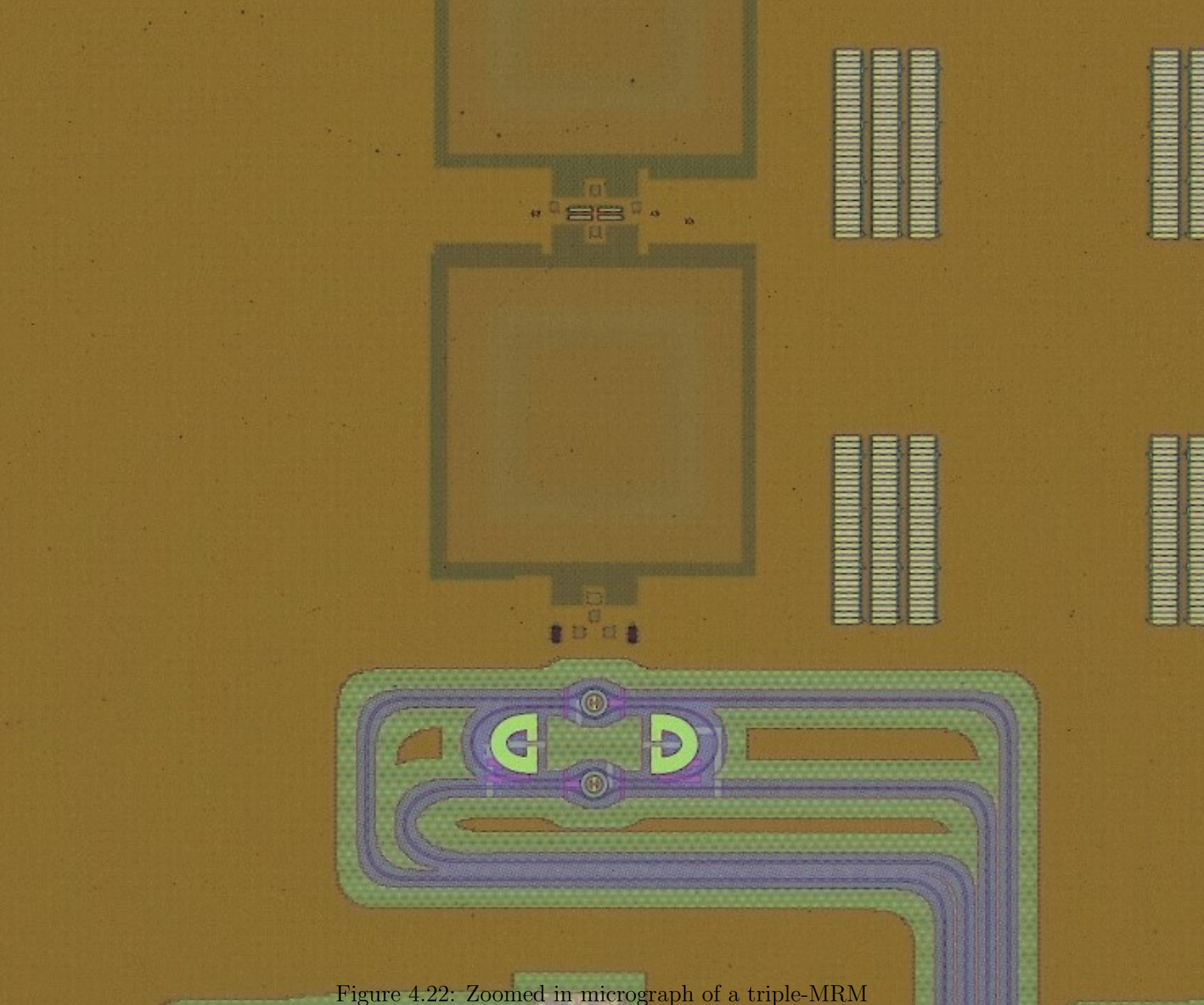

Figure 4.22: Zoomed in micrograph of a triple-MRM

this prototype design, since the ring-to-ring coupler between the two cavities is also a multi-mode point coupler. To realize a wrapped coupler for the triple-MRM, the central ring need to form a peanut shape, which is shown in Fig. 4.22. The heaters are close to the left and right arcs of the central ring, which reduces the thermal coupling to the electrically modulated rings. There is neither doping nor electrodes for the central ring, as it does not need electrical modulation or tuning. To make the measurement more flexible, the drop-port is also implemented for all the triple-MRMs to potentially monitor the optical power from it.

The LNA generates the differential signals, so for the single-MRM, we prefer having both the cathode and anode modulated by the RF signals so that the differential port of the LNA has balanced load, as shown in the left of Fig. 4.23. For the triple-MRM however, there are various possible connection configurations between the LNA and the junctions. For example,

Table 4.2: Ring modulator varieties. Each background color represents one combination of grating coupler direction, junction type and dopant type

Variant #	MRM Type	Coupler Direction	Dopant Type	Junction Type	Frequency Split Target
1	Single	Down	Custom	Interleaved	N/A
2	Single	Down	Standard	Interleaved	N/A
3	Single	Down	Custom	Vertical	N/A
4	Single	Down	Custom	Hybrid	N/A
5	Single	Up	Custom	Interleaved	N/A
6	Single	Up	Standard	Interleaved	N/A
7	Triple	Up	Custom	Interleaved	100 GHz
8	Triple	Up	Standard	Interleaved	100 GHz
9	Triple	Down	Custom	Interleaved	100 GHz
10	Triple	Down	Custom	Interleaved	100 GHz
11	Triple	Down	Custom	Interleaved	60 GHz
12	Triple	Down	Custom	Interleaved	60 GHz
13	Triple	Down	Standard	Interleaved	100 GHz
14	Triple	Down	Standard	Interleaved	100 GHz
15	Triple	Down	Standard	Interleaved	60 GHz
16	Triple	Down	Standard	Interleaved	60 GHz
17	Triple	Down	Custom	Vertical	100 GHz
18	Triple	Down	Custom	Vertical	100 GHz
19	Triple	Down	Custom	Vertical	60 GHz
20	Triple	Down	Custom	Vertical	60 GHz
21	Triple	Down	Custom	Hybrid	100 GHz
22	Triple	Down	Custom	Hybrid	100 GHz
23	Triple	Down	Custom	Hybrid	60 GHz
24	Triple	Down	Custom	Hybrid	60 GHz

we can have both the cathodes and anode of the two rings modulated by the differential RF signal through the bias network, or only have the cathodes modulated when anodes are biased by the DC voltage, which are shown in the middle and right of the same figure. It seems connection configuration in the center benefits from two times of the modulation voltage but it's not the case: both $RF+$ and $RF-$ see a load impedance that is 1/4 of that in the right side configuration, so when the bi-conjugate match is realized, both configurations deliver the same amount of modulation power to the load, so the voltage amplitude of $RF+, RF-$ in the center will be 1/2 of that in the right. For common-mode signals in practice, the central configuration is better, as the common-mode voltage of $RF+/RF-$ will both apply to the cathodes and anodes, which does not affect the instant bias condition of the ring modulator. On the contrary, for the connection on the right, the common-mode signals are applied to the cathodes of the rings and forms the undesired common-mode signal path. In this design, we still choose to have only cathodes connected in order to have routing wires

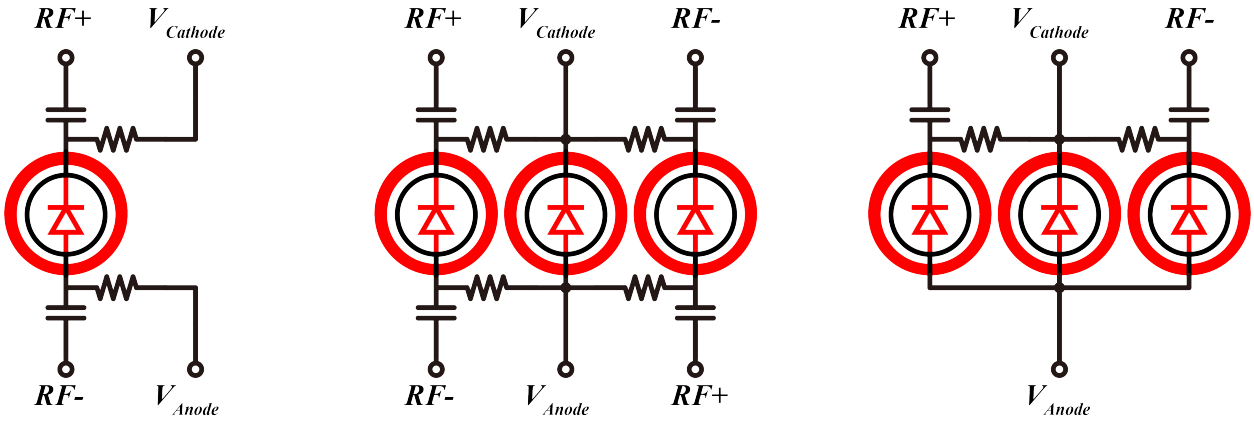

Figure 4.23: Signal connections for modulation. Left: single-MRM. Middle: triple-MRM with both electrodes modulated by RF signals. Right: triple-MRM with only cathodes modulated by RF signals

with less parasitic capacitance and to monitor the bias condition of the rings. The central ring will be electrically "floating" the central ring does not go through any PN junction.

4.6 Measurement Results

The design [2, 3] is implemented in a commercial 45nm SOI process. It includes a standalone LNA together with multiple variants of LNA-MRM systems. The micrograph of the fabricated chip is shown in Figure 4.24. The fabricated chip is flipped and packaged on an organic substrate via the on-chip bump pads. The RF input signals are routed from the bump pads to the probe pads on the top layer of the organic substrate, while all the other signals are routed to the ball grid array (BGA) on the back side of the package.

As all the top level signals of the design are analog signals and there are a large amount of variants in this design, the organic substrate package is assembled on a chip board used to fan out these signals. Fig. 4.25a shows the diagram of the measurement setup. Fig. 4.25b and Fig. 4.25c is the photo showing the measurement setup details close to the chip and the diagram showing the landing of the critical components, respectively. The static power and bias signals are generated from the data acquisition (DAQ) system to the chip board and reaches the on-chip circuits and photonics via the BGA. The fiber array is attached from the removed substrate side to the chip, which couples the continuous wave (CW) laser into the chip, and also couples the optical signal at the through-port of the MRM out of the chip to an optical spectrum analyzer (OSA). The optical measurements of the MRMs can be done and the results are shown in Fig. 4.26. Here Fig. 4.26a shows the optical response of a triple-MRM variant to the laser wavelength with different heater voltages for the central cavity. The brighter region implies a state closer to on-resonance and three

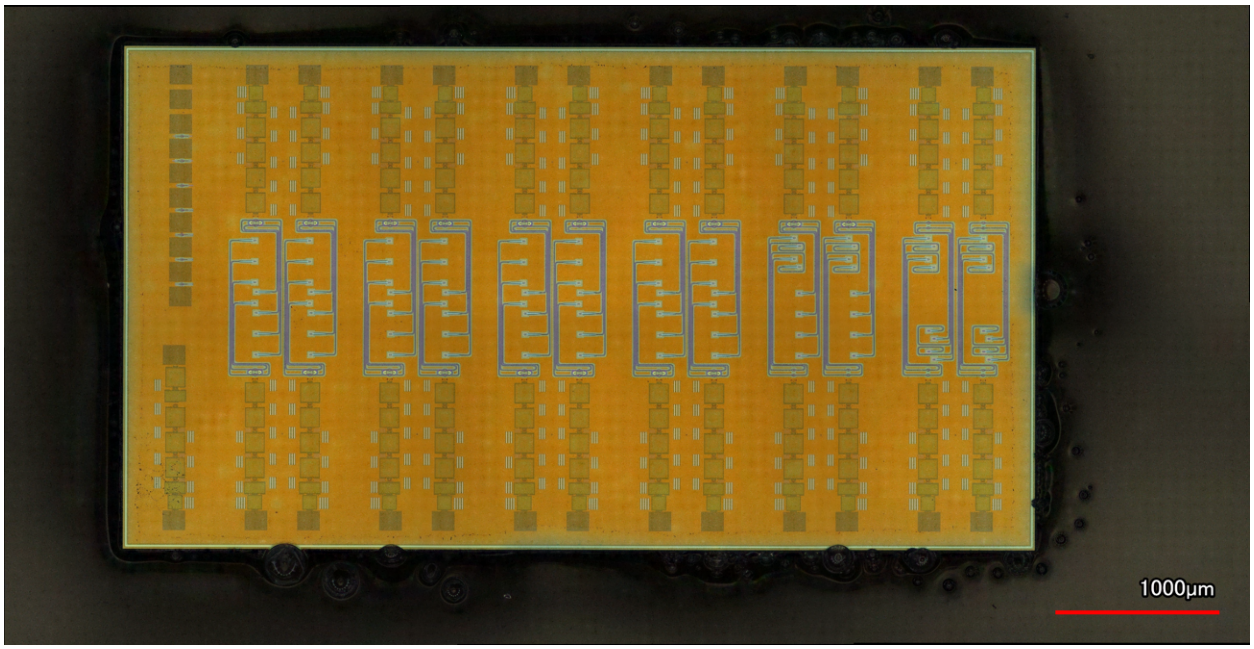

(a) Full chip view

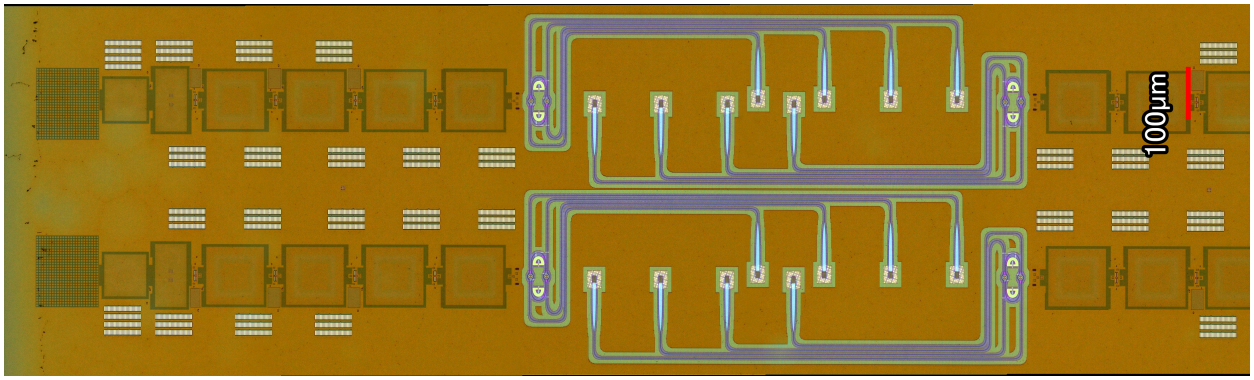

(b) Zoomed-in view of two adjacent testsites

Figure 4.24: Chip micrograph

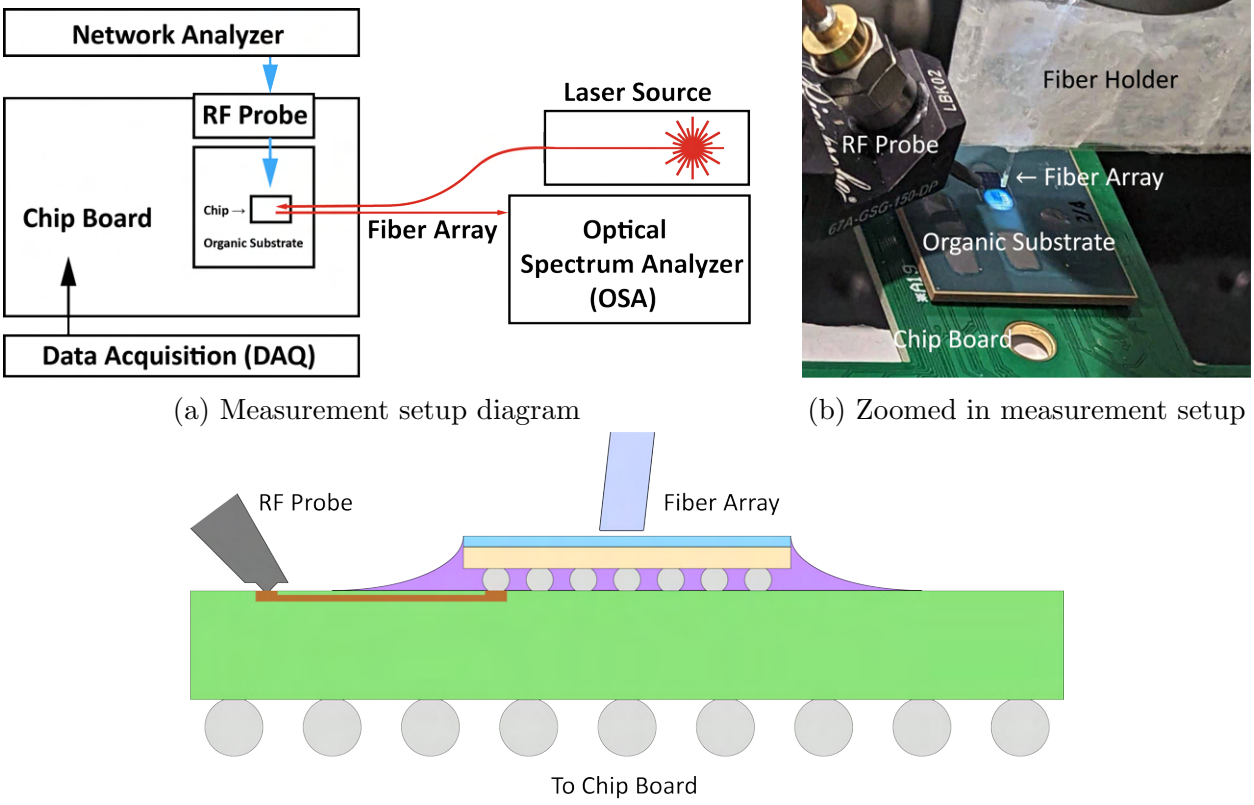

(a) Measurement setup diagram

(b) Zoomed in measurement setup

(c) Landing of the RF probe and the optical fiber array on the substrate released package

Figure 4.25: Measurement setup

supermode resonances close to each other can be observed. There are additional weaker resonances observed that represent the other intrinsic resonance of the central cavity since its free spectral range (FSR) is smaller than the modulated cavities. Due to the mismatch of intrinsic resonance frequencies between the central cavity and the modulated cavities, there is existing detuning even with zero heater power so that the two outside supermodes do not have equal split between the central supermode. The resonance wavelength splits can be extracted from Fig. 4.26a and translated to the resonance frequency splits, one of which is plotted in Fig. 4.26b proving the tunability of the triple-MRM.

The high frequency RF signal is transmitted from the network analyzer to the RF probe that is landed on the probe pads of the organic substrate, and the transmission lines on the organic substrate route the RF signal all the way from these probe pads to the RF bump pads of the chip. The mm-wave signal at frequency f_{RF} is transmitted from a vector network analyzer (VNA). It gets amplified by the on-chip LNA and modulates the MRM to generate an optical sideband that is located f_{RF} away from the CW laser frequency, as shown in

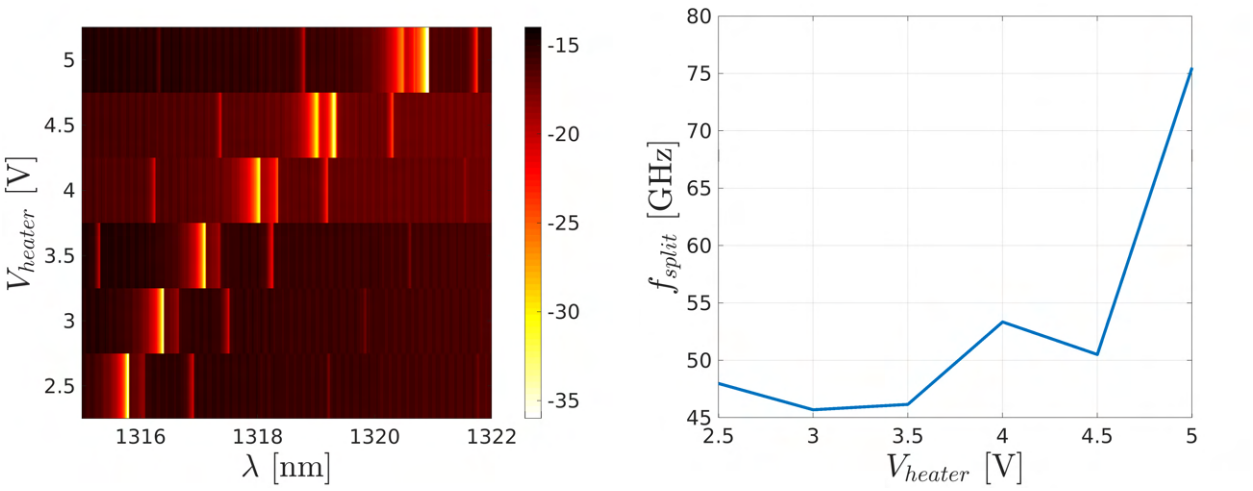

(a) Wavelength response of the triple-MRM with different central heater voltages

(b) Frequency split between two of the supermodes

Figure 4.26: Resonance detuning of the central cavity

Fig. 4.28.

During the measurement, we need to first find out the center frequency of the LNA driving the MRM, which might be different from the standalone LNA. Thus in the first step, the RF power is fixed and its frequency is being swept, the amplified RF signal modulating the MRM will generate heat and hence result in a resonance frequency shift. It is observed that this shift peaks when the RF frequency is around 57 - 58 GHz, and this frequency should be the center frequency of the LNA driving the MRM. This center frequency is lower than what we expect, possibly due to the influence from the Cu pillars and pads that are close to the transformers.

The standalone LNA measurement also confirms the discrepancy in terms of the centerr frequency. Meanwhile, the s_{11} matches the simulation result while the behavior of s_{22} is not as expected. One possible reason is that the routing from the LNA output bump pads to the on-package probe pads on the on the organic substrate has relatively long traces with vias, which generate the undesired reflections. The measured s_{21} of the standalone LNA is thus lower than simulation because of the power mismatch.

Figures 4.28-4.31 show the further measurement results that are more related to the link performance of a single-MRM variant and a triple-MRM variant with the same dopant and junction type. Among them, Fig. 4.28 shows the definition of the parameters that are extracted from the optical spectrum. In this scenario, the sideband conversion efficiency equals the ratio of the sideband peak power to the off-resonance through port power. For the single-MRM measurement, the measured off-resonance power is -15 dBm when the optical power from the laser source is 0 dBm, and this reflects to a loss of 15 dB along the optical

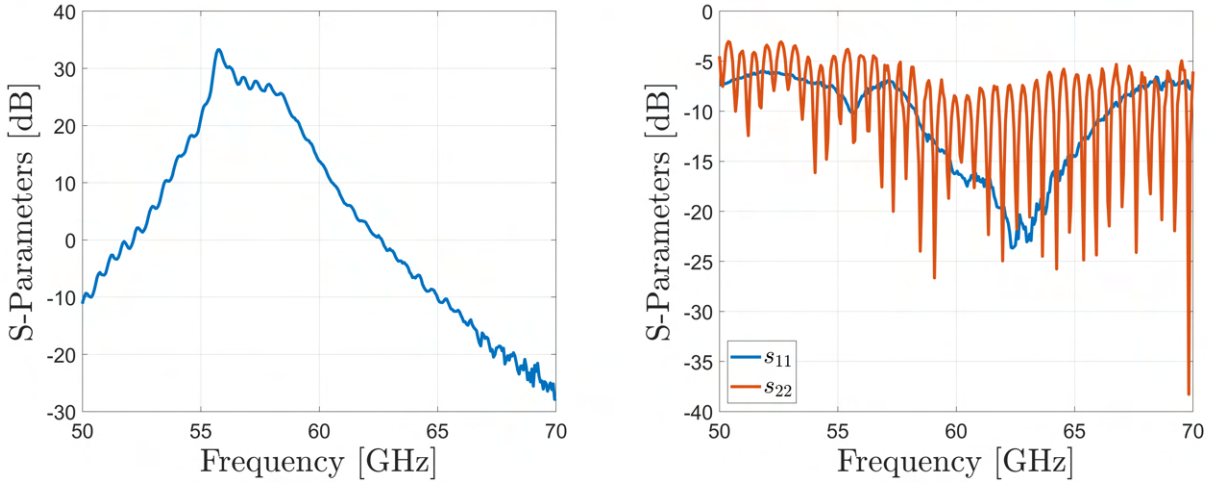

(a) s_{21} (b) s_{11} and s_{22}

Figure 4.27: Measured S-parameters of the standalone LNA

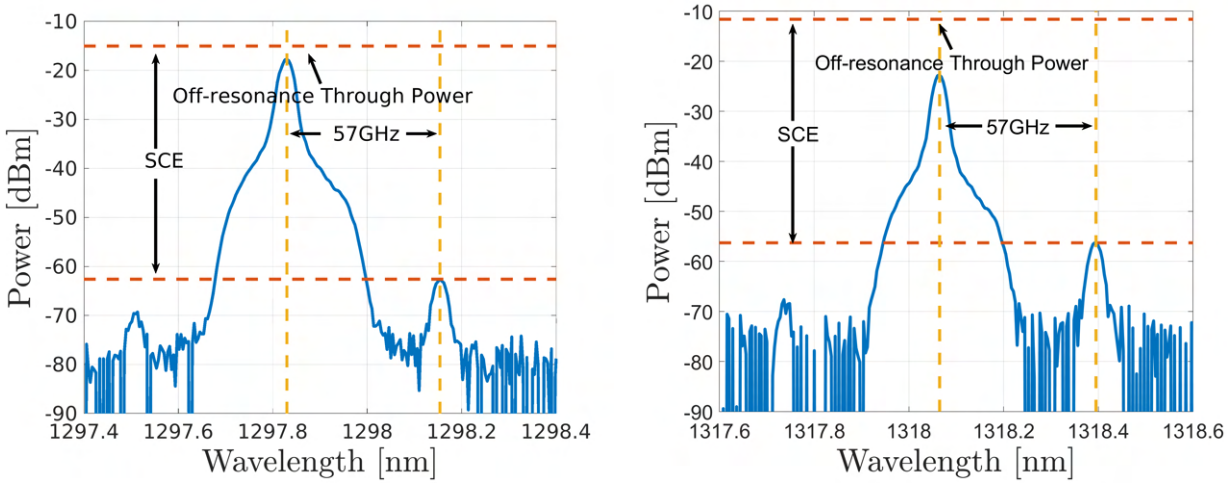

(a) Single-MRM (b) Triple-MRM

Figure 4.28: Measured optical spectrum

path mainly contributed by the grating loss of the couplers due to imperfect fiber-coupler alignment. Fig. 4.28b reflects the spectrum when the laser power is 6 dBm and the loss from the two couplers are around 17 dB. In practice with improved coupling conditions, the loss can be as low as 2 dB per coupler, which reduces the overall coupling loss from around 16 dB in the experiment significantly down to around 4 dB.

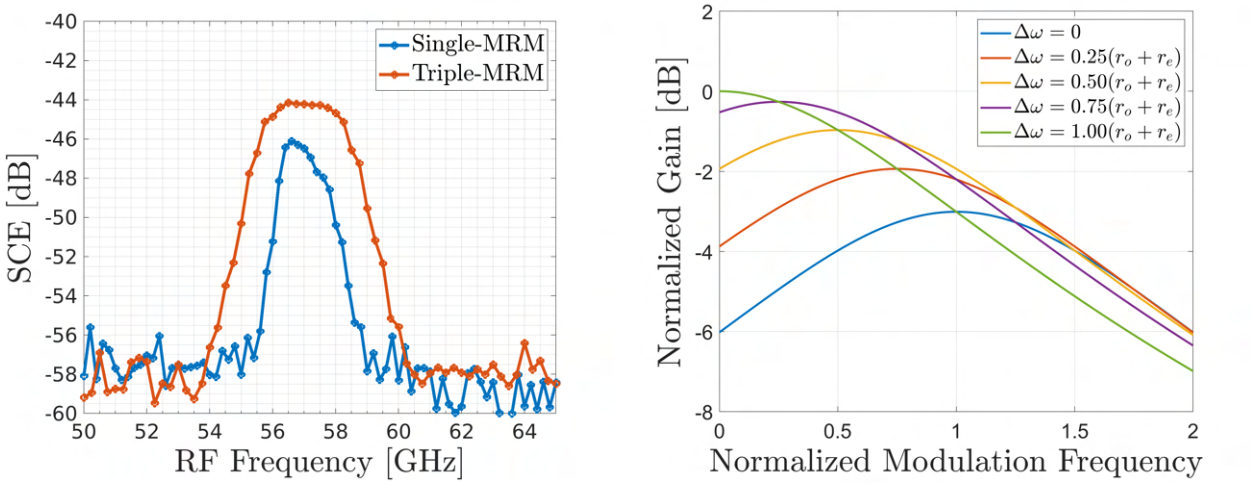

(a) Measurement results

(b) Simulation results across different detunings

Figure 4.29: Frequency response of SCE

Fig. 4.29a shows the SCE as a function of RF frequency when the laser frequency, resonance frequencies and split of the MRM variants are all fixed to maximize the SCE. They both peak at 57 GHz that indicates the central frequency of the LNA's transducer gain. This central frequency is lower than the 70 GHz one from simulation shown in Fig. 4.17a, possibly due to the influence from the AC-grounded bump pads on chip or the interaction between adjacent LNA variants. The triple ring variant presents a passband of ∼3.2 GHz, and the LNA is the dominant source that limits this bandwidth. The similar plot for the single-MRM variant however, shows a narrower bandwidth of ∼2 GHz and a more asymmetric response. The steeper roll-off is caused by the fact that the sideband offset from the resonance frequency is comparable with the optical bandwidth, and the asymmetry can be explained by taking several equal-$\Delta\omega$ sections in Fig. 2.4, which reveals the fact that a detuning that maximizes the SCE at a specific modulation frequency does not guarantee that SCE with this optimal detuning peaks at such modulation frequency, as shown in Fig. 4.29b.

Fig. 4.30 illustrates the relationship between SCE and the RF power under different optical power levels, and from SCE the Noise Figure can be projected based on Eq. 3.9 and Eq. 3.19, which are shown in Fig. 4.31. The plot shows the link begins to saturate around -35 dBm input RF power, which is expected as the LNA has a high transducer gain. For the single-MRM variant, no significant difference is observed among the curves of SCE when the optical power increases, and this implies that with high optical power levels which usually causes degrading effects like self-heating or carrier absorption, high optical power levels, for example up to 4 dBm, do not result in considerable performance degradation in the single-MRM sensing element, so its projected NF scales well with total laser power. The triple-MRM variant however, confronts a strong performance degradation at high laser power

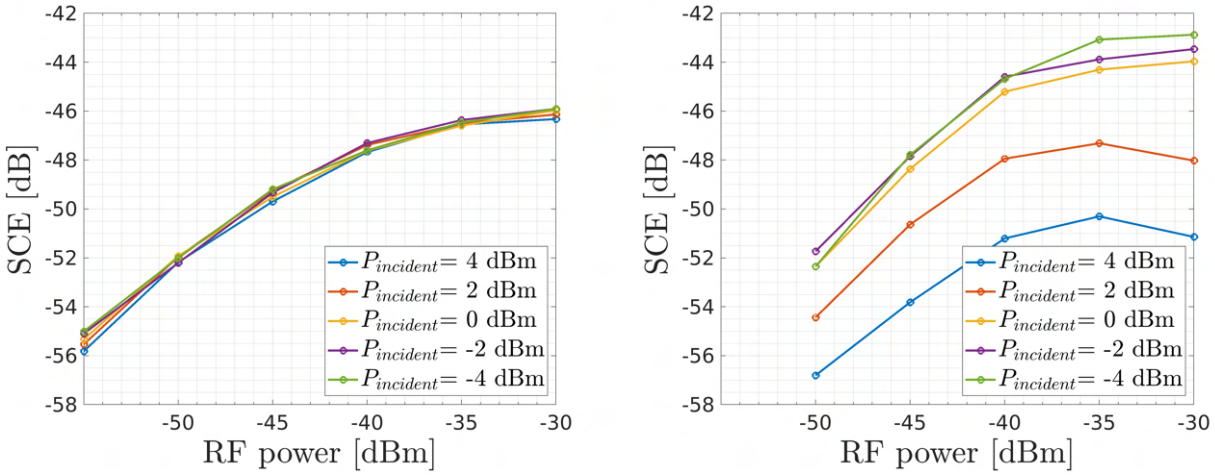

(a) Single-MRM variant

(b) Triple-MRM variant

Figure 4.30: Sideband conversion efficiency v.s. RF power

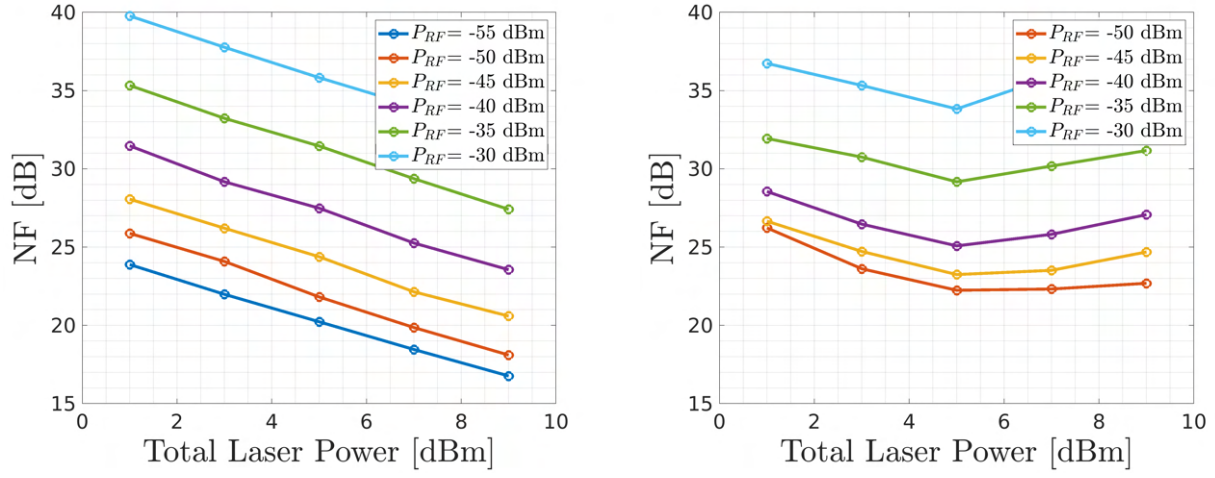

(a) Single-MRM variant

(b) Triple-MRM variant

Figure 4.31: Projected NF v.s. total laser power assuming 2dB loss per coupler

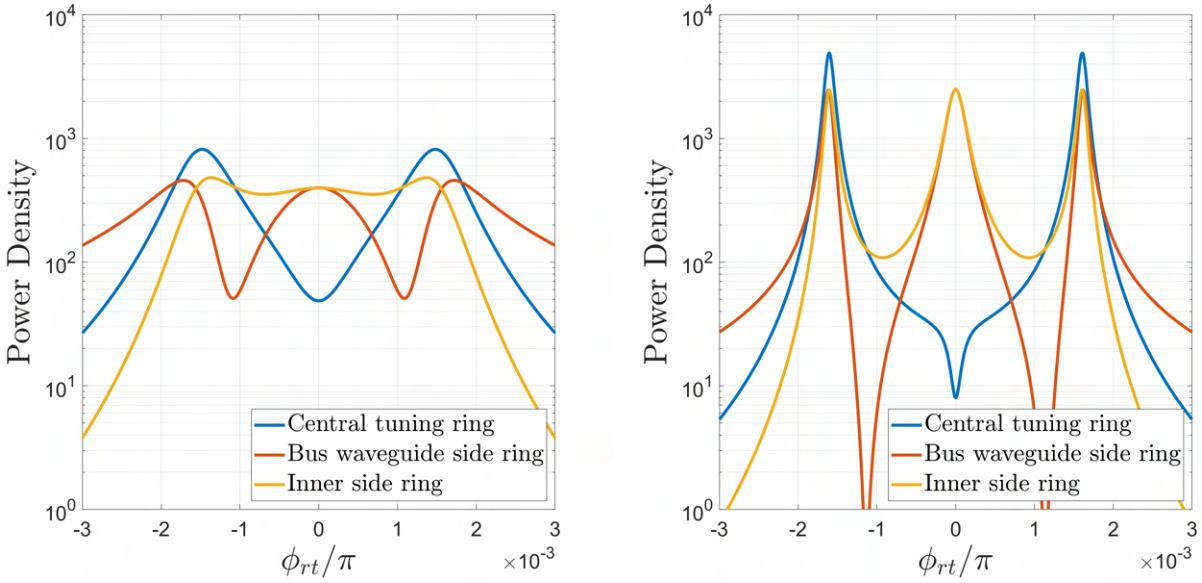

(a) Cavities with low Q

(b) Cavities with high Q

Figure 4.32: Normalized power densities in the three microring cavities of the triple-MRM

levels, which prevents a lower NF figure by increasing the laser power. To find out whether this results from the high-Q undoped central cavity, a model is built to characterize the power densities inside the three cavities with respect to different round-trip phase shift, or equivalently the laser frequency. The results are shown in Fig. 4.32, and the conclusion from these results is that at the left and right supermode resonance frequencies, the power density in the central cavity is always about twice of that in the two cavities being modulated, no matter how large the decay rate of the cavities are or how large the ratio of these decay rates is. Since all the three cavities should have similar circulating optical power compared to the single ring, the most reasonable explanation for this performance degradation is that the central cavity didn't have electrodes that help to sweep out the carriers.

The measured SCE matches the theoretical model, and is mainly limited by the RC bandwidth and the relatively low quality factor of the single-MRM variant measured so far. The noise figure of LNA+single-MRM is still comparable to that of a standalone dual-MRM [20], which intrinsically has better SCE than the standalone single-ring MRM tested in this LNA+single-MRM experiment. Hence, the performance of the proposed architecture can be further improved by integrating the LNA with these more efficient MRMs. Table 4.3 compares this design with previous work that focused on MZMs, illustrating that smaller footprint and power per element as well as higher modulation frequency are achievable with pre-amplified MRM designs, owing to the large load capacitance and area of the MZM designs. The resonant nature of MRMs also enables wavelength division multiplexing compared

Table 4.3: Comparison with State-of-the-Art RF Photonic Modulators/Front-ends

Reference	This work [2, 3]		*Fio+LS 2019* [20]	*JLT 2023*[55]		*RFIC 2019*[56]
Monolithic Integration	Yes		NA	NA#	No*	No
Driver Process	45 nm RFSOI		NA	NA	Discrete	130 nm SiGe BiCMOS
Electrical Power [mW]	30‖		-	-	5000	1700
Optical Modulator	Single-MRM	Triple-MRM	Dual-MRM	MZM	MZM	MZM
SCE [dB]	-49.5 @ -45dBm P_{RF}	-47.8 @ -45dBm P_{RF}	-42 @ -20dBm P_{RF}	-	-	-
Laser Power [dBm]	9	5	9	4.8	30	-
NF [dB]	20.6§	23.3§	37.9	43	11.1	20
Frequency [GHz]	57	57	41	20	20	20

‖heater tuning power up to 16 mW excluded
#without EDFA or pre-amplifier
*with 2 EDFAs and 1 pre-amplifier, output power of the EDFA is taken as a laser source power
§projected NF assuming a 50% split and 2dB loss per coupler (P_{laser} -4dB incident power at the MRM)

to broadband MZM designs, enabling scaling to larger arrays due to more sensing elements per fiber. The power consumption per array element is 30 mW from the LNA, which shows that thousands of such elements can be integrated in a low-power mm-wave sensing array.

4.7 Chapter Summary

The chapter introduces the design considerations, procedures and measurement results of a mm-wave sensing element in the transmitter array for the proposed architecture. The element with single-MRM variant can achieve a noise figure of around 20.6 dB with less than 30 mW of electrical power and 9 dBm of laser power per element. The element with triple-MRM variant provides 23.3 dB noise figure with the same electrical power and 5 dBm laser power. The triple-MRM variant shows some extent of advantage over the single-MRM one, especially when the laser power is low. In the case of a high laser power level, the triple-MRM variant degrades due to the lack of carrier sweep-out electrodes, and this revision will be applied in future designs. The advantage of the triple-MRM variant is lower than the prospective, which results from the relatively high decay rate or say the relatively low quality factor of the cavity. With improved monolithic design platform, we will have more degrees of freedom in the MRM design space, so we expect to have a lower decay rate so that the triple-MRM gets more advantage over the single-MRM, and a higher resonance shift from modulation together with larger electrical bandwidth that both enhance the performance of the general MRM family.

Chapter 5

Transmitter Array Element Design in A Silicon Photonic Platform

This chapter introduces the design of the transmitter array element in a commercial RF-SOI process optimized for silicon photonic applications [57] targeting 60 - 70 GHz carrier frequency. On the electronics side, the performance of the CMOS devices in this process technology is very close to that in the previous RFSOI technology. On the photonics side, more MRM varieties are available with the process optimization, and the a thick buried oxide layer is present so that the substrate release post process is no longer required to preserve the optical mode.

5.1 Active Core with Input Matching

The active core design principles and methodology are very similar to those in the previous chapter, as the optimized silicon-photonic platform does not have significant change in the performance of the CMOS devices. One of the change is that the previous design utilizes the vertical natural capacitor (VNCAP) formed by the BEOL metal layers and dielectrics. Although VNCAP offers higher quality factors, the drawback is the relatively lower capacitance

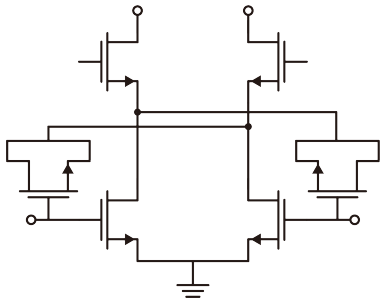

Figure 5.1: Neutralization MOS capacitors implementation

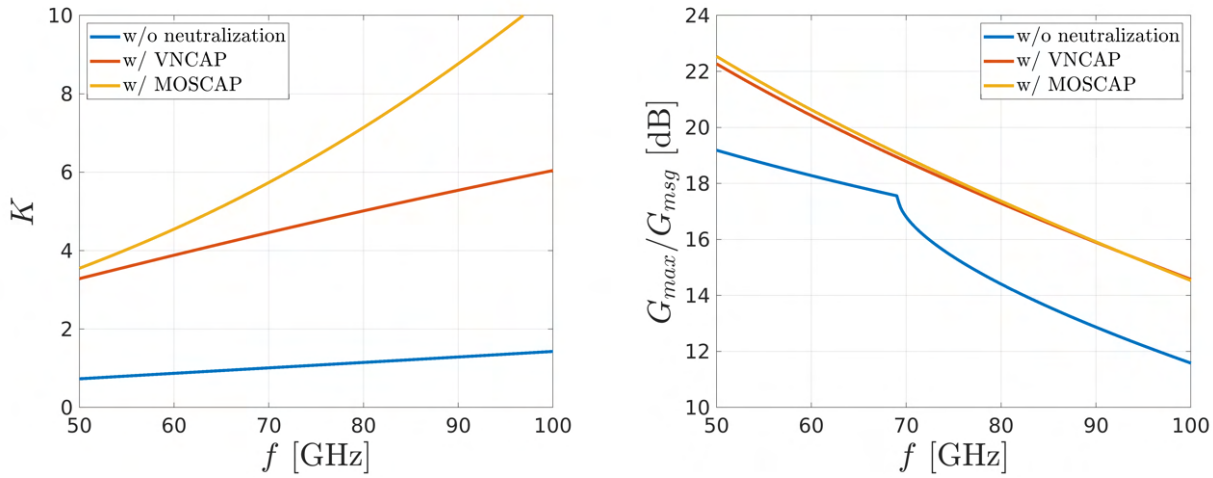

(a) Stability factor K

(b) Maximum available / stable gain

Figure 5.2: Comparison between different neutralization techniques

density and the additional design rule constraints (DRC) that might add additional routing parasitic resistors or capacitors to the design. In addition, the performance improvement of the neutralization highly depends on the good matching between the C_{gd} of the transistors and the neutralization capacitors, and is prone to process variations.

There are designs that implement transistors for neutralization [58, 59], and this design chooses the topology depicted in Fig. 5.1. The two neutralization transistors are of the same type with the common-source transistors with half the size. Each neutralization transistors has its source connected to its drain as a MOSCAP. During normal operation, the two common-source transistors are in the saturation region so that their gate-to-drain voltages are not able to turn a MOSFET or MOSCAP of the same type on into the strong inversion region. Thus, the channels of the two MOSCAPs do not have high concentration of the minor carriers, and their gate to source/drain capacitors exclude the channel capacitance and include only the gate to source/drain fringe parasitic capacitance. The same origination of the parasitic C_{gd} of the common-source transistors and the C_{neu} guarantees good matching and neutralization quality across process, voltage and temperature (PVT) variations [60, 61].

Although MOSCAPs take advantage of robustness, their relatively lower quality factor raises design concerns in terms of performance degradation. Therefore, the post-extraction simulations of VNCAP- and MOSCAP-based neutralization are done and the results are shown in Fig. 5.2, and the results with no neutralization are also attached as a reference. Fig. 5.2a presents the stability factors where both designs show the unconditionally stable state in the frequency range of interest compared to the reference. Since both neutralization designs have K well above 1, the exact values don't really matter as its upper limit depends on the precise matching of the capacitance. Fig. 5.2b shows the maximum available gain

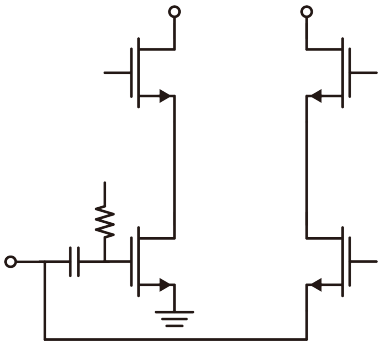

Figure 5.3: Schematic of the active Balun

plots, giving the fact that both neutralization designs achieve better gain over the reference design although they have maintained a higher K, and the gain performance between these two does not differ a lot. Given the fact that no significant performance degradation is observed in MOSCAPs, they are employed in the active stages for designs in this process platform.

One other change is that we are gradually targeting the operation in a larger frequency range, so the active balun [62, 63] is replacing the passive one for a wide-band input matching and also for reducing the inductor/transformer footprint. The schematic of the active balun used in this design is shown in Fig. 5.3. The core of the balun is a common-source transistor and a common-gate transistor. The incoming signal directly applies to the source of the common-gate transistor directly and to the gate of the common-source transistor indirectly through the ac-coupling network. The two transistors are biased with the same current density so their small-signal parameters are close, so that the strengths of voltage signals that appear at the drains should have similar strength while in the opposite directions if they have the balanced load impedance. Effectively, the differential signals will appear at the drains. Similar to the differential active stages, the common-gate transistor pair is added to further boost the maximum available power gain.

The wide-band matching is obtained through the following mechanism: for a common source transistor where the gate capacitance mainly contributes by C_{gs} and the series gate resistance R_g exists. The voltage amplitude with fixed power applied highly depends on the equivalent shunt resistance that is given by:

$$R_{eq,CS} \approx (1 + Q_g^2)R_g, \qquad Q_g = \frac{1}{\omega R_g C_{gs}} \tag{5.1}$$

and for the differential pair, this equivalent resistance is $R_{eq,CSdiff} = 2R_{eq,CS}$. The ratio of the equivalent resistance to $50\,\Omega$ of the source can be much higher than 1, and with larger ratio, we will suffer from narrower bandwidth from a single-stage matching network.

For the active balun however, the input also sees a common gate stage. Together with

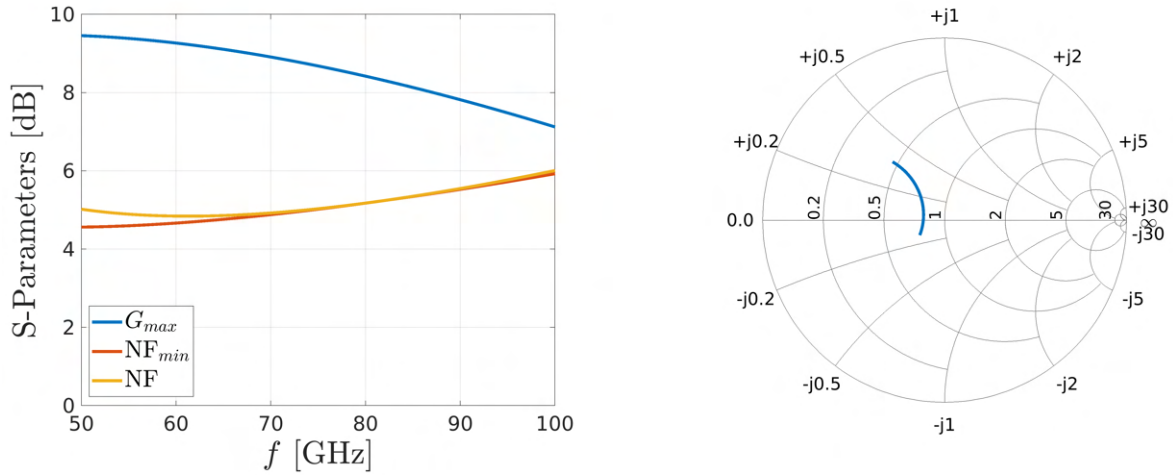

(a) Gain and Noise

(b) s_{11} Smith chart

Figure 5.4: Performance metrics of the active balun

the common-source transistor, its equivalent resistance is:

$$R_{eq,abl} = \frac{1}{1/R_{eq,CS} + 1/R_{eq,CG}} \qquad R_{eq,CG} \approx \frac{1}{g_{m,CG}} \tag{5.2}$$

This can give us a much lower equivalent resistance, with 2 - 4 mA of bias current through the common-gate branch, $R_{eq,CG}$ can be close to 50 Ohm, which leads to a close-to-matched status. A wide-band matching is therefore realized noticing that this equivalent resistance is not strongly frequency dependent.

Nevertheless, the bandwidth feature of the active balun is with the cost of a lower G_{max}: assume that the matching networks that do the power match from the 50 Ω source to the common-source differential pair or the active balun are lossless, the power applied to the active stage's input should be the same, so for the voltage amplitude we have:

$$\frac{v_{amp,abl}}{v_{CSdiff}} = \frac{\sqrt{PR_{eq,abl}}}{\sqrt{PR_{eq,CSdiff}}} \approx \frac{1}{\sqrt{2g_{m,CG}R_{eq,CS}}} \tag{5.3}$$

As the bandwidth of the matching network is highly correlated to the ratio of the two resistive terms before and after matching, the lower G_{max} is inevitable for the active balun if the target is a wide band power match. The designed active balun still achieves a G_{max} of around 9 dB from simulation shown in Fig. 5.4a. This is 9 dB lower than the common-source differential pair. However, considering that the additional matching network is required for the common-source differential pair, which has a large footprint and brings the additional loss of 2 - 3 dB due to limited quality factor, it is still worthy to implement such active balun. Fig. 5.4a also shows the noise performance of the active balun, where the minimum noise

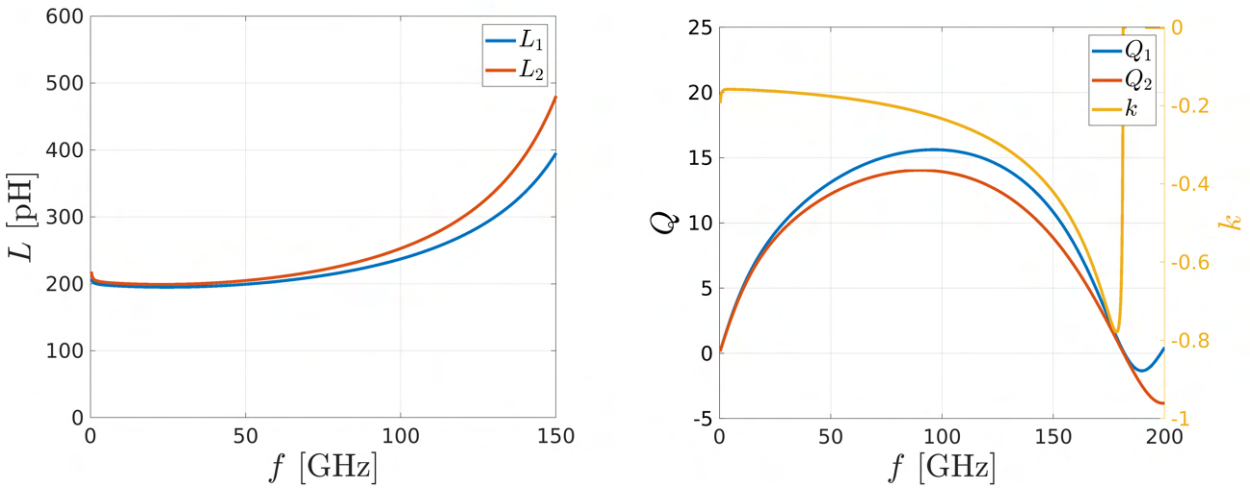

(a) Inductance

(b) Quality factor and coupling coefficient

Figure 5.5: Performance metrics of the weakly-coupled transformer

figure and the noise figure are both around 5 dB and they are almost the same. This is a sign of the noise match at the same time. Fig. 5.4b depicts the s_{11} of the active balun. Since it drives the following stages, the s_{11} of the entire LNA will change a bit, which will be explained later.

5.2 Bandwidth Extension

The proposed transmitter array element requires the center frequency of the LNA and the split of the dual-/triple-MRM to be aligned in order to achieve optimal conversion efficiency and noise performance. So to demonstrate the tunability of the MRM integrated with the circuits, we would prefer an LNA with wider bandwidth. One common approach is to employ the weakly coupled transformers [28, 64, 65], which has very similar electro-magnetic mechanism compared to the multi-MRM. Since the quality factor of the on-chip inductors are usually not too high, such mutual coupling and split can easily create a significantly higher bandwidth.

In addition to the design considerations of inductance and quality factors for normal inductors or transformers with strong coupling, the coupling coefficient is what we need to take special care of for the weakly-couple transformer. The reason is that although we would like to have weak coupling to make the split flat with less ripple, the low k potentially gives us a worse insertion loss, especially when the quality factor of the inductors are not high enough [66]. In this design, based on the quality factors obtained during the iterative design, we would like to have a k that is around 0.2. The EM simulation results of the designed weakly coupled transformers is shown in Fig. 5.5. The inductance of the primary and the

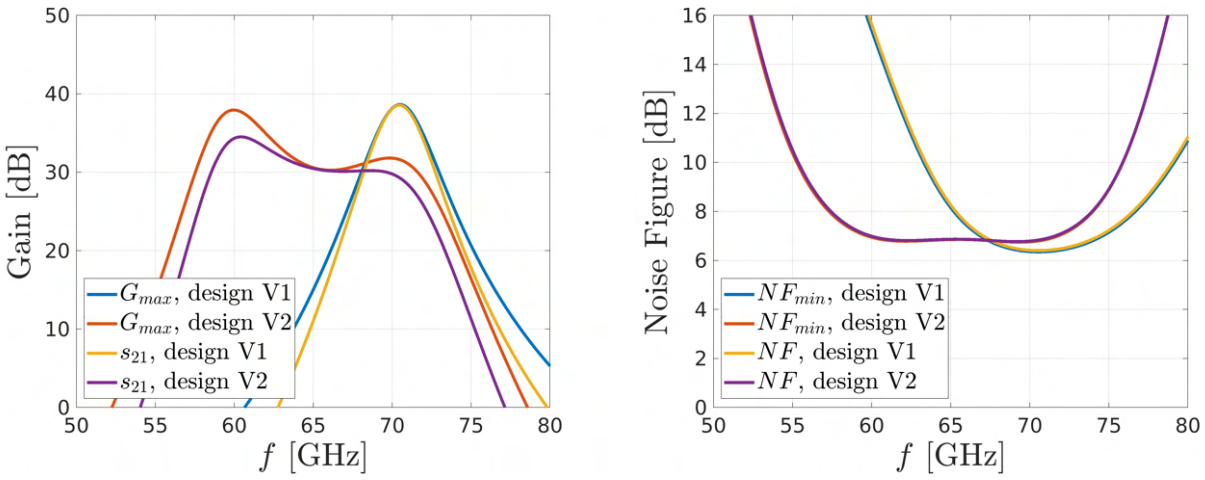

(a) Gain (b) Noise figure

Figure 5.6: Gain and noise performance of the two LNA designs

secondary coil are both close to 22- pH in the frequency range of interest around 60 - 70 GHz. At higher frequencies however, due to the parasitic capacitance, the effective inductance increases while the quality factors Q decreases until it reaches the self-resonance frequency.

With this new silicon-photonic process platform, we have two versions of LNA designs. The first version has the active balun and the neutralization MOSCAP implemented, and the second version has the weakly coupled transformers featuring bandwidth extension placed. Their simulated performance metrics are shown in Fig. 5.6 and Fig. 5.7. V1 has its power gain that reaches around 38.5 dB peaking at 70 GHz with a bandwidth of 2.5 GHz. With bandwidth extension, the LNA power peaks at 60.4 GHz with reaching 34.5 dB with a 3 dB frequency 58.8 GHz to 65.4 GHz. In addition, the bandwidth-extended LNA also has a secondary gain plateau around 31 dB, which keeps the gain curve nearly flat above 29 dB until the frequency approaches 71 GHz. Fig. 5.6b reports that the noise figure is 6.4 dB for design V1 and 6.8 dB for design V2, while design V2 keeps this noise figure within a much wider frequency band. The s_{11}, s_{22} of the two designs are plotted in Fig. 5.7. Both designs has realized input and output matching. Design V2 has much better input matching because an additional shunt inductor is implemented at the input of the active balun to resonate out the parasitic resistance. This inductor was placed together with the on-chip probe pads so it does not necessarily increase the area of the design. The performance metrics are summarized in Table 5.1.

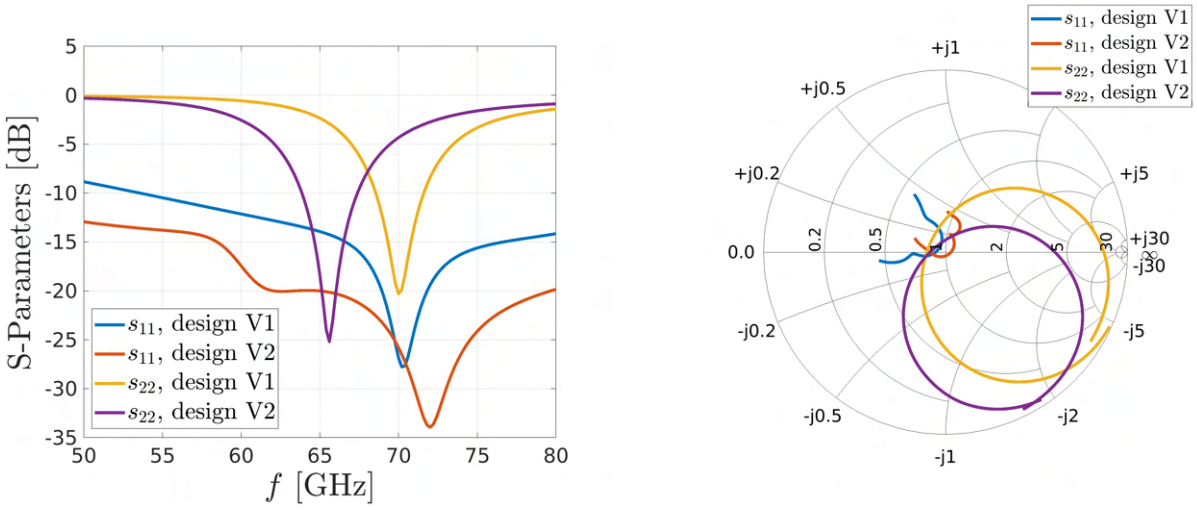

(a) Rectangular plot

(b) Smith chart

Figure 5.7: Gain and noise performance of the two LNA designs

Table 5.1: Summary of LNA Performance from Simulation

Design	V1	V2
Peak Gain	38.5 dB	34.5 dB
Peak Frequency	70.0 GHz	60.4 GHz
Operating Frequency Range	69.2 - 71.7 GHz	59.0 - 71.0 GHz
Noise Figure	6.4 dB	6.8 dB
Power	25 mW	36 mW

5.3 Photonics Implementation and Chip Integration

The high-precision thermal tuning is always critical in terms of MRM implementation and operation. The design in the previous chapter works as a proof of concept and there are enough bump pads available to control the individual heater power for all the MRMs from the external voltage source. In a practical system however, these heater control signals should be generated locally, and this design chose to implement the relative compact pulse density modulation (PDM) driver. The diagram of the driver is shown in Fig. 5.8, the 10-bit adder calculates the sum of the configuration bits and the bits stored in a 10-bit register. The MSB of the 11-bit sum or say the carry signal is the output of the digital block, and the register takes the remaining 10 bits as the input in the next clock cycle. The output is connected to the gate of a heater driver head which is a wide NMOS transistor. When the

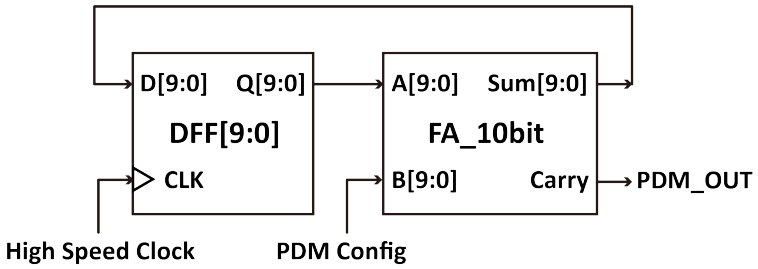

Figure 5.8: Diagram of the PDM Driver

carry signal voltage is high, the NMOS is on, so that the current flows through the heater from the high-voltage supply; when the carry signal voltage, the NMOS is off and there will be no current flowing through. The average heater power is therefore the product of the on-state power and the pulse density controlled by the configuration bits. This PDM driver requires a clock signal to update the registers and to avoid EO conversion from this clock signal, this clock frequency should be moderately high, so that the switching fall into a frequency band that is far beyond the thermal bandwidth and filtered out by the slower heat dissipation process. In this design, this high speed clock frequency is designed to be around 1 GHz.

In addition to the thicker BOX layer, this silicon photonic platform also has plenty of custom options available for the photonics design compared to the previous RFSOI process platform, one of which is the partial etch option that creates thinner silicon waveguide layers and forms a rib structure. Fig. 5.9a presents the only available waveguide in the previous 45 nm RFSOI platform which is the so called full-silicon waveguide. For an active modulator, the P-N junction need the electrical connection to a contact and to a metal layer, and the full-silicon waveguide needs a long extension before connecting to the metal electrodes need to prevent the optical mode leakage. Furthermore, both the cathode and the anode electrodes are located inside the ring cavity to preserve the optical mode, and this decreases the effective width of the extensions as they need to interleave. Both factors decrease the RC bandwidth because silicon has higher resistivity than metal even if it is heavily doped and in addition, the tuning efficiency of the heater located at the center of the ring will also degrade because the mode-preserving extension increases its physical distance between to the cavity.

With the feature of partial etch, the first potential optimization is to make the extensions thinner. The electrodes of anodes and cathodes are still all at the inner side of the cavity, so that the half-rib structure depicted in Fig. 5.9b is formed. The junction structures shown in Fig. 4.20 for full-silicon waveguide are all available for half-ring waveguide, and because the cavity has significantly better optical mode confinement which results in a shorter required extension, one benefit is that the heater can be placed closer to the cavity and a better tuning efficiency can be achieved. In the sense of the sideband conversion efficiency, however, it is not explicit to tell whether there is improvement, since the rib structure has higher resistivity, that harms the overall RC bandwidth. A further potential optimization is that with better

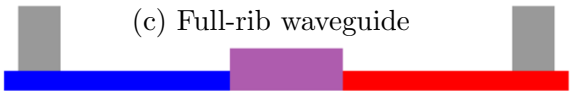

Figure 5.9: Radial section of the electrodes and cavity waveguide, left side is the inner side. Red: heavy P-doping; blue: heavy N-doping; deep purple: either heavy P- or N-doping depends on which section is selected; light purple: effective junction region; gray: metal

optical mode confinement, the electrodes and ribs no longer need to all be located at the inner side of the ring cavity. For example, we can place the anode electrodes outside the ring cavity and the cathode electrodes inside the cavity, which forms the so called full-rib waveguide shown in Fig. 5.9c. Compared to the half-rib waveguide, the extensions from the cavity to the electrodes no longer need to be interleaved, so we can achieve much lower extension resistance and obtain a higher RC bandwidth, as depicted in Fig. 5.10a, the top side view of the full-rib vertical junction structure. Because the electrodes are on both the inner and outer sides, the P and N regions of the cavity can be continuous instead of interleaved as separated islands, forming the full-rib horizontal junction with a different top view shown in Fig. 5.10b. The interface of the P and N regions however, does not necessarily need to be a smooth arc. In case the spoked structure is inherited by the full-rib horizontal junction MRM, we effective achieve a spoked horizontal junction with effectively larger P-N junction area and with better sensitivity to modulation.

The ring modulator's performance varies with the waveguide structure, the junction type, the doping concentration and the DC bias voltage, while the relationship is explicit in none of these factors, since their influence to the cavity decay rate, the refractive index modulation and the RC bandwidth. Thus, a model is developed to evaluate the end-to-end performance of the photonics, where the core optical devices are shown in Fig. 3.1, while we have the grating couplers representing optical loss, and the LNA driving the ring modulator as well. We will assume fixed and reasonable performance metrics for the other electrical or optical blocks, and only changes the ring modulators to compare the performance. As the noise performance is more straight forward, we choose to plot the SNR degradation at the photonic stage, so the total noise figure of the proposed electronic-photonic system will be the sum of this SNR degradation and the noise figure of the LNA.

We assume that the LNA has a power gain of 35 dB and a noise figure of 6 dB. The loss of each grating coupler will be -2 dB and the responsivity of the photodetectors will be 1.0 A/W. The MRMs will have their 3-D models constructed for simulating performance

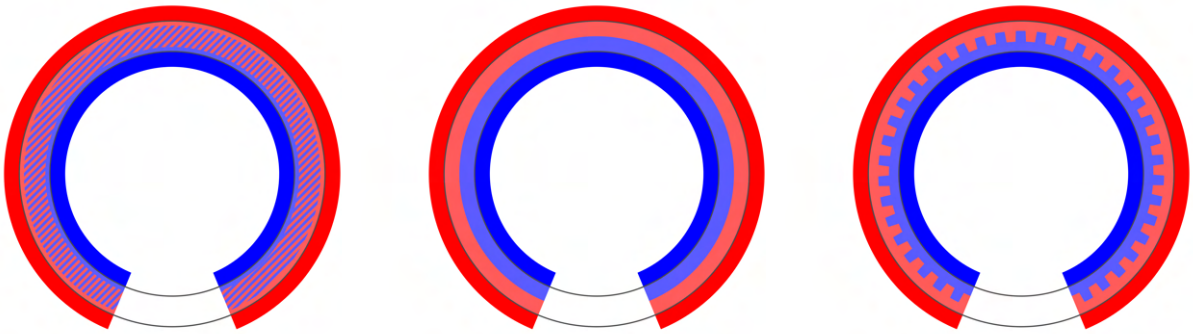

(a) Vertical junction (b) Basic horizontal junction (c) Spoked horizontal junction

Figure 5.10: Top view of full-rib MRMs available in the silicon photonic process platform 45SPCLO. Red: P-doping; blue: N-doping; interleaved stripes: vertical junction. Deep red and blue represent regions farther away from the cavity and closer to the electrodes.

metrics including the cavity decay rate r_o [rad/s], the modulation efficiency of resonance frequency $k_{f,V}$ [GHz/V] and the RC bandwidth [GHz]. And all these parameters will be plugged into the analytic model that calculates the SNR degradation. We choose four of the waveguide-junction structures to present, which are the full-silicon waveguide + vertical junction, the half-rib waveguide + vertical junction, the full-rib waveguide + vertical junction and the full-rib waveguide + basic horizontal junction. For each structure, we assign five levels of DC voltage bias and 7 levels of doping concentration. Both the single-MRMs and dual-MRMs are used to evaluate RF modulation around 70 GHz, with the assumption that the dual-MRMs have the proper resonance split.

The SNR degradation plots of the single-MRMs are presented in Fig. 5.11. In these plots, darker regions represent combination of doping and bias that gives better noise performance, and white blocks either mean that the SNR degradation exceeds the color bar range or we can't get useful data. From the plot we can tell:

- Within one specific ring structure, higher doping concentration seems to give better performance. The reason is that single-MRM's performance does not significantly rely on cavity decay rate which improves the peak gain but harms the bandwidth of an intrinsic optical resonance, so the main contribution is from the resonance frequency modulation $k_{f,V}$ and the RC bandwidth. Intuitively, $k_{f,V}$ is correlated to the sensitivity of the PN junction's depletion width to voltage, and is in another sense, correlated to the small-signal junction capacitance. Higher doping concentration results in smaller depletion width and higher junction capacitance, hence $k_{f,V}$ gets improved. Although the larger junction capacitance harms the RC bandwidth, the higher doping also lowers the resistance of the junction region, so this counteract slows the degradation of the

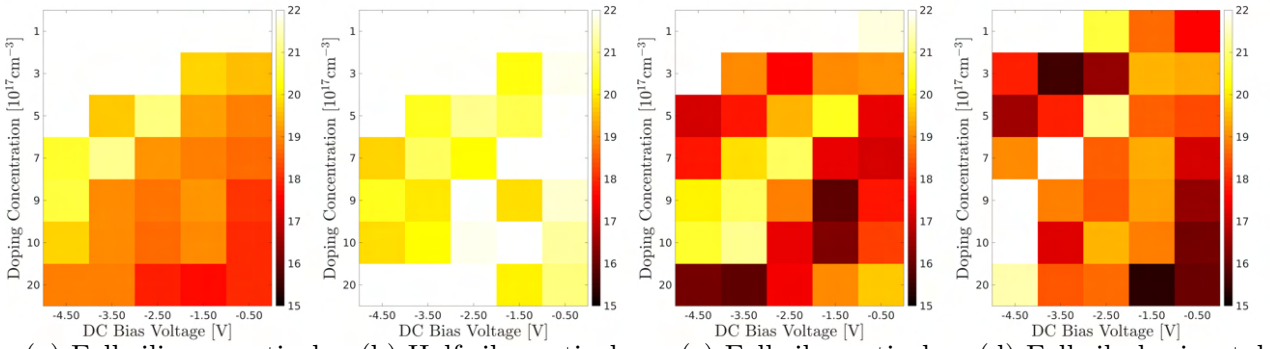

(a) Full-silicon, vertical junction (b) Half-rib, vertical junction (c) Full-rib, vertical junction (d) Full-rib, horizontal junction

Figure 5.11: SNR degradation [dB] of the single-MRM based photonic stage driven by the LNA with 35 dB power gain and 6 dB noise figure.
X-axis: junction DC bias voltage [V]; Y-axis: junction doping concentration [10^{17} cm^{-3}]
Assumptions: $P_{laser} = 1.0$ mW, $\mathcal{R}_{PD} = 1.0$ A/W for photo detector and $\eta_c = -2.0$ dB for grating coupler.

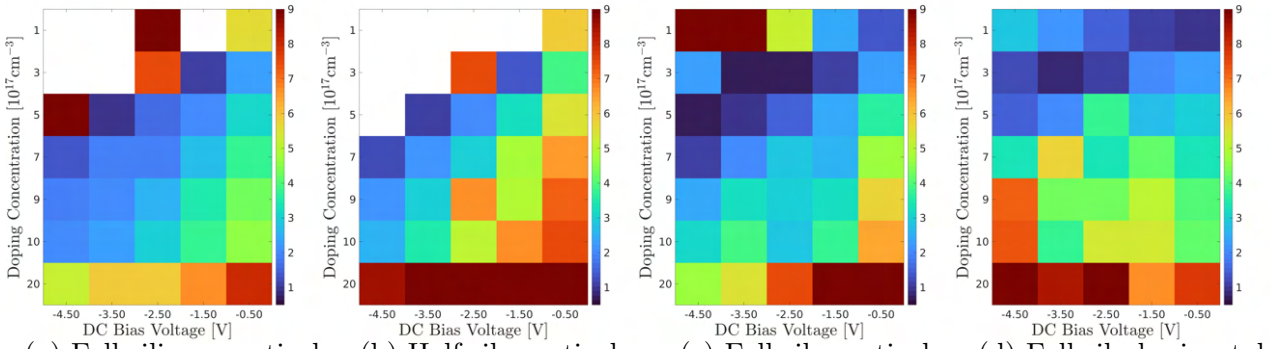

(a) Full-silicon, vertical junction (b) Half-rib, vertical junction (c) Full-rib, vertical junction (d) Full-rib, horizontal junction

Figure 5.12: SNR degradation [dB] of the dual-MRM based photonic stage driven by the LNA with 35 dB power gain and 6 dB noise figure.
X-axis & Y-axis represent the same parameters, and the assumptions are the same.

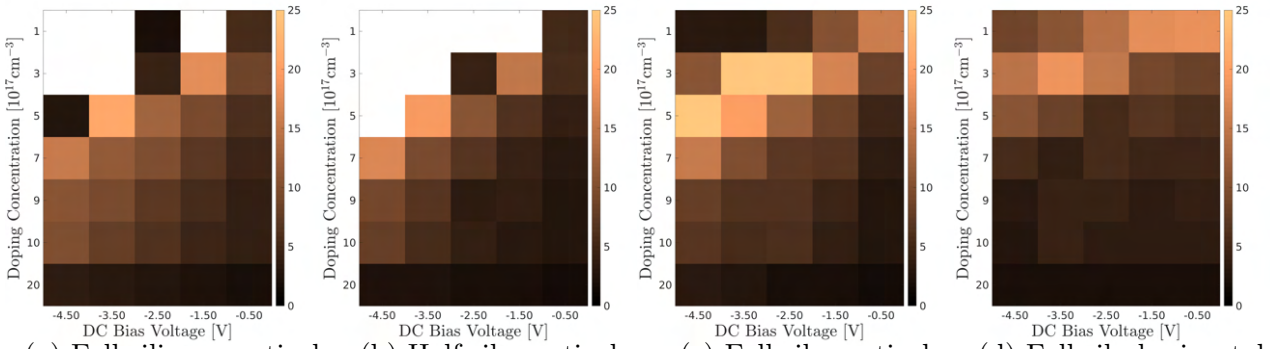

(a) Full-silicon, vertical junction (b) Half-rib, vertical junction (c) Full-rib, vertical junction (d) Full-rib, horizontal junction

Figure 5.13: Noise performance improvement [dB] from single-MRM to dual-MRM. X-axis & Y-axis represent the same parameters, and the assumptions are the same.

RC bandwidth.

- For the single-MRMs with vertical junction structure, the full-rib ones outperform the full-silicon and half-rib ones. The main reason is the improved RC bandwidth, and the change of junction profile also increases the effective junction area that leads to a higher $k_{f,V}$.

- For all the vertical junction MRMs, we will have significant performance penalty when the doping concentration is low and the reverse bias voltage is strong. Since both factors makes the arise of the depletion width, once this width exceeds the thickness of the waveguide, we effectively have almost no modulation to the depletion width that intuitively controls the effective refractive index and the resonance frequency.

As a comparison, Fig. 5.12 shows the SNR degradation of the dual-MRMs, where a color closer to deep blue represents a variant with better performance in terms of noise. From this graph, the fact that full-silicon MRMs slightly outperform half-rib ones still apply. In addition, the plot again confirms that vertical junction MRMs suffer from extremely low doping concentration and strong reverse bias. The (full-rib) MRMs with horizontal junction on the other hand, are not significantly influenced as their maximum junction width can be equal to the width of the cavity waveguide.

However, one big difference is that, unlike single-MRMs with its fundamental performance limitations where decay rate doesn't really help or harm the sideband conversion efficiency or the noise performance at RF/mm-wave frequency, dual-MRMs instead, benefit from lower decay rate as described in Eq. 2.20. A lower decay rate can be realized by having lower doping concentration because the doping makes the photons scatter and decreases their lifetime. Although the lower doping concentration makes the refractive index modulation weaker and partially offsets the overall gain and noise performance, from the figure we can

Table 5.2: MRM varieties driven by LNAs in design V1. Each background color represents one combination of waveguide configuration, junction type and coupler type

Variant #	MRM Type	Cavity Waveguide	Junction Type	Coupler Type	Coupling Strength	Custom Doping
1	Single	Full-silicon	Vertical	Wrapped	Over	
2	Triple	Full-silicon	Vertical	Wrapped	Critical	
3	Triple	Full-silicon	Vertical	Wrapped	Over	
4	Triple	Full-silicon	Interleaved	Wrapped	Over	
5	Dual	Full-rib	Horizontal	Point	Critical	
6	Dual	Full-rib	Horizontal	Point	Over	
7	Triple	Full-rib	Horizontal	Point	Over	
8	Dual	Full-rib	Horizontal	Wrapped	Over	
9	Single	Full-rib	Vertical	Point	Over	
10	Single	Full-rib	Vertical	Point	Over	Yes
11	Dual	Full-rib	Vertical	Point	Over	
12	Triple	Full-rib	Vertical	Point	Critical	
13	Triple	Full-rib	Vertical	Point	Over	
14	Dual	Full-rib	Vertical	Wrapped	Over	
15	Single	Half-rib	Vertical	Point	Critical	
16	Single	Half-rib	Vertical	Point	Critical	Yes
17	Dual	Half-rib	Vertical	Point	Critical	
18	Dual	Half-rib	Vertical	Point	Over	
19	Triple	Half-rib	Vertical	Point	Critical	
20	Triple	Half-rib	Vertical	Point	Over	
21	Dual	Half-rib	Vertical	Wrapped	Over	
22	Triple	Half-rib	Vertical	Wrapped	Over	
23	Single	Half-rib	Interleaved	Point	Critical	
24	Dual	Half-rib	Interleaved	Point	Over	
25	Triple	Half-rib	Interleaved	Point	Over	
26	Dual	Half-rib	Interleaved	Wrapped	Over	
27	Triple	Half-rib	Interleaved	Wrapped	Over	

see that the optimal designs still occur with relatively lower doping and stronger reverse bias, if the depletion width does not exceed the size of the waveguide.

Fig. 5.12 summarizes that with the given performance of the LNA, the other photonic device and the laser source, 3 dB of SNR degradation at the stage of the photonics is not difficult to reach, and together with the LNA's assumed 6 dB noise figure, a total noise figure of 9 dB can be realized for the proposed system. Fig. 5.13 shows the improvement of noise performance by switching from single-MRMs to dual-MRMs with an average range of 10 dB to 25 dB.

From the analysis above, the most promising dual-MRM variants are the ones with full-rib cavity waveguide and are the ones when the doping is light and the reverse bias voltage is decently strong. Within these MRM variants, the vertical junction gives a better performance, but also makes the MRM more prone to the risk of no working in case the doping concentration is lower than expected; on the other hand, the variants of the horizontal junc-

Table 5.3: Standalone MRM varieties (in design V1). Each background color represents one combination of waveguide configuration, junction type and coupler type. Special custom doping is not used here.

Variant #	MRM Type	Cavity Waveguide	Junction Type	Coupler Type	Coupling Strength
1	Single	Full-silicon	Vertical	Wrapped	Critical
2	Single	Full-silicon	Interleaved	Wrapped	Over
3	Triple	Full-silicon	Interleaved	Wrapped	Critical
4	Single	Full-silicon	Interleaved	Wrapped	Over
5	Single	Full-rib	Horizontal	Point	Critical
6	Single	Full-rib	Horizontal	Point	Over
7	Triple	Full-rib	Horizontal	Point	Critical
8	Single	Full-rib	Horizontal	Wrapped	Over
9	Dual	Full-rib	Horizontal	Wrapped	Critical
10	Triple	Full-rib	Horizontal	Wrapped	Over
11	Single	Full-rib	Vertical	Point	Critical
12	Dual	Full-rib	Vertical	Point	Critical
13	Single	Full-rib	Vertical	Wrapped	Over
14	Dual	Full-rib	Vertical	Wrapped	Critical
15	Triple	Full-rib	Vertical	Wrapped	Over
16	Single	Half-rib	Vertical	Wrapped	Over
17	Dual	Half-rib	Vertical	Wrapped	Critical
18	Triple	Half-rib	Vertical	Wrapped	Critical
19	Dual	Half-rib	Interleaved	Point	Critical
20	Triple	Half-rib	Interleaved	Point	Critical
21	Single	Half-rib	Interleaved	Wrapped	Over
22	Dual	Half-rib	Interleaved	Wrapped	Critical

tion get a decently good balance between the gain & noise performance and the robustness to process variation.

For verification purposes, design V1 still implemented the dual- or triple-MRM variants with sub-optimal performance for verification purposes, plus the single-MRM variants for comparison. The variants driven by LNA are listed in Table 5.2. There are also standalone devices that can be measured without being driven by the LNA, and these variants are shown in Table 5.3. All the full-rib, horizontal junction MRMs in design V1 are using the basic horizontal junctions. In design V2, we seek to evaluate the ring variants the performance of which needs to be both high and robust and with wide range of tunability, thus all the ring variants are the full-rib horizontal junction triple-MRMs, where half of them have the basic horizontal junction and the rest half have the spoked horizontal junction. The remaining varying design parameter is the physical gap spacing between the rings, or between the ring and the bus waveguide, which aims at achieving the optimal external coupling rate r_e. To

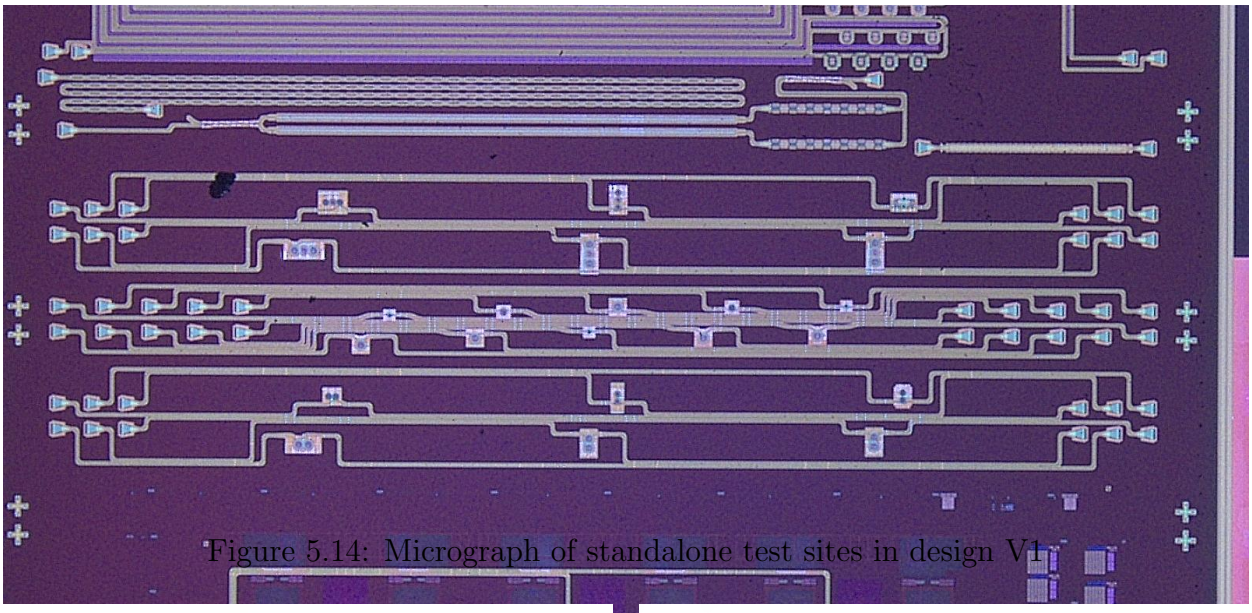

Figure 5.14: Micrograph of standalone test sites in design V1

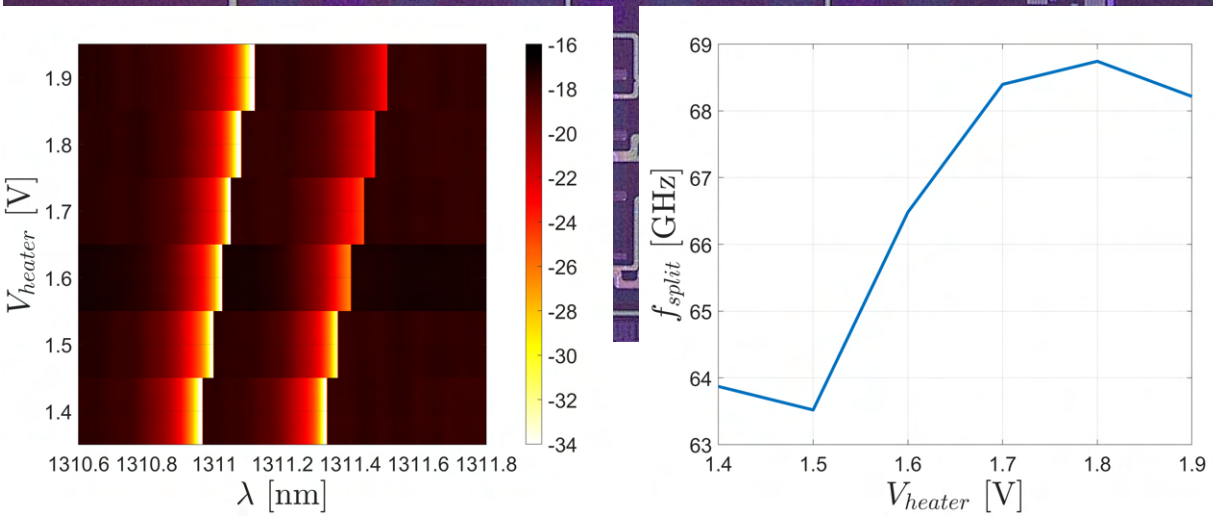

(a) Wavelength response of the dual-MRM with different heater voltages

(b) Frequency split of the two supermodes with different heater voltages

Figure 5.15: Resonance detuning of the dual-MRM

operate with higher incident laser power without significant performance degradation which occurred in the design mentioned in the previous chapter, all the triple-MRMs designed within this process platform have their central cavity doped and extended to electrodes for carrier sweep-out.

5.4 Measurement Results

As listed in Table 5.3, the standalone MRM testsite taped-out with design V1 has 10 single-MRMs, 6 dual-MRMs and 6 triple-MRMs, and its micrograph is shown in Fig. 5.14. Though not showing in the figure, there are rows of probe pads close to the MRMs. The probe pads

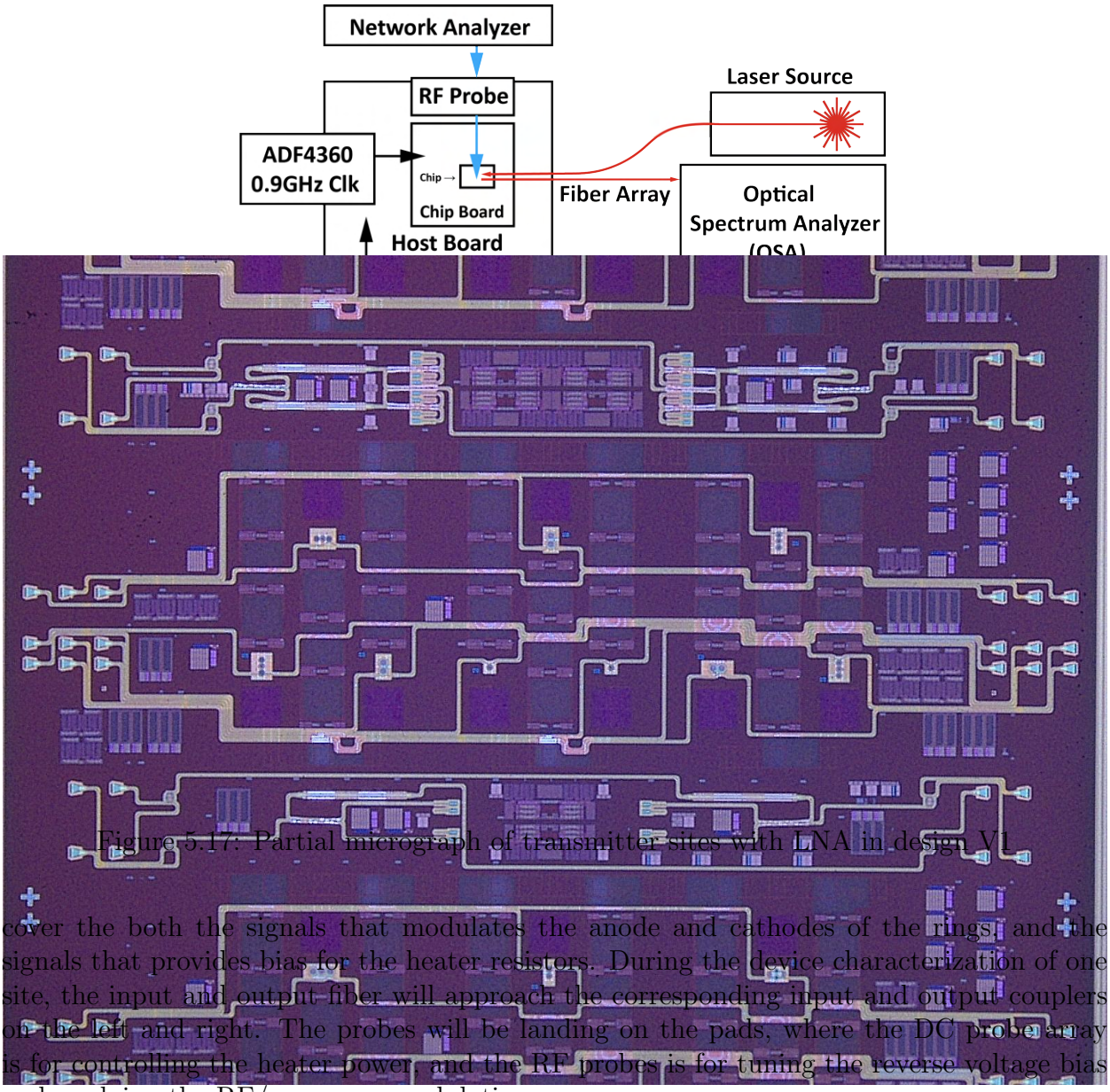

Figure 5.17: Partial micrograph of transmitter sites with LNA in design V1

cover the both the signals that modulates the anode and cathodes of the rings, and the signals that provides bias for the heater resistors. During the device characterization of one site, the input and output fiber will approach the corresponding input and output couplers on the left and right. The probes will be landing on the pads, where the DC probe array is for controlling the heater power, and the RF probes is for tuning the reverse voltage bias and applying the RF/mm-wave modulation.

Fig. 5.15 illustrates the experiment on the tunability of a standalone dual-MRM test site. During the measurement, a 0 V voltage is applied to one of the heaters, and the other heater will be swept and the optical response of the MRM versus laser wavelength/frequency will be recorded. As shown in Fig. 5.15a, this tuning shifts both supermode resonance to a higher wavelength like what occurred for the triple-MRM in the previous chapter. The tuning of frequency split itself seems not significant, by Fig. 5.15b does present and confirms the tunability. The tuning limitation is mainly on the lower bound at around 60 GHz by the original split of the two non-detuned, mutually coupled cavities. The measurement for standalone devices is still ongoing, where the next steps include but are not limited to the

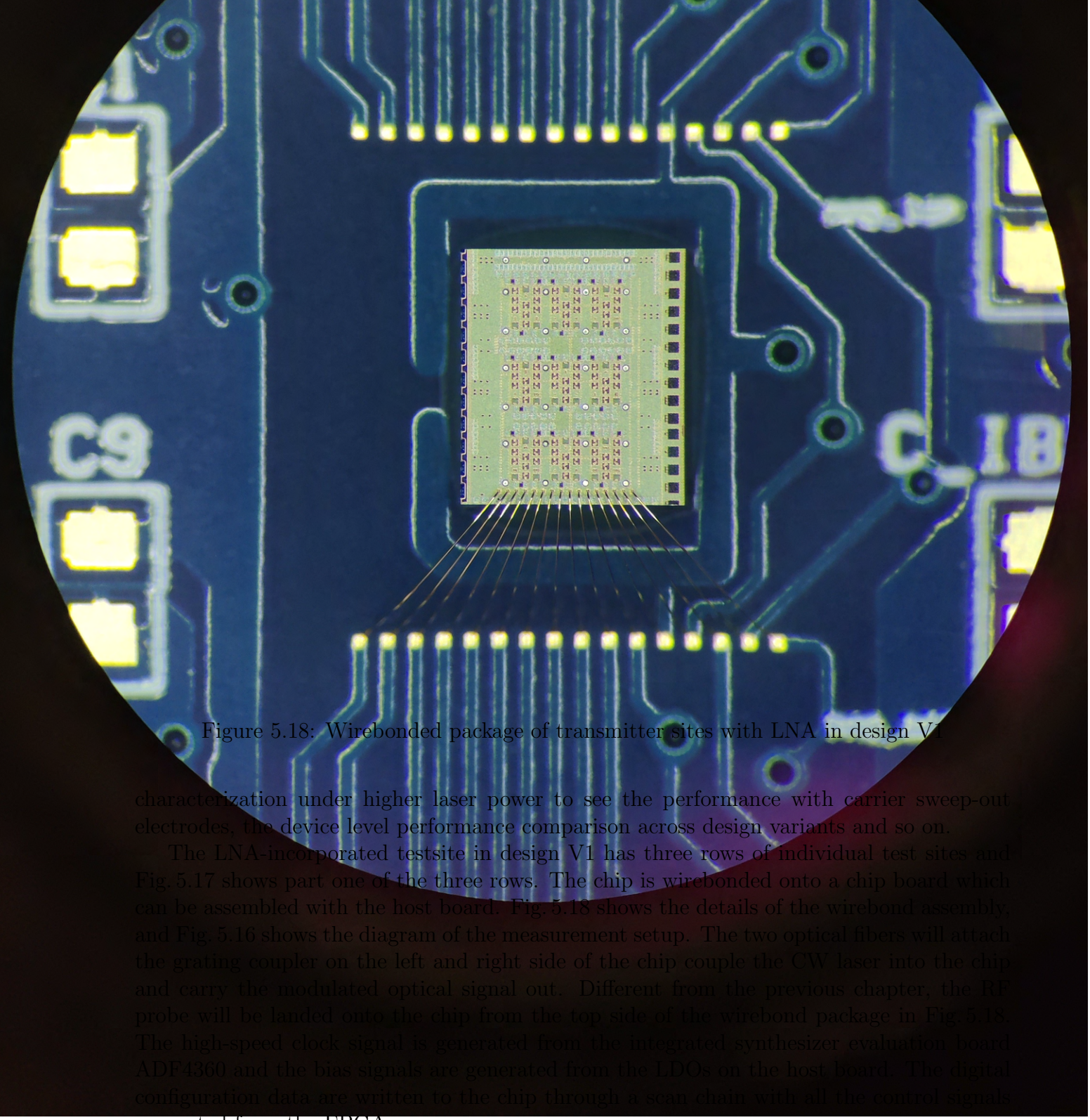

Figure 5.18: Wirebonded package of transmitter sites with LNA in design V1

characterization under higher laser power to see the performance with carrier sweep-out electrodes, the device level performance comparison across design variants and so on.

The LNA-incorporated testsite in design V1 has three rows of individual test sites and Fig. 5.17 shows part one of the three rows. The chip is wirebonded onto a chip board which can be assembled with the host board. Fig. 5.18 shows the details of the wirebond assembly, and Fig. 5.16 shows the diagram of the measurement setup. The two optical fibers will attach the grating coupler on the left and right side of the chip couple the CW laser into the chip and carry the modulated optical signal out. Different from the previous chapter, the RF probe will be landed onto the chip from the top side of the wirebond package in Fig. 5.18. The high-speed clock signal is generated from the integrated synthesizer evaluation board ADF4360 and the bias signals are generated from the LDOs on the host board. The digital configuration data are written to the chip through a scan chain with all the control signals generated from the FPGA.

The measurement of design V1 is in progress. Some of the MRM variants have a frequency split of higher than 70 GHz with some even reaching 80 GHz. Although this new platform has more optical device features, the influence from the process variation is still challenging for the designers. The full-silicon waveguide, although not the best choice in terms of performance, has smaller variation in terms of its thickness. The rib waveguide available in this new process generation has much larger shallow etch thickness variation. This thickness might significantly change the coupling coefficient between two cavities, and

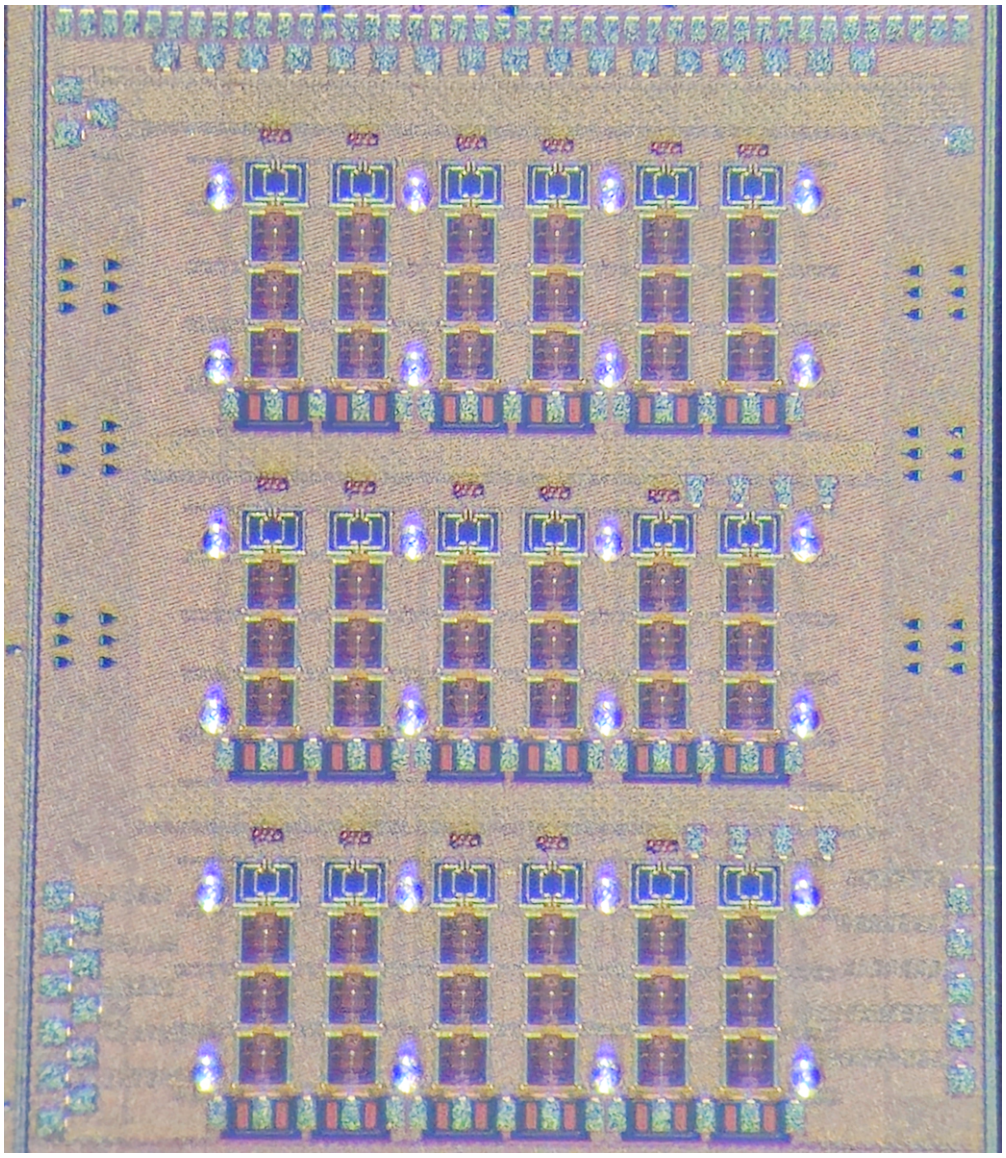

Figure 5.19: Micrograph of design V2

can even introduce the coupling of a higher order mode. So for future designs, the process variation should also be taken into account for device and system level optimization [67].

Meanwhile, there are still plenty of dual- and triple-MRMs with a proper resonance split that can be aligned with the LNA, and we are attempting to do the alignment for now.

The micrograph of design V2 is shown in Fig. 5.19. At present, the wafer with design V2 has just been diced. The package design including the chip board and the host board has been finished, so the next step is to send for package once the bare dies get delivered.

5.5 Chapter Summary

The chapter further develops the transmitter array element design within a new process platform optimized for silicon photonic devices. Optimization in terms of wide band input matching, inter-stage matching are made targeting a more practical demonstration of the proposed architecture.

The device level characterization is in progress as well as the characterization of the LNA modulator sites. From the currently obtained device level measurement results, the dual-MRM also presents decent tuning capability and the sideband can be generated. Whether to use the dual-MRM or the triple-MRM highly depends on the scenario of the application, for example whether we prefer a tunable carrier frequency at the system level, and on the process variation control of the device as well. For this newly developed silicon photonic process platform, the process variation might still be a non-trivial issue, and it needs to be addressed either by the foundry or by the designer.

Chapter 6

Receiver Array Element Design

This chapter presents the design of the receiver (Rx) element that accommodates the proposed architecture featuring wavelength division multiplexing. The design is fabricated in the silicon photonic process platform.

6.1 Photonic Front-end Unit

Eq. 3.7 reveals that if only there is only one link channel in the fiber, i.e. we will only see one pair of spectral components that are close to each other so that the demodulated photo current represents the low-frequency baseband signal, then there is no imperative need for a filter, as all the other undesired signals will be close to or beyond the carrier frequency that can be filtered out with additional analog or digital filters in the electrical domain. With the proposed wavelength division multiplexing however, additional design considerations need to be taken into account. Fig. 6.1a presents an example of the spectral components where four proposed photonic links share one optical fiber. Without any optical band selection filters, all the sidebands and reference tones will reach this specific photodetector pair, so that the demodulated photo current suffers from the baseband signals aliasing of these four link channels. While this aliasing might draw some interest as a beamforming computation can happen here, it also raises concerns in terms of factors like the dynamic range of the following electrical front-end. Thus, we choose to have one electrical front-end for each optical link channel, and conduct all the beamforming in the electrical domain, as the area and power budget on the receiver side is decently high. One solution to avoid the combination of different link channels during demodulation is illustrated in Fig. 6.1b. For the two optical fibers carrying four link channels, there are eight ring filters instantiated, with four of them on the sideband side and the rest four on the reference side. For a specific photonic front-end depicted in this figure, the two ring filters selects out one individual sideband and reference tone and passes the rest of the optical signals to the next photonic front-end. The selected sideband pairs with the corresponding reference tone and combine through the coupler. With this architecture, the demodulated photo current only contains the selected

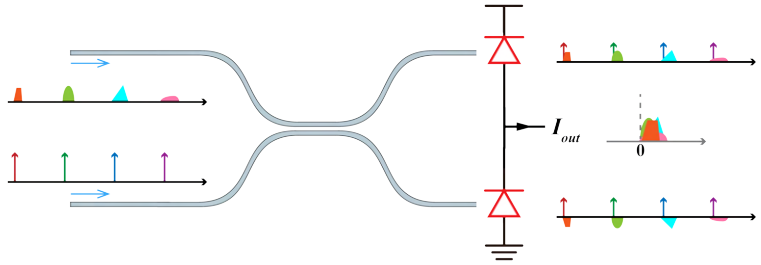

(a) With no optical filters

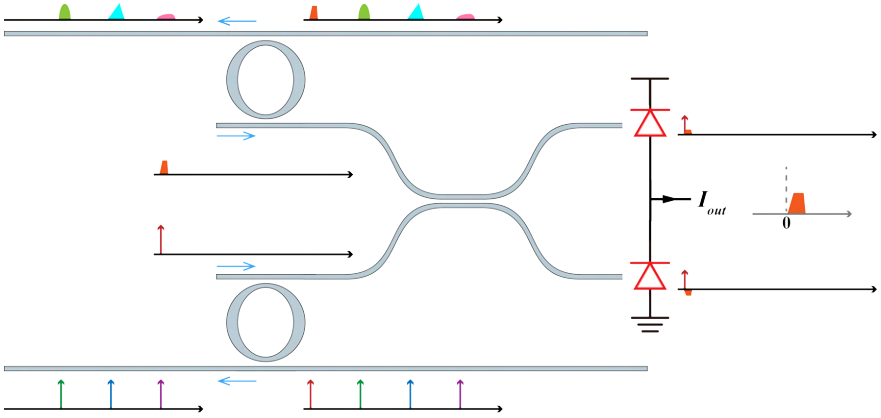

(b) With optical band-selection filters

Figure 6.1: Spectral diagram of a receiver element in a WDM link

link channel ideally, so that the aliasing between different link channels will be negligible, and the optical signals of each link channel will be processed by a unique electrical front-end which benefits both the conversion gain and the noise figure. This design makes use of the ring that consists of the single-mode coupling regions and the adiabatic bending regions [68]. With doping region outside the cavity and better optical mode confinement due to the adiabatic waveguide, this ring exhibits lower insertion loss in the optical pass band, which makes it a perfect static tunable filter.

We implemented two types of receiver elements in this design, and their photonic front-end diagram with device implementation and waveguide routing depicted in Fig. 6.2, described as:

- Fig. 6.2a shows the photonic front-end that can handle amplitude shift-keying (ASK) demodulation. The two optical input signals first go through the adiabatic ring filters,

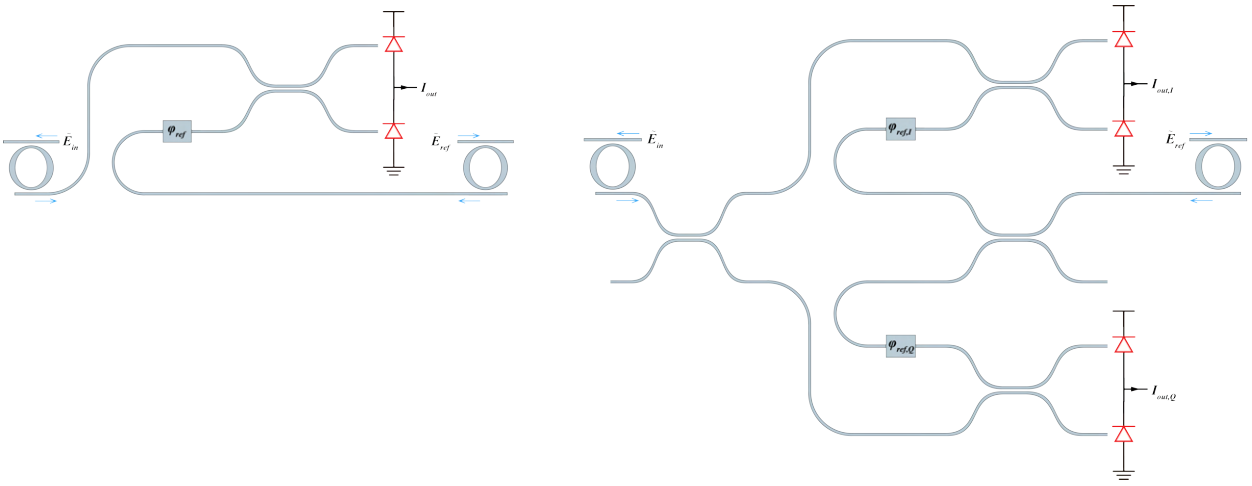

(a) With one demodulation channel (b) With I/Q channels

Figure 6.2: Photonic front-end implementation for the proposed receiver array element

with the selected band propagating out from the drop port and the unwanted bands passes via the through port to the next ring filter. Suggested by Eq. 3.8, to maximize the conversion gain, the relative phase between the sideband and the reference need to be adjusted by tuning φ_{ref} to a specific value before combining through the 2×2-coupler. There will be one branch of output current flowing from the balanced photodetector pair to the receiver analog front-end (RXAFE).

- Fig. 6.2b shows the front-end that is able to perform complex demodulation which is suitable to demodulate signals from quadrature amplitude modulation (QAM). The difference is that the selected sideband and reference tone will propagate into two additional 2×2-couplers working as 50%-50% optical power splitters. By assigning the correct coupler port to the input, the split output signals should be in-phase. Then the split reference tones individually go through two thermally controlled phase shifters before combining with the split sideband signals. The two branches of in-phase sidebands and the two quadrature shifted reference tones then combine through two identical couplers and generates four combinations, which reaches the balanced PD pairs and get finally converted to the I-path and Q-path photo current. Regardless of the absolute values of $\varphi_{ref,I}$ and $\varphi_{ref,Q}$, once the phase difference of them are guaranteed to be $\pi/2$, the I and Q path baseband data can be fully recovered by the back-end post processing.

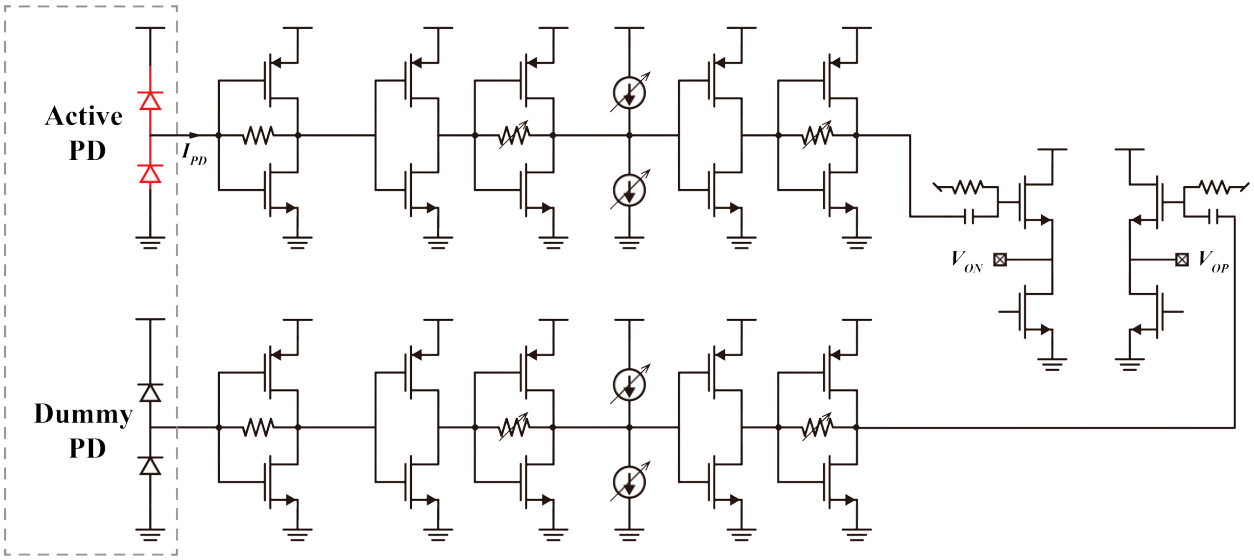

Figure 6.3: Schematic of the receiver's analog front-end

6.2 Electronic Front-end Unit

The schematic of the analog front-end that takes one branch of photo current is shown in Fig. 6.3. The photo current is first converted to the voltage signal by the inverted-based transimpedance amplifier (TIA). The voltage signals is then amplified by the cascaded inverter-based Cherry-Hooper stages. The Cherry-Hooper stage has its gain controlled by the resistor digital-to-analog converter (DAC) to accommodate varied amplitude levels of the input photo current. In between the two Cherry-Hooper stages, a pair of current DACs are implemented as well to cancel the offset voltage caused by the process variation to guarantees that the proper DC operating point of the amplifier chain.

The amplifier chain mentioned above is a single ended design since the photonic front-end only generates on branch of photo current. In order to suppress the influence from factors like power supply noise and crosstalks from adjacent circuit blocks, a duplicate of the amplifier chain is placed with the dummy PD as well, given the fact that the undesired factors mainly exert the same gain to the signal path and the dummy path, this pseudo-differential pair has better power supply rejection ratio (PSRR) and is less sensitive to the environment interference.

To achieve higher linearity and to match the output resistance to $50\,\Omega$, the output buffer is a common-drain source-follower. As the DC output voltage of the previous Cherry-Hooper will be around half of the power supply which is lower than the desired DC input voltage of the common-drain transistor. An AC-coupling bias network is hence used to assign proper bias point for the source-following aiming at a larger output swing. Because we have very limited

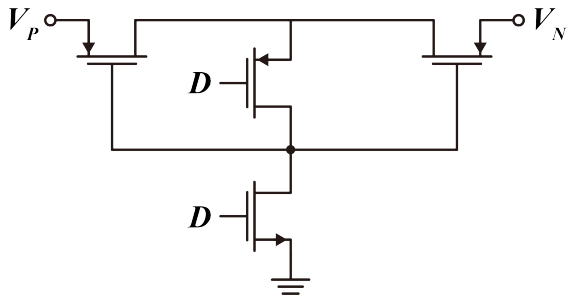

Figure 6.4: Schematic of the configurable pseudo resistor

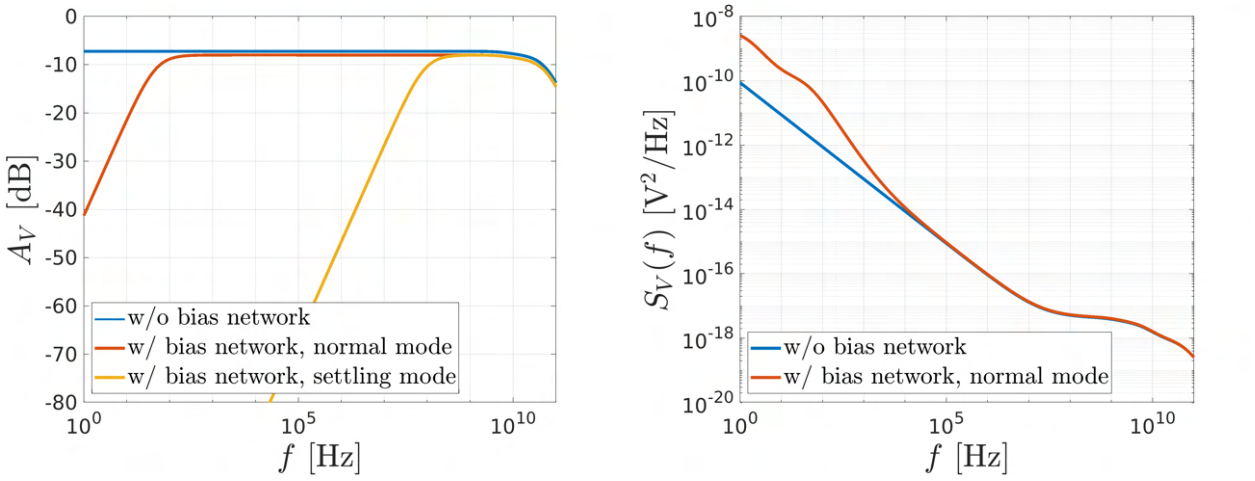

(a) Frequency response

(b) PSD of output noise voltage

Figure 6.5: Simulated frequency response and noise of the source follower

access to a large on-chip passive resistors or capacitors while such AC-coupling network requires a fairly low high-pass corner frequency, we utilize the transistor to build a high-resistance configurable pseudoresistor, illustrated in Fig. 6.4.

The pseudoresistor consists of two PMOS transistors as the core that provide the bias voltage closer to the power supply, and it has the additional NMOS / PMOS switches for the fast-settling mode configuration. In the normal high-resistance mode, the digital control signal D is low so that the NMOS switch is off and the PMOS switch is on, so that the gates of the core PMOS transistors are connected to the middle node to form a symmetric pseudoresistor [69–71]. In the fast settling mode, the NMOS switch is on and the PMOS switch is off, so the core PMOS transistors are on with their gates pulled down to the ground, this creates a moderate switch resistance path between V_P and V_N so that the bias voltage can settle within a shorter time period.

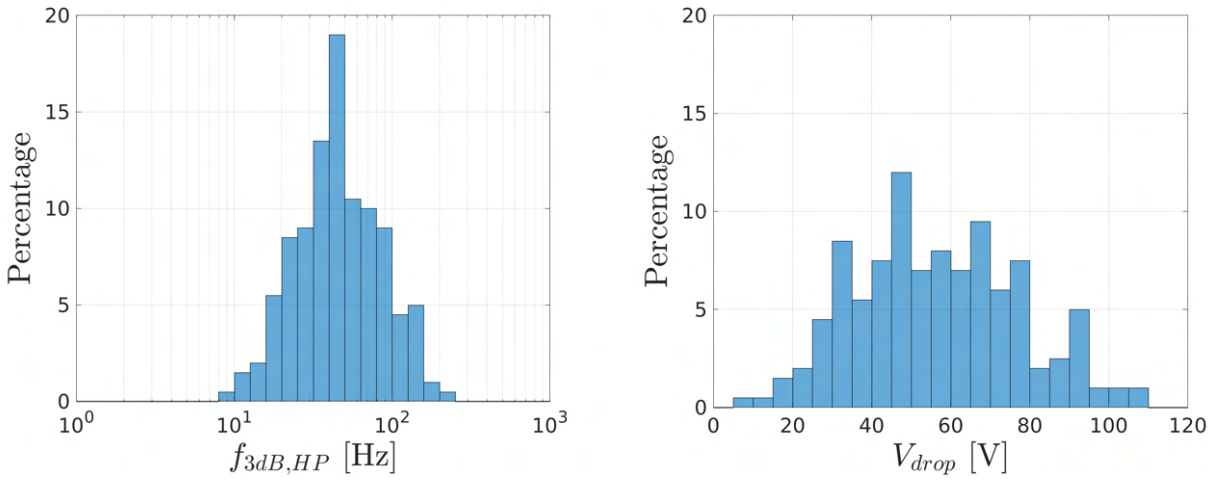

(a) High-pass corner frequency

(b) Voltage drop

Figure 6.6: Histogram of the pseudoresistor's performance metrics from Monte-Carlo simulation

The designed AC-coupling network consists of the configurable pseudoresistor and a 400 fF capacitor. Fig. 6.5a plots the frequency response of the source follower core, together with that of the source follower with the coupling network with two resistance configurations. In all the three scenarios, the DC operating point of the common-gate transistors is close to the supply voltage. The mid-band voltage gain of the source follower core is around -7.3 dB, with -6 dB from the voltage divider due to the 50 Ω impedance matching. With the input bias network, it has an additional gain degradation around 0.7 dB decrease due to the input capacitance of the source follower core. The bandwidth of the source follower in the normal mode is around 50 GHz, and the high-pass corner frequency is around 48 Hz, which fulfills the design constraints. In the fast settling mode, the corner high-pass corner frequency is above 50 MHz. In this case, the DC operating point of the bias network can settles a million times faster, approximately within 20 ns.

The use of the pseudoresistor introduces additional noise that mainly presents around and below the high-pass corner frequency, as indicated by the power spectral density (PSD) of the source follower's output noise voltage plotted in Fig. 6.5b. The root mean-square (RMS) voltage integrated from 1 Hz to 50 GHz is 250 μV for the source follower core and the pseudoresistor-based network adds around 25% noise power to it, resulting in an increased RMS noise voltage of 280 μV and referring to the input as 703 μV.

Utilizing the pseudoresistor also makes the design more prone to process variations, including the exact value of the resistance that influences the high-pass cut-off frequency and the voltage drop across the resistor due to the leakage. To address the potential drawbacks, all the transistors in the pseudoresistor plus the input transistor of the source follower core

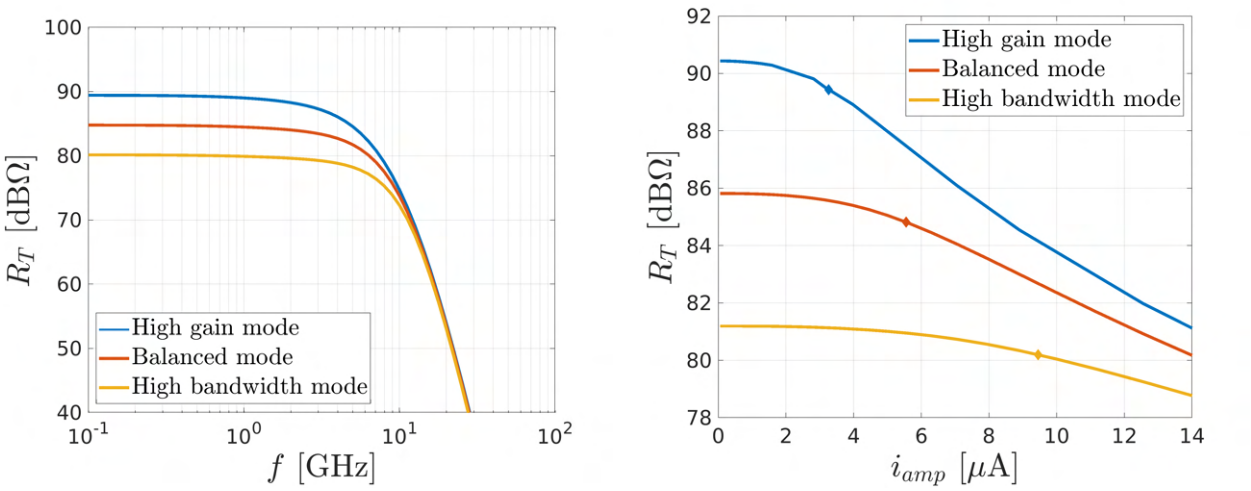

(a) Frequency response

(b) Gain compression

Figure 6.7: Transimpedance gain R_T of the RXAFE

are thick gate devices, and stacked transistors are used for the NMOS switch, so that the gate leakage current is negligible. Monte-Carlo simulations are run to verify the 3 dB high-pass cutoff frequency and the voltage drop of the pseudoresistor when it is connected with the source follower, and Fig. 6.6 presents the results. The maximum high-pass 3 dB corner frequency observed is around 250 Hz and the maximum voltage drop is 108 mV among 200 Monte-Carlo samples, showing the robustness of the entire source follower.

The resistor DACs implemented in the Cherry-Hooper stages make the gain and bandwidth of the RXAFE configurable. In this design there are three modes in which we are targeting a higher gain, a higher bandwidth, and a balanced performance of gain and bandwidth, respectively. From the post-extraction simulation, the mid-band gains of these three configurations approximately range from 80 dB to 90 dB accommodating different levels of input photo current amplitudes, and the 3 dB bandwidths range from 6.3 GHz to 3.6 GHz, as plotted in Fig. 6.7a.

Figure. 6.7b shows the degradation of the transimpedance gain of the fundamental tone with increasing input amplitude. The markers label the 1 dB gain compression points where the input current amplitudes of the three modes are 3.25 μA, 5.55 μA and 9.45 μA, respectively, and the corresponding output voltage amplitudes are all around 96 mV. Because of the similar output amplitudes of the compression points and the fact that the 1 dB gain compression input for the TIA is as large as 650 μA, we get to know that the linearity of the designed RXAFE is output limited contributed by the Cherry-Hooper stages. This design is mainly for verifying the gain and noise performance of the proposed full link rather than realizing high linearity, so the Cherry-Hooper stages are implemented to have larger output amplitude purely for measurement purposes. Therefore, in case the additional amplifier

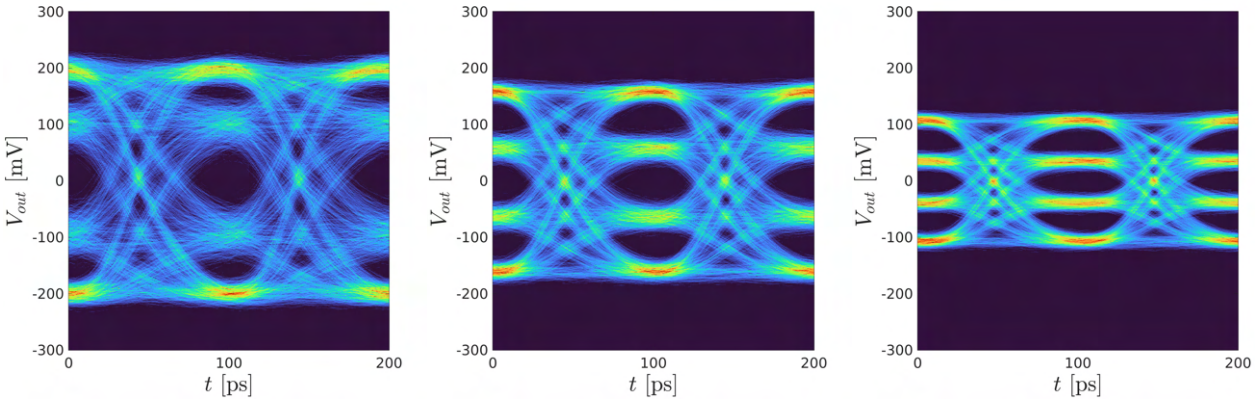

(a) High gain mode (b) Balanced mode (c) High bandwidth mode

Figure 6.8: Eye diagrams from the transient noise simulation

stages and the source follower are replaced by the analog to digital converter in a practical system, the receiver can achieve much higher linearity.

Table 6.1: Performance Summary of the Receiver Analog Front-end

Gain Configuration	High Gain	Balanced	High Speed
Gain	89.4 dBΩ	84.8 dBΩ	80.2 dBΩ
Bandwidth	3.6 GHz	4.9 GHz	6.3 GHz
Input amplitude at 1 dB Compression Point	3.25 μA	5.55 μA	9.45 μA
Output amplitude at 1 dB Compression Point	96.4 mV	96.6 mV	96.7 mV
Input Referred Noise, RMS within 2 times bandwidth	0.88 μA	1.03 μA	1.23 μA
Input Referred Noise, Spot at Midband	1.59 $\times 10^{-22}$ A^2/Hz		
Equivalent Shot Noise Current	244 μA		
Power	13.6 mW		

Frequency domain noise simulations show that the total input referred RMS noise current ranges from 0.88 μA to 1.23 μA depending on the gain configuration. To further verify the noise performance, transient noise simulations are done with all the three gain configurations. The input current is the PAM4 signal encoded by the pseudo-random sequence with a bit rate of 20 Gbit/s (i.e. symbol rate of 10 GBaud/s) and a peak-to-peak swing of 20 μA. The intensity assisted eye diagrams with 10^4 symbols are shown in Fig. 6.8 where all the eyes are

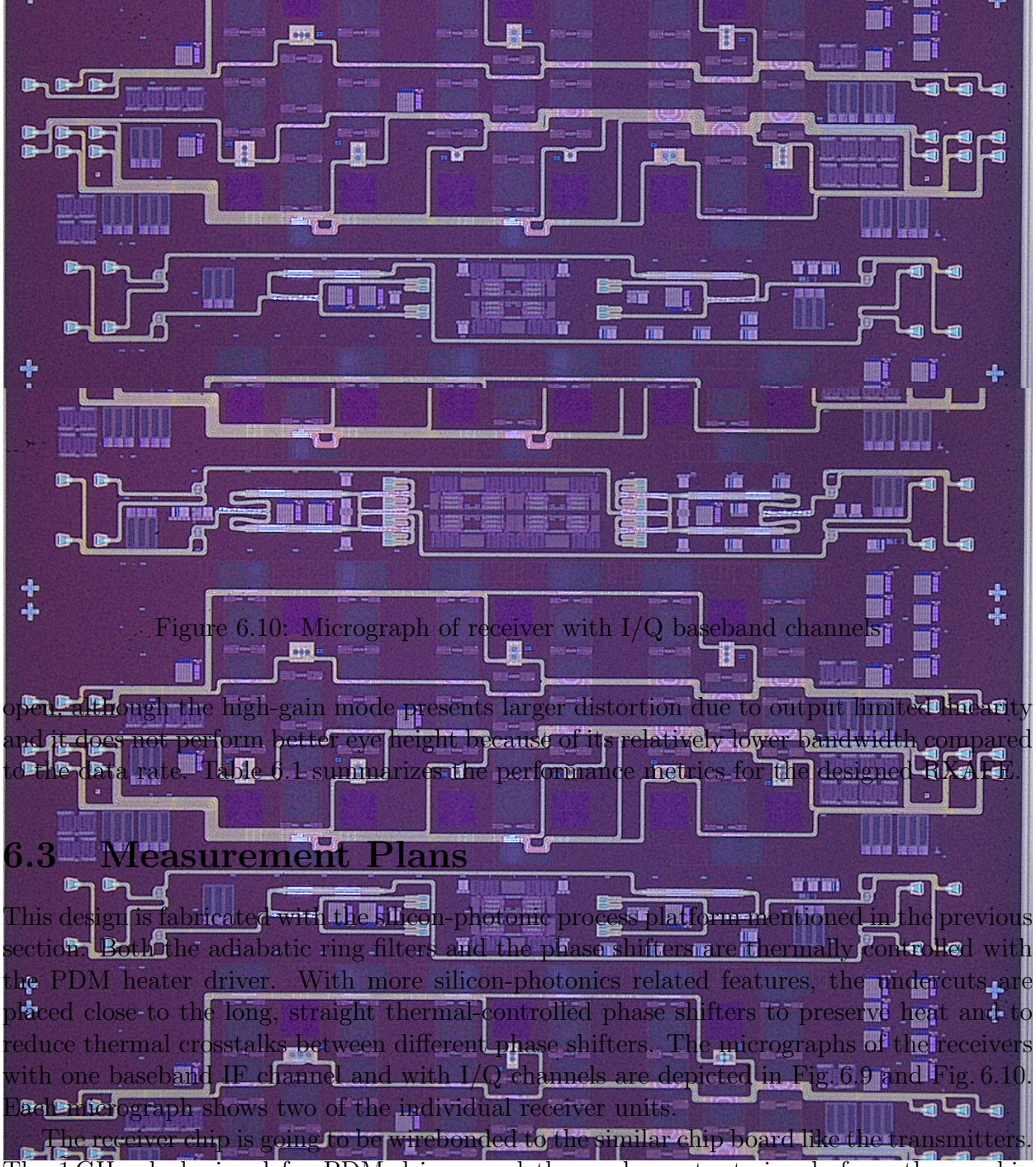

Figure 6.10: Micrograph of receiver with I/Q baseband channels.

open, although the high-gain mode presents larger distortion due to output limited linearity and it does not perform better eye height because of its relatively lower bandwidth compared to the data rate. Table 6.1 summarizes the performance metrics for the designed RXAFE.

6.3 Measurement Plans

This design is fabricated with the silicon-photonic process platform mentioned in the previous section. Both the adiabatic ring filters and the phase shifters are thermally controlled with the PDM heater driver. With more silicon-photonics related features, the undercuts are placed close to the long, straight thermal-controlled phase shifters to preserve heat and to reduce thermal crosstalks between different phase shifters. The micrographs of the receivers with one baseband IF channel and with I/Q channels are depicted in Fig. 6.9 and Fig. 6.10. Each micrograph shows two of the individual receiver units.

The receiver chip is going to be wirebonded to the similar chip board like the transmitters. The 1 GHz clock signal for PDM drivers and the analog output signals from the on-chip source-followers arrives at or depart the chip board through the SMA connectors, and all the other low-to-moderate speed scan chain or static bias signals are connected to the host board through, which is similar to the transmitter packaging design.

The diagram of the planning measurement setup is shown in Fig. 6.11. The diagram only shows the signal path of one single optical channel, and it consists of the following essential component and instruments for the desired evaluation:

- The arbitrary waveform generator (AWG) generates the I-path and Q-path baseband IF signals as a reference. QAM signals will be used in this case as the implemented electronic-photonic system can handle it. On the other hand, the signals generator is for providing a high-frequency LO signal.

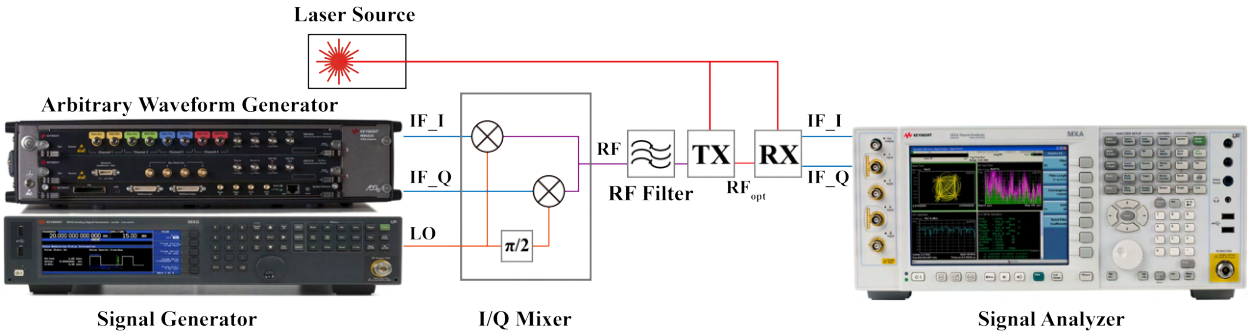

Figure 6.11: Diagram of the receiver's measurement setup

- The commercial I/Q complex up-convert mixer. It takes the in-phase and the quadrature of the LO signal and multiply them with the I-path and Q-path IF signals respectively. The up-converted RF signals are them combined and form the final complex modulated RF signals.

- the commercial RF filter is for creating the representative RF/mm-wave signals. To emulate the RF signals with image rejection, the output of the AWG itself already has a carrier frequency $f_{LO,AWG}$. Given the LO frequency provided by the signal generator $f_{LO,siggen}$, the output of the mixer has two sidebands at $f_{LO,siggen} \pm f_{LO,AWG}$. The RF filter is to select out the sideband at $f_{LO,siggen} + f_{LO,AWG}$, which represents the carrier frequency of the emulated RF signal source.

- The laser source provides two laser tones for each optical link channel. One tone is the reference tone getting feed-forwarded directly into the receiver chip and the other is propagated to the transmitter to get modulated.

- The signal analyzer obtains the demodulated analog IF signals of the I-path and the Q-path, and use them to recover the constellation plot.

The diagram assumes that the receiver with I/Q channels are being evaluated. For the receiver with only one demodulation channel, the AWG only generates I-path signal and the I/Q mixer will be replaced by the basic mixer. However, we need to tune the phase shifter on the RX chip carefully in order to maximize the gain.

The measurement is planned to be conducted in three parts. The first part is to evaluate its performance in a regular coherent silicon photonic high-speed serial link, as the receiver's architecture can also handle basic BPSK or QPSK demodulation in case the adiabatic ring filter aligns with the single laser tone. In this scenario, the signal generator and the mixer will not be used and the output of the AWG will be directly fed to the TX. The TX in this step consists of commercial components like Mach-Zehnder Interferometers for a more stabilized operation as a reference. Since a regular coherent link only used one laser tone, such first-step measurement reveals the performance with nearly-perfect laser coherence.

The second part of the measurement is to activate the signal generator and plug in the mixer, then provide the two laser tones while the TX is still the commercial plug-in blocks. This part introduces the non-ideal correlation between the two laser tones so that the results present how does the system level performance degrades. The last part is to replace the TX with the ones that we designed illustrated in the previous chapters, which evaluates the overall performance of the monolithic design.

6.4 Chapter Summary

The chapter implements the receiver array element design to mainly to evaluate the electrical-to-electrical link performance. The photonic front-end performs optical domain band selection and is able to demodulate the optical signal processed by the I/Q modulation. The analog front-end achieves a configurable gain ranging from about 80 dBΩ to 90 dBΩ, with its input referred noise current equivalent to the noise generated by 244 μA diode current which is much smaller than the actual DC photo current. The linearity of the full receiver is somehow limited, but mainly because of the amplifying stages for measurement purposes, and can be significantly improved.

Chapter 7

Conclusion

7.1 Summary

The major contribution from the thesis are summarized as follows:

- This work proposes a electronic-photonic system architecture to address the design challenge of massive-MIMO millimeter-wave systems. With the two-tone laser playing the role of the optical LO, it first avoids the burden of electrical domain LO distribution. By utilizing energy efficient photonic links that are monolithically integrated with the circuits, the quantization and post processing blocks that bring more design constraints can be implemented remotely on an individual site where the power and area budgets are more sufficient.

- To conduct the electro-optical conversion with high efficiency and with desired frequency response, this work employs the multi-cavity MRM including dual- and triple-MRM, where the sideband conversion efficiency is comparable to single-MRM at baseband frequency range.

- From the system level of view, this work develops the model that maps the optical performance metrics to the end-to-end metrics, including the conversion gain/transconductance, noise figure, IIP_3 and so on, that are in the framework of wireless communication systems.

- To prove the feasibility of the proposed architecture, several designs are implemented in two generations of process platforms that enable monolithic integration. The design framework and methodology are illustrated in this work. The measurement results present the proof of concept, and discover the additional design considerations for future designs.

Overall, this research work consists of many challenging tasks: both the process platforms and the photonic devices are relatively new with a large design space to explore and more

performance metrics to characterize; there are not many testing points we can add as the electrical signals operates at high frequency. Nevertheless, our design is finally proved to work as expected, and the development of monolithic silicon photonic process gives us the confidence that the photonic link for massive-MIMO applications will attract more attentions and become much more practical.

7.2 Future Work

This work focuses on the photonic transmitter and receiver element. For the entire system, the following aspects are also non-trivial tasks which either needs to be properly addressed, or shows the potentials of a breakthrough:

- **Laser Source:** The two laser tones works as the LO, so just like the electrical LO, a low phase noise is required. This raises requirement for the coherence of the two laser tones from the laser source.
- **MRM Locking:** The resonance frequency of the MRM is also sensitive to parameters like the temperature or the mechanical stress. It is important to lock it to the laser tone so that a stable behavior can be achieved. Such locking requires both front-end level and algorithm level optimizations.
- **Beamforming:** The proposed architecture leaves the beamforming operations in the electrical domain. It would be even more attractive if this beamforming can be conducted in the optical domain.

Bibliography

[1] Emily Naviasky et al. "A 71-to-86-GHz 16-Element by 16-Beam Multi-User Beamforming Integrated Receiver Sub-Array for Massive MIMO". In: *IEEE Journal of Solid-State Circuits* 56.12 (2021), pp. 3811–3826.

[2] Ruocheng Wang et al. "A Monolithically Integrated Electronic-Photonic Front-end Utilizing Micro-ring Modulators for Large-Scale mm-wave Sensing". In: *ESSCIRC 2023-IEEE 49th European Solid State Circuits Conference (ESSCIRC)*. 2023, pp. 489–492.

[3] Manuj Singh et al. "Electronic-Photonic Millimeter-Wave Sensing Element Based on Monolithically Integrated LNA and Triple Cavity Ring Modulator". In: *2023 European Conference on Optical Communication (ECOC)*. 2023.

[4] Amnon Yariv. "Universal relations for coupling of optical power between microresonators and dielectric waveguides". In: *Electronics letters* 36.4 (2000), pp. 321–322.

[5] Nicolas Dupuis et al. "30-Gb/s Optical Link Combining Heterogeneously Integrated III–V/Si Photonics With 32-nm CMOS Circuits". In: *Journal of Lightwave Technology* 33.3 (2015), pp. 657–662.

[6] Jonathan Proesel, Clint Schow, and Alexander Rylyakov. "25Gb/s 3.6pJ/b and 15Gb/s 1.37pJ/b VCSEL-based optical links in 90nm CMOS". In: *2012 IEEE International Solid-State Circuits Conference*. 2012, pp. 418–420.

[7] Mostafa G. Ahmed et al. "A 16-Gb/s -11.6-dBm OMA Sensitivity 0.7-pJ/bit Optical Receiver in 65-nm CMOS Enabled by Duobinary Sampling". In: *IEEE Journal of Solid-State Circuits* 56.9 (2021), pp. 2795–2803.

[8] Nandish Mehta et al. "A 12Gb/s, 8.6μApp input sensitivity, monolithic-integrated fully differential optical receiver in CMOS 45nm SOI process". In: *ESSCIRC Conference 2016: 42nd European Solid-State Circuits Conference*. 2016, pp. 491–494.

[9] Nandish Mehta et al. "A Laser-forwarded Coherent 10Gb/s BPSK Transceiver using Monolithic Microring Resonators in 45nm SOI CMOS". In: *2019 Symposium on VLSI Circuits*. 2019, pp. C192–C193.

[10] Bozhi Yin et al. "Electronic-Photonic Cryogenic Egress Link". In: *ESSCIRC 2021 - IEEE 47th European Solid State Circuits Conference (ESSCIRC)*. 2021, pp. 51–54.

[11] Ghazal Movaghar et al. "First Monolithically-Integrated Silicon CMOS Coherent Optical Receiver". In: *2023 Optical Fiber Communications Conference and Exhibition (OFC)*. 2023, pp. 1–3.

[12] R. L. Nguyen et al. "A Highly Reconfigurable 40-97GS/s DAC and ADC with 40GHz AFE Bandwidth and Sub-35fJ/conv-step for 400Gb/s Coherent Optical Applications in 7nm FinFET". In: *2021 IEEE International Solid- State Circuits Conference (ISSCC)*. Vol. 64. 2021, pp. 136–138.

[13] C. M. Wilkes et al. "60 dB high-extinction auto-configured Mach–Zehnder interferometer". In: *Opt. Lett.* 41.22 (Nov. 2016), pp. 5318–5321.

[14] Ling Liao et al. "High speed silicon Mach-Zehnder modulator". In: *Opt. Express* 13.8 (Apr. 2005), pp. 3129–3135.

[15] Navid Hosseinzadeh et al. "A Distributed Low-Noise Amplifier for Broadband Linearization of a Silicon Photonic Mach–Zehnder Modulator". In: *IEEE Journal of Solid-State Circuits* 56.6 (2021), pp. 1897–1909.

[16] B.E. Little et al. "Microring resonator channel dropping filters". In: *Journal of Lightwave Technology* 15.6 (1997), pp. 998–1005.

[17] Wesley D. Sacher and Joyce K. S. Poon. "Dynamics of microring resonator modulators". In: *Opt. Express* 16.20 (Sept. 2008), pp. 15741–15753.

[18] Hui Yu et al. "Trade-off between optical modulation amplitude and modulation bandwidth of silicon micro-ring modulators". In: *Opt. Express* 22.12 (June 2014), pp. 15178–15189.

[19] Hayk Gevorgyan et al. "Triply resonant coupled-cavity electro-optic modulators for RF to optical signal conversion". In: *Opt. Express* 28.1 (Jan. 2020), pp. 788–815.

[20] Hayk Gevorgyan, Anatol Khilo, and Miloš A. Popović. "Efficient coupled-cavity electro-optic modulator on silicon for high carrier frequency, narrowband RF signals". In: *Frontiers in Optics + Laser Science APS/DLS*. Optica Publishing Group, 2019, FW5C.1.

[21] Yossef Ehrlichman, Nathan Dostart, and Miloš A. Popovic. "Dual-cavity resonant modulators for efficient narrowband RF/microwave photonics". In: *2016 IEEE International Topical Meeting on Microwave Photonics (MWP)*. 2016, pp. 165–168.

[22] Yossef Ehrlichman and Miloš A. Popović. "Dual-cavity optically and electrically resonant modulators for efficient narrowband RF/microwave photonics". In: *2017 Conference on Lasers and Electro-Optics (CLEO)*. 2017, pp. 1–2.

[23] Hayk Gevorgyan and Miloš A. Popović. "Frequency Translating Add/Drop Filters based on Electro-Optically Modulated Photonic Molecules". In: *Frontiers in Optics + Laser Science 2021*. Optica Publishing Group, 2021, FTu6B.4.

[24] Hayk Gevorgyan, Anatol Khilo, and Miloš A. Popović. "Broadband efficient coupled-cavity electro-optic modulators based on Q engineering for RF photonics applications". In: *Conference on Lasers and Electro-Optics*. Optica Publishing Group, 2018, JW2A.59.

[25] Chun-Hsing Li, Chien-Nan Kuo, and Ming-Ching Kuo. "A 1.2-V 5.2-mW 20–30-GHz Wideband Receiver Front-End in 0.18-μm CMOS". In: *IEEE Transactions on Microwave Theory and Techniques* 60.11 (2012), pp. 3502–3512.

[26] Haikun Jia et al. "A Full Ka-Band Power Amplifier With 32.9% PAE and 15.3-dBm Power in 65-nm CMOS". In: *IEEE Transactions on Circuits and Systems I: Regular Papers* 65.9 (2018), pp. 2657–2668.

[27] G. Mangraviti et al. "A 52–66GHz subharmonically injection-locked quadrature oscillator with 10GHz locking range in 40nm LP CMOS". In: *2012 IEEE Radio Frequency Integrated Circuits Symposium*. 2012, pp. 309–312.

[28] Marco Vigilante and Patrick Reynaert. "On the Design of Wideband Transformer-Based Fourth Order Matching Networks for E-Band Receivers in 28-nm CMOS". In: *IEEE Journal of Solid-State Circuits* 52.8 (2017), pp. 2071–2082.

[29] Manuj Singh et al. "Photonic molecule electro-optic modulators for efficient, widely tunable RF sideband generation and wavelength conversion". In: *Frontiers in Optics + Laser Science 2021*. Optica Publishing Group, 2021, FTh6B.2.

[30] Deng Mao et al. "Adiabatic Coupler With Design-Intended Splitting Ratio". In: *Journal of Lightwave Technology* 37.24 (2019), pp. 6147–6155.

[31] Nandish Mehta et al. "A Laser-Forwarded Coherent Transceiver in 45-nm SOI CMOS Using Monolithic Microring Resonators". In: *IEEE Journal of Solid-State Circuits* 55.4 (2020), pp. 1096–1107.

[32] *Developed Simulink toolbox*. URL: `https://github.com/isgcal/SiPh_Simulink`.

[33] S. Buchbinder et al. "Silicon Microring Modulator for High SFDR Analog Links in Monolithic 45nm CMOS". In: *Conference on Lasers and Electro-Optics*. Optica Publishing Group, 2022, SF4L.1.

[34] Sungjae Lee et al. "Record RF performance of 45-nm SOI CMOS Technology". In: *2007 IEEE International Electron Devices Meeting*. 2007, pp. 255–258.

[35] Jason S. Orcutt et al. "Open foundry platform for high-performance electronic-photonic integration". In: *Opt. Express* 20.11 (May 2012), pp. 12222–12232.

[36] Mark T. Wade et al. "75% efficient wide bandwidth grating couplers in a 45 nm microelectronics CMOS process". In: *2015 IEEE Optical Interconnects Conference (OI)*. 2015, pp. 46–47.

[37] Chen Sun et al. "A 45nm SOI monolithic photonics chip-to-chip link with bit-statistics-based resonant microring thermal tuning". In: *2015 Symposium on VLSI Circuits (VLSI Circuits)*. 2015, pp. C122–C123.

[38] Fabio Pavanello et al. “Efficient nanoscale photonic devices and monolithic electronic-photonic subsystems in sub-100 nm SOI CMOS”. In: *2015 IEEE Photonics Conference (IPC)*. 2015, pp. 1–2.

[39] Chen Sun et al. “Single-chip microprocessor that communicates directly using light”. In: *Nature* 528.7583 (Dec. 2015), pp. 534–538.

[40] Amir H. Atabaki et al. “Integrating photonics with silicon nanoelectronics for the next generation of systems on a chip”. In: *Nature* 556.7701 (Apr. 2018), pp. 349–354.

[41] Li Gao, Qian Ma, and Gabriel M. Rebeiz. “A 4.7 mW W-Band LNA with 4.2 dB NF and 12 dB Gain Using Drain to Gate Feedback in 45nm CMOS RFSOI Technology”. In: *2018 IEEE Radio Frequency Integrated Circuits Symposium (RFIC)*. 2018, pp. 280–283.

[42] Mustafa Sayginer and Gabriel M. Rebeiz. “A W-Band LNA/Phase Shifter With 5-dB NF and 24-mW Power Consumption in 32-nm CMOS SOI”. In: *IEEE Transactions on Microwave Theory and Techniques* 66.4 (2018), pp. 1973–1982.

[43] Ozgur Inac, Mehmet Uzunkol, and Gabriel M. Rebeiz. “45-nm CMOS SOI Technology Characterization for Millimeter-Wave Applications”. In: *IEEE Transactions on Microwave Theory and Techniques* 62.6 (2014), pp. 1301–1311.

[44] Li Gao, Eric Wagner, and Gabriel M. Rebeiz. “Design of E- and W-Band Low-Noise Amplifiers in 22-nm CMOS FD-SOI”. In: *IEEE Transactions on Microwave Theory and Techniques* 68.1 (2020), pp. 132–143.

[45] Berke Cetinoneri et al. “*W* -Band Amplifiers With 6-dB Noise Figure and Milliwatt-Level 170–200-GHz Doublers in 45-nm CMOS”. In: *IEEE Transactions on Microwave Theory and Techniques* 60.3 (2012), pp. 692–701.

[46] Di Li, Lei Zhang, and Yan Wang. “Design of 60-GHz amplifiers based on over neutralization and optimized inter-stage matching networks in 65-nm CMOS”. In: *2015 IEEE International Symposium on Radio-Frequency Integration Technology (RFIT)*. 2015, pp. 130–132.

[47] Yaoshun Ding, Soenke Vehring, and Georg Boeck. “Design of 24 GHz High-Linear High-Gain Low-Noise Amplifiers Using Neutralization Techniques”. In: *2019 IEEE MTT-S International Microwave Symposium (IMS)*. 2019, pp. 944–947.

[48] Patrick J. Artz et al. “A Fully-Differential 146.6-157.4 GHz LNA Utilizing Back Gate Control to Adjust Gain in 22 nm FDSOI”. In: *2022 IEEE/MTT-S International Microwave Symposium - IMS 2022*. 2022, pp. 611–614.

[49] Hayk Gevorgyan et al. “High Shift Efficiency O-band Spoked-Ring Modulator Allowing Fully Electro-Optic Channel Tuning in a 45nm CMOS Platform”. In: *Conference on Lasers and Electro-Optics*. Optica Publishing Group, 2021, SW3C.5.

[50] Hayk Gevorgyan et al. "Cryo-Compatible, Silicon Spoked-Ring Modulator in a 45nm CMOS Platform for 4K-to-Room-Temperature Optical Links". In: *2021 Optical Fiber Communications Conference and Exhibition (OFC)*. 2021, pp. 1–3.

[51] Fabio Pavanello et al. "Ring modulators with enhanced efficiency based on standing-wave operation on a field-matched, interdigitated p-n junction". In: *Opt. Express* 24.24 (Nov. 2016), pp. 27433–27443.

[52] Jeffrey M. Shainline et al. "Depletion-mode carrier-plasma optical modulator in zero-change advanced CMOS". In: *Opt. Lett.* 38.15 (Aug. 2013), pp. 2657–2659.

[53] Fabio Pavanello et al. "Ring modulators in standing-wave and partial standing wave operation on a matched interdigitated p-n junction for enhanced efficiency". In: *Frontiers in Optics 2015*. Optica Publishing Group, 2015, FW3E.4.

[54] Kenaish Al Qubaisi et al. "Microring Modulators in a New Silicon Photonics-Optimized 45 nm Monolithic Electronics-Photonics SOI CMOS Platform". In: *2021 Conference on Lasers and Electro-Optics (CLEO)*. 2021, pp. 1–2.

[55] Ramy Rady et al. "A 20–43.5-GHz Wideband Tunable Silicon Photonic Receiver Front-End for mm-wave Channel Selection/Jammer Rejection". In: *J. Lightwave Technol.* 41.5 (Mar. 2023), pp. 1309–1324.

[56] Navid Hosseinzadeh et al. "A 0.5-20 GHz RF Silicon Photonic Receiver with $120dB \cdot Hz^{2/3}$ SFDR using Broadband Distributed IM3 Injection Linearization". In: *2019 IEEE Radio Frequency Integrated Circuits Symposium (RFIC)*. 2019, pp. 99–102.

[57] Michal Rakowski et al. "45nm CMOS - Silicon Photonics Monolithic Technology (45CLO) for next-generation, low power and high speed optical interconnects". In: *Optical Fiber Communication Conference (OFC) 2020*. Optica Publishing Group, 2020, T3H.3.

[58] Abdelaziz Hamani et al. "A 125.5-157 GHz 8 dB NF and 16 dB of Gain D-band Low Noise Amplifier in CMOS SOI 45 nm". In: *2020 IEEE/MTT-S International Microwave Symposium (IMS)*. 2020, pp. 197–200.

[59] Jesse Moody, Stefan Lepkowski, and Travis M Forbes. "A Low Power V-Band LNA with Wide Supply Voltage Range Exploiting Complementary Current Reuse and Power Efficient Bias Point". In: *2023 IEEE/MTT-S International Microwave Symposium - IMS 2023*. 2023, pp. 135–138.

[60] Emanuel Cohen et al. "Robust 60 GHz 90nm and 40nm CMOS wideband neutralized amplifiers with 23dB gain 4.6dB NF and 24% PAE". In: *2012 IEEE 12th Topical Meeting on Silicon Monolithic Integrated Circuits in RF Systems*. 2012, pp. 207–210.

[61] Chia-Jen Liang et al. "A 0.6-V VDD W-Band Neutralized Differential Low Noise Amplifier in 28-nm Bulk CMOS". In: *IEEE Microwave and Wireless Components Letters* 31.5 (2021), pp. 481–484.

[62] Donggu Im, Ilku Nam, and Kwyro Lee. "A CMOS Active Feedback Balun-LNA With High IIP2 for Wideband Digital TV Receivers". In: *IEEE Transactions on Microwave Theory and Techniques* 58.12 (2010), pp. 3566–3579.

[63] Sinyoung Kim and Kuduck Kwon. "Broadband Balun-LNA Employing Local Feedback gm-Boosting Technique and Balanced Loads for Low-Power Low-Voltage Applications". In: *IEEE Transactions on Circuits and Systems I: Regular Papers* 67.12 (2020), pp. 4631–4640.

[64] Jingzhi Zhang et al. "Analysis and Design of Ultra-Wideband mm-Wave Injection-Locked Frequency Dividers Using Transformer-Based High-Order Resonators". In: *IEEE Journal of Solid-State Circuits* 53.8 (2018), pp. 2177–2189.

[65] Federico Vecchi et al. "A wideband mm-Wave CMOS receiver for Gb/s communications employing interstage coupled resonators". In: *2010 IEEE International Solid-State Circuits Conference - (ISSCC)*. 2010, pp. 220–221.

[66] Woorim Shin et al. "A Compact 75 GHz LNA with 20 dB Gain and 4 dB Noise Figure in 22nm FinFET CMOS Technology". In: *2018 IEEE Radio Frequency Integrated Circuits Symposium (RFIC)*. 2018, pp. 284–287.

[67] Asif Mirza et al. "Silicon Photonic Microring Resonators: A Comprehensive Design-Space Exploration and Optimization Under Fabrication-Process Variations". In: *IEEE Transactions on Computer-Aided Design of Integrated Circuits and Systems* 41.10 (2022), pp. 3359–3372.

[68] Danielius Kramnik et al. "Fast-Tuning Adiabatic Microrings for CROW Filters and Athermal WDM Receivers in a 45 nm SOI CMOS Process". In: *Conference on Lasers and Electro-Optics*. Optica Publishing Group, 2022, SF4M.2.

[69] Jiawei Xu et al. "A 160 μW 8-Channel Active Electrode System for EEG Monitoring". In: *IEEE Transactions on Biomedical Circuits and Systems* 5.6 (2011), pp. 555–567.

[70] Honglei Wu and Yong Ping Xu. "A 1V 2.3/spl mu/W Biomedical Signal Acquisition IC". In: *2006 IEEE International Solid State Circuits Conference - Digest of Technical Papers*. 2006, pp. 119–128.

[71] Fan Zhang et al. "A Low-Power ECoG/EEG Processing IC With Integrated Multiband Energy Extractor". In: *IEEE Transactions on Circuits and Systems I: Regular Papers* 58.9 (2011), pp. 2069–2082.